Study of the pore systems of metal-organic frameworks, mesoporous silica, and low-k dielectric layers by means of positron annihilation spectroscopy

Dissertation

zur Erlangung des Doktorgrades der Naturwissenschaften
(Dr. rer. nat.)

der

Naturwissenschaftlichen Fakultät II
Chemie, Physik und Mathematik

der Martin-Luther-Universität
Halle-Wittenberg

vorgelegt von
Herrn
AHMED GAMAL ATTALLAH ABDELMAKSOUD ELSHERIF
geb. am 20.08.1986 in Kalyobiya, Ägypten

Gutachter:

1- Prof. Dr. Reinhard Krause-Rehberg

2- Prof. Dr. Dirk Enke

3- Prof. Dr. Klaus Rätzke

Halle (Saale), 16.02.2018

Verteidigt am 15.05.2018

Acknowledgements

First, my outmost thanks go to **Allah** for giving me the strength, patience and great support for conducting this work.

I would like to express my sincere gratitude to my advisor **Prof. Dr. Reinhard Krause-Rehberg** for his continuous support of my Ph.D study and related research, for his patience, motivation, and immense knowledge. His guidance helped me in all the time of research and writing of this thesis.

Besides my advisor, I would like to thank **Prof. Dr. Dirk Enke**, Leipzig University for his participating in suggestion the research program of this thesis, the preparation of the samples of my research by his group, his helpful discussions, and his wonderful cooperation.

Also, I wish to express my sincere gratitude to **Prof. Holdt** and **Dr. Suvendu Mondal**, Potsdam University for supplying MOF samples. Such a collaboration yielded three publications with very interesting results.

Additionally, I express my gratitude to **M. Sc. Denise Schneider**, **Dr. Hans. Uhlig**, and **Dr. Gregor Dornberg** (the group of Prof. Enke) for preparing CPG and pseudomorphic transformed samples. **Dipl.-Ing. Nicole Köhler**, Chemnitz University is thanked for preparing the ULK films.

A special thank goes to **Assoc. Prof. Radek Zaleski**, Maria Curie-Skłodowska University, Poland for his fruitful discussions and suggestions and for providing some MATLAB codes and revising my MATLAB codes. He was incredibly patient during our discussions and communication.

My sincere thanks also go to **Dr. Andreas Wagner**, **Dr. Maik Butterling**, and **Dr. Maciej Oskar liedke**, HZDR who gave access to the MePS laboratory at ELBE facility. Without they precious support it would not be possible to conduct the slow positron measurements.

To all my colleagues in the work group of positron annihilation at the Martin Luther University Halle-Wittenberg, **Dr. Mohamed Elsayed**, **Dr. Marco John**, **M.Sc. Alaa Ibrahim**, **M.Sc. Chris Bluhm**, cordial thanks for all the intellectual discussions we had. **M.Sc. Eric Hirschmann** is highly acknowledged for his software of DPALS. The team of the mechanical and electronic workshops are deeply appreciated.

I would like to take this opportunity to thank my master thesis supervisors **Prof. Dr. Mamdouh Abdel Rahman** and **Prof. Dr. Emad Badawi** (Minia University, Egypt), with the help of whom I managed to take my first step in research. I am indebted for the continuous support from my passed father and without whom I could not have accomplished this degree. Special thank goes to my

siblings for all their help and motivation. I am grateful to my wife Noha and my boys Hossam and Mohamed for their patience and great support in many ways during my Ph.D. study.

Contents

List of Figures

List of Tables

Symbols and abbreviations

Chapter 1

AC	Activated Carbon
CNT	Carbon Nanotube
MOF	Metal-Organic-Framework
IC	Integrated Circuit
ULK	Ultra-Low-K
IUPAC	International Union of Pure and Applied Chemistry
MW	Microwave-assisted
MCM-41	Mobile Composition of Matter -41
SBA-15	Santa Barbara Amorphous-15
k	dielectric constant
CVD	Chemical Vapor Deposition
SAXS	Small Angle X-ray Scattering
SANS	Small Angle Neutron Scattering
PAS	Positron Annihilation Spectroscopy
H-K	Harvath-Kawazoe
BJH	Barrett, Joyner, and Halenda
BET	Brunauer, Emmett, and Teller
DFT	Density Functional Theory
PSD	Pore Size Distribution
CLD	Chord-Length-Distribution
PALS	Positron Annihilation Lifetime Spectroscopy
p-Ps	para-Positronium
o-Ps	ortho-Positronium

Chapter 2

DBS	Doppler Broadening Spectroscopy
ACAR	Angular correlation of annihilation radiation
SLOPOS	Slow Positron
LINAC	LINear ACcelerator
GiPS	Gamma-induced Positron Annihilation Spectroscopy
ELBE	Electron LINAC with high Brilliance and low Emittance
HZDR	Helmholtz-Zentrum Dresden - Rossendorf
MePS	Monoenergetic Positron Source
λ_b	defect free bulk-annihilation rate
κ_d	defect-trapping rate
λ_d	defect related-annihilation rate
τ	positron-annihilation lifetime
I	positron intensity

λ_p	pick-off annihilation rate
FWHM	Full-Width at Half-Maximum
DPALS	Digital Positron Annihilation Lifetime Spectroscopy
τ_{avg}	average positron lifetime
PMT	Photo-Multiplier Tube
ADC	Analog-to-digital-converter
MELT	Maximum Entropy of LifeTime
HPG	High Purity Germanium
MCA	MultiChannel Analyzer
TE	Tao-Eldrup
RTE	Rectangular Tao-Eldrup
ε	moderation efficiency
EPOS	ELBE Positron Source
RF	Radio Frequency

Chapter 3

IFP	Imidazolate Framework Potsdam
PXRD	Powder X-ray Diffraction
CE	Conventional Electrical heating
HKUST	Hong Kong University of Technology
DMF	dimethylformamide
EELViS	Excited Energy Levels and Various Shapes
COF	Covalent-Organic Framework
HOF	Hydrogen bonded Organic Framework
MBB	molecular building block

Chapter 4

MTS	Micelle-Templated Silica
CPG	Controlled Porous Glass
SHA	Spelt Husk Ash
RHA	Rice Husk Ash
CTAB	cetyltrimethylammonium bromide
CTAOH	cetyltrimethylammoniumhydroxide
PFG-NMR	Pulsed-field gradient nuclear magnetic resonance
ETE	Extended Tao-Eldrup

Chapter 5

PECVD	Plasma Enhanced Chemical Vapor Deposition
EP	Ellipsometric Porosimetry
XRP	X-Ray Porosimetry

Chapter 1

Porous materials and their characterization methods

1.1 Introduction

Porous materials are those materials which contain channels, cavities, or interstices. Many applications and developments have been performed due to the use of porous materials because of their tunable pore size, high specific surface area, and surface and framework functionalization. To reach this massive number of applications, immense studies and research have been reported. Our air has a huge amount of CO_2 (407.18 ppm, according to the National Oceanic and Atmospheric Administration Earth System Research Laboratory website [1]) and other pollutions which affect our overall health and can result in hazardous climate changes. Porous materials with controlled pore sizes and functionalized internal surfaces can be used to adsorb undesirable particles from the air. Also, they can be used to purify water and petroleum with the same procedure by adsorbing specific molecules.

As a little survey of these materials, Activated carbon (AC) and carbon nanotube (CNT) could be used to remove heavy metal ions like lead, cadmium, chromium, copper, and nickel from wastewater [2]. AC and CNT can do this because of their large micropore, mesopore volumes, and their high surface area. Researchers in [3] synthesized Metal-Organic Framework (MOF) porous materials to purify the air from ammonia. This is because ammonia has a high vapor pressure of 7600 mmHg at 298 K [3] and it produces inorganic chemicals highly due to its broad uses. In addition to MOF, zeolites can be used in gas separation process of CO_2 and CH_4 [4]. Additionally, zeolites are used for supporting materials, shape selectivity (by carrying a metal which in turn directs the shape during the reaction), and solid acid catalysis [5] due to their large surface area and cage-like pore system. The problem with zeolites as catalysts is the pore constraint because they cannot be used to perform the cat-

alyst process with larger molecules. Ordered mesoporous materials (like Mobile Composition of Matter-41 (MCM-41) and Santa Barbara Amorphous-15 (SBA-15)) overcome this problem. In addition to the overcoming of the pore constraint, ordered mesoporous materials have a high surface area with very narrow pore size distribution (PSD). Despite these advantages of ordered mesoporous material, they have low acidity and low stability, and efforts to solve these limitations are attempting. The burning of gasoline by the combustion engines of cars and trucks release a high amount of CO_2 and other exhausts to the air hence, looking for other alternative engines is an urgent issue. Clean energy offers the opportunity to get rid of these undesirable exhaust. Fuel cells are strong competitors for the combustion engines but fuel cell is limited in use. Besides the other problems of making the fuel cell commercially available (cost and technology), the storing of hydrogen as a fuel is still also a problem. This is because the current storage technologies like high-pressure compression or liquefaction of hydrogen are difficult and expensive to be used in a small vehicle. The use of AC, CNT, and MOFs and tuning their templates and modifying their structure enables storing of high amounts of hydrogen in their pores at room temperature [6]). The integration of very fast transistors with a growing in their numbers and a shrinking in their sizes onto a single chip is a crucial issue in the microelectronic industry. The reduction of the transistor's size reached a point where any further size reduction yields a signal delay due to the interconnection between wires [7]. The signal delay is expressed as RC where R represents the wire resistance and C is the interlayer dielectric capacitance. To reduce such a signal delay as possible, the conventional composition of the integrated circuits (ICs) should be replaced. For doing so, aluminum wiring is replaced by copper which has a smaller resistance and dielectric substances with k value less than that of the traditional SiO_2 ($k = 4$) have to be integrated. Since air has $k = 1$, production of pores in dielectric materials would reduce the k value to get ultra-low-k(ULK) materials with a $k < 2$. So, porous dielectric materials can enhance the overall performance of microprocessors in microelectronics industry significantly.

Aside from the aforementioned applications of porous materials, they can be used also for vapor separation, drug delivery and storage, templates in low-dimensional materials' preparation [8], light-weight cores, packaging, filters, and thermal and electrical insulators [9].

1.2 Scope of the thesis

The main theme of this thesis is to use the positron annihilation lifetime spectroscopy (PALS) as a porosimetry tool for some porous materials which exhibited very interesting properties. Some of these materials are studied by PALS for the first time (biomasses). Some MOFs showed conflicts between crystallographic and gas sorption porosities, induced defects due to the activation, and very high gas uptakes, therefore, the first aim of this thesis is to apply the PALS method to interpret these conflicts and properties. The second aim is to use PALS for investigating the transformation of highly disordered porous silica from different sources (German-Spelt Husk Ash (G-SHA) and silica gel) as well as the transformation of a controlled porous glass (CPG) sample. This second aim is very interesting from two aspects; firstly from adding economic and environmental values to biomasses (G-SHA) and secondly; from using the PALS method which would help for understanding the transformation process deeply. Understanding and depth profiling of the porous system in some ULK thin films synthesized via a novel method by employing the mono-energetic positron source (MePS) is the final aim of this thesis.

1.3 Classification of porous materials

Nanoporous materials can be classified according to their dimensions (diameter) and the building blocks. According to the International Union of Pure and Applied Chemistry (IUPAC) classification [10], porous materials can be divided into three different categories:

Micropores→ materials with pore size less than 2 nm (typically from 0.2 to 2 nm). They can be used for gas purification, storage, and filtering because of their small pores which in turn will host small molecules only.

Mesopores→ materials with pore size between 2 nm and 50 nm. This kind of porous materials of a fairly large pore diameter can be used in adsorbing systems like liquids and vapors.

Macropores→ materials with pore size larger than 50 nm. They can host large molecules like small biological molecules.

Whatever the kind of the pores, these pores could be closed or open pores. Closed pores are empty spaces buried inside the material and cannot be accessible by the adsorbate. This sort is useful in thermal insulation and light-weight materials. The status of the pore will control and limit the usage of this porous material [11].

The chemical nature of the pore walls or the building materials in porous ma-

terials can be divided into three different types: Organic, inorganic, and hybrid materials. Organic materials like AC and CNT are bonded by the hydrogen bonds forming a regular structure. They can interact with organic molecules and have a small mechanical and thermal stability. Inorganic structures like zeolites, aluminates, and silicates [6] have strong covalent bonds and they are mechanically and thermally stable which enable these materials to be used as support materials. Hybrid porous structures like MOF have two advantages over organic and inorganic as they have high mechanical and thermal stability besides that, a variety of functional groups can be used in the structure of MOFs which means a diversity in their applications.

1.4   Preparation of porous materials

1.4.1   Synthesis of microporous materials - Zeolites and MOFs

Zeolites
Zeolites contain principally in their framework aluminum, silicon, and oxygen. Both silicon and aluminum are tetrahedrally attached together via a common oxygen atom. In zeolites, some of the quadri-charged silicon cations are replaced by triply-charged aluminum producing a positive charge defecinity. This developed charge is compensated by the presence of singly and/or doubly-charged cations (e.g. Na^+, K^+, Ca^{2+}, and Mg^{2+}) [12] in the structure forming pores or spacious rings. This way, zeolites framework contains channel, channel intersections, and/or cages of ~ 0.3 to 1.5 nm. To mention some examples, zeolites can form small pore with eight member-ring apertures with diameters of 3-4.5 Å(zeolite A), medium pore with ten membered-ring apertures of 4.5-6.0 Å(zeolite ZSM-5), and large pore with twelve membered-ring apertures of 6.0-8.0 Å(Beta and Y zeolites). These different representative types are shown in figure 1.1.

Zeolites are typically synthesized under hydrothermal conditions in an autoclave using a cationic organic template or structure directing agent (commonly tetrapropylammonium (TPA^+) cations). This template is added to an alkali solution of sodium silicate with sodium aluminate, then the suspension is heated [14]. Tetrahedral clusters, which are considered to be the primary building blocks of zeolites, are formed by the heating and these primary building units will be assembled around the organic templates or into secondary building units by varying temperature, heating time, and the pH. Calcination is the final step of zeolite's synthesis and calcination means burning the organic template by heating to a high temperature of 823 K under oxygen. Figure 1.2 shows the
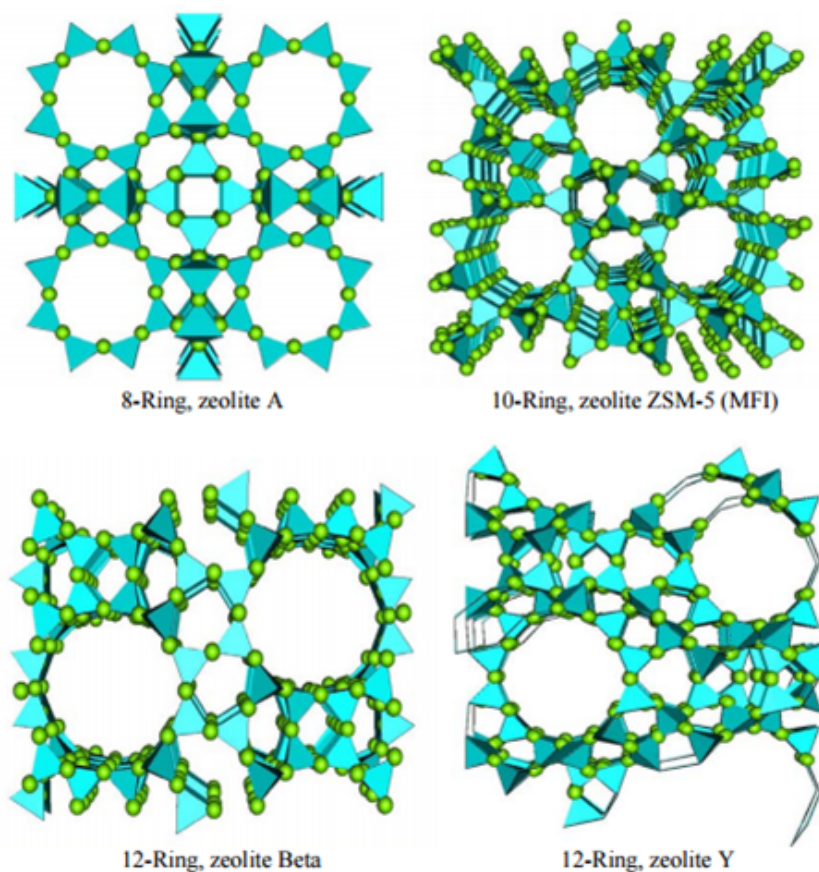
Figure 1.1: Different types of Zeolites [13].

synthesis procedure of ZSM-5 where tetraethylorthosilicate (TEOS) is used as a silica source [15]. The remaining framework is a negative porous framework
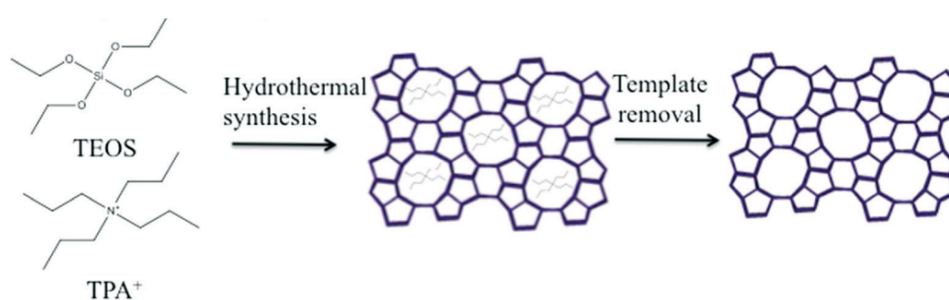
Figure 1.2: Synthesis of a zeolite around an organic template [15].

and it is charged balanced with a metal cation, or can form an acidic-catalyst by accepting an H^+ atom. Due to their porous nature and charged surfaces, zeolites found their way in many applications like ion-exchange beds, water purification, and adsorption and their acidic surface allowed them to be used in heterogeneous chemical catalysts.

Metal Organic Frameworks (MOFs)

MOFs are crystalline porous materials formed by connecting a metal node (one atom or cluster) to an organic linker. Due to their large surface area, tunable pore size, and functionality, MOFs can be used effectively in gas storage and separation applications. One of the most interesting facts about MOFs is the ability to manipulate either the metallic nodes or the organic spacers to yield a variety of porous structures and orientations [16]. Preparation of MOFs can be divided into two types; solution phase synthesis and solid state synthesis while the latter produces some difficulties to create single crystal because it involves grinding process which means a collapse of the formed crystals [17]. There are different approaches for MOFs synthesis such as solvothermal, microwave-assisted, electrochemical, mechanochemical, and sonochemical methods [16]. In the solvothermal method, conventional electrical heating is used to initiate the reaction between the isolated metal ions and organic ligands to facilitate the self-assembling of MOFs [18] where metal centers act as acid while the basic solvent deprotonates the organic linker's acid precursor so that the resulting linker acts as a base. An activation procedure should be performed to remove any residual solvent in the pores. Despite the higher internal surface area, higher yield, and better crystallinity of solvothermal- MOFs, this activation requires a long duration which can reach several weeks [19]. During MOFs synthesis via microwave (MW)- assisted conditions, microwave radiations are used to supply the energy for the reactions which occur due to the interaction between the electromagnetic waves and the mobile electric charges like polar solvent molecules. In the presence of MW, polar molecules or free ions try to align with the alternating 300-300 000 MHZ [19] field producing an electric field. Solvents absorb MW radiations and convert electromagnetic waves into heat. The MW-assisted method is preferred due to its rapidity, high efficiency, and particle size reduction. The two schemes of the conventional heating and MW-assisted conditions of preparing MOFs are presented in figure 1.3. More details about electrochemical, mechanochemical, and sonochemical methods are given in [20].

1.4.2   Synthesis of mesoporous materials-MCM-41, SBA-15, and low-*k* materials

Mobile Composition of Matter-41 (MCM-41)

Removable templates like organic molecules, ions, surfactants, or colloidal particles can be used to synthesize mesoporous materials. Ordered mesoporous materials, like MCM-41, which contain silicate walls between the ordered pores,
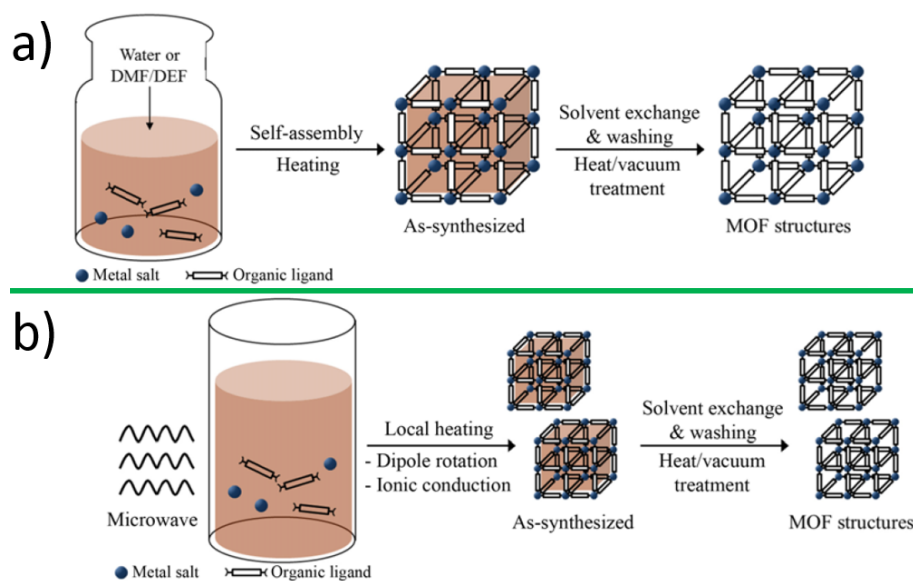
Figure 1.3: Schemes of preparing MOFs by a) the conventional heating and b) MW-assisted conditions [20].

can be synthesized by liquid crystalline template [21]. In this liquid crystal templating mechanism, assemblies of surfactant micelles (e.g., alkyltrimethy-lammonium surfactants) template the porous structure of the mesophase [22]. This mechanism is illustrated in figure 1.4 which shows two possible pathways for preparing MCM-41. In the first pathway, the liquid crystal phase is intact before the silicate species are added while in the second one the addition of the silicate results in the ordering of the subsequent silicate encased surfactant micelles [23]. The procedure of this synthesis process starts with a dilute so-
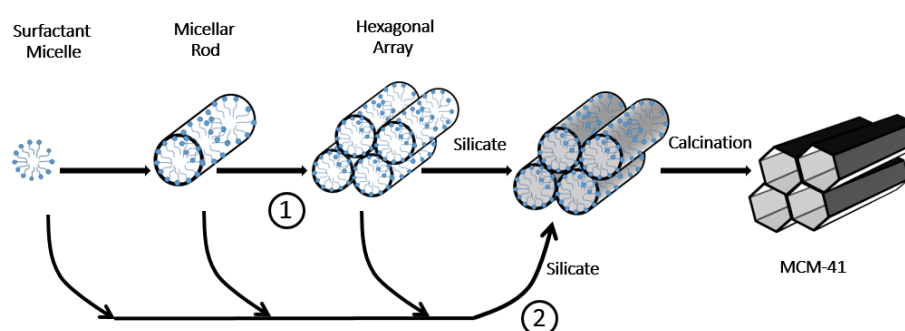
Figure 1.4: Possible ways of MCM-41 Synthesis by 1) liquid crystal and 2) silicate anion initiated (redrawn from [23]).

lution of a surfactant, having spherical micelles, and a silica source addition under high pH [23]. The surfactant may be directed to pathway 1 (figure 1.4) in which the surfactant micelles aggregates into rods. These structures have a hexagonal arrangement in solution [24]. After that, inorganic silicate present in the reaction mixture could then arrange around these formed arrays to produce

an inorganic structure reflecting the hexagonal micellar array. In the second possible path of interaction (pathway 2 in figure 1.4), the silicate influences the formation of this liquid crystal phase. In both paths, the silica is condensed within the mesostructure with time and/or heating. Afterwards, the surfactants are removed by calcination at high temperatures ($\sim$ 870 K) leaving behind the hexagonal porous structure of MCM-41. With this process, the pore size of MCM-41 can be varied according to the carbon chain lengths of the surfactant.

Santa Barbara Amorphous-15 (SBA-15)

SBA-15 mesoporous materials have uniform hexagonal pores with narrow PSD, tunable diameter, and high specific surface area [25, 26]. The thick walls of the SBA-15 allowed it to have higher thermal and mechanical stability than the thinner-walls MCM-41 [27]. SBA-15 was obtained by using amphiphilic block copolymers Pluronic P123 as organic structure-directing agents and TEOS as a silica source [28] under acidic conditions (pH $\approx$1) [25, 26]. After the synthesis, the templates are removed from the structure by calcination (usually at 773 K in air for 6 h [25]) and washing [29]. With this procedure, and according to [30], the obtained structure of SBA-15 has parallel pores with a highly ordered structure (figure 1.5). The pore size and the silica walls can be varied by changing the heating temperature (308-413 K) [25]. In addition to the mesopores exist in
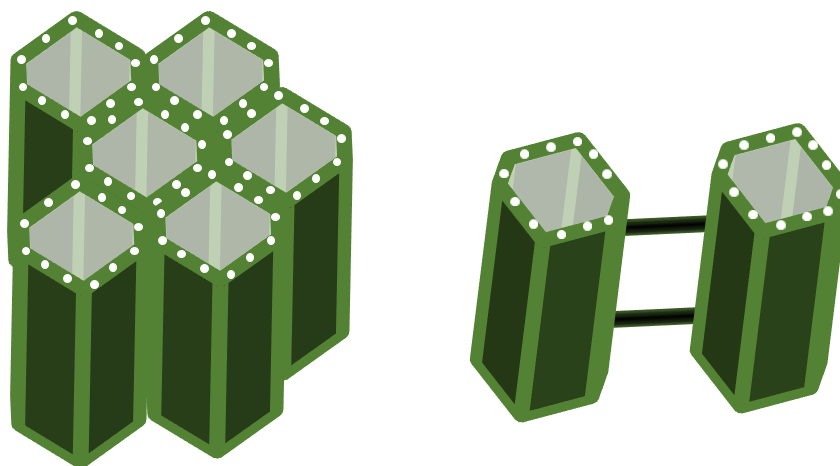
Figure 1.5: Illustration of the porous structure of SBA-15

SBA-15, micropores are created in its thick walls due to the penetration of the hydrophobic ethylene oxide chain in the silica walls [31].

Low-k

Chemical vapor deposition (CVD) and spin coating are used to synthesize low-k materials. On the spin coating method, the first step is to create a stable liquid

solution consisting of molecular units (which will form the material's backbone (yellow balls in figure 1.6)), molecular units which is called "porogen" (green drops in figure 1.6), and solvent. Such a solution is then deposited on a substrate's surface (grey disk in figure 1.6) via spin coating [32]. During the spinning, both the matrix and porogen are miscible and interact together and the centrifugal force spreads the solution drops into a thin layer. The cross-linking of the framework (and possibly the porogen) occurs after performing initial curing in the 373-573 K range for few minutes [32]. Regarding the CVD method, the deposited film is formed from free radicals, with high reactivity, in their gaseous phase. These free radicals are cross-linked by a covalent bond network. Finally, the spin-coated films or CVD ones are baked at a relatively
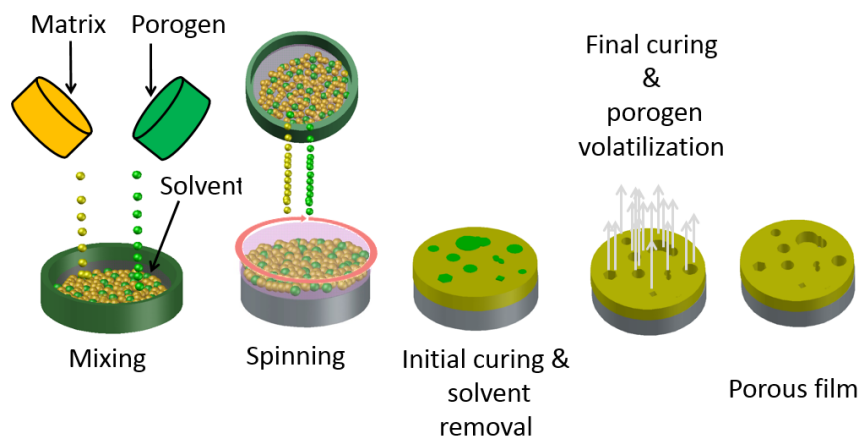
Figure 1.6: Description of spin coating of low-*k* materials

high temperature, 723 K, to remove porogen from the film's framework leaving behind a "porous" film.

1.4.3 Synthesis of macroporous materials

Macroporous materials are synthesized by different ways including templating such as emulsion [33] and spherical array templating [34]. In the emulsion templating method, an emulsion of uniform oil spheres is prepared to get the desired droplet sizes. The next step is to prepare a metal oxide sol by mixing a chemically modified metal alkoxide with formamide which has a little water. Afterwards, the emulsion is dispersed in the sol. The droplet volume fraction is adjusted to the desired porosity [33]. Finally, the material is dried and a heat treatment is performed in ordered to get the porous network. While in the spherical array method, a non-porous spherical template like polystyrene spheres are packed into an ordered array and silicon alkoxide solution is added to allow hydrolysis and condensation around the spheres. Finally, the template

can be removed by thermal degradation of the composite leaving a macroporous solid behind. Figure 1.7 shows the formation of macroporous material by means of spherical array templating method.
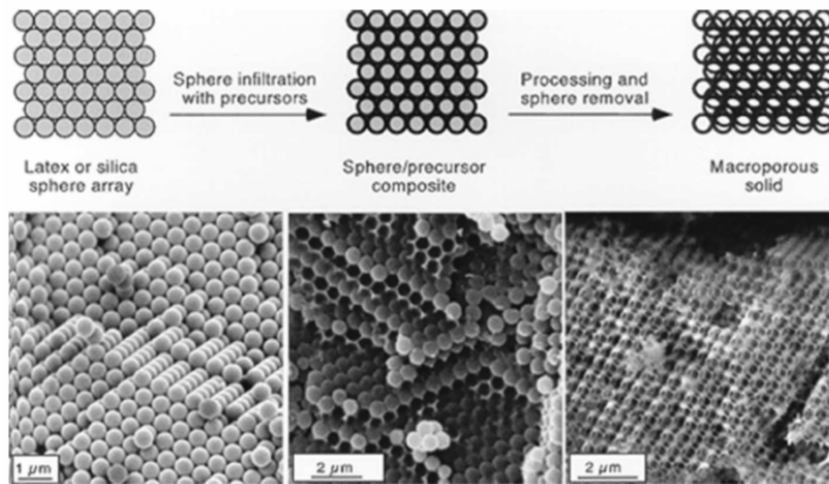
Figure 1.7: Spherical templating method for creation of macroporous solid [35].

1.5   Characterization of porous materials

After the synthesis of a porous material, it is intuitive to do the pore characterization in order to know whether they met the expected features or not. Pore characterization is to know the pore size, distribution, volume, surface area, and the chemical nature of the pore's surfaces and walls. There are several methods to characterize porous materials like gas adsorption, mercury intrusion, Small Angle X-ray and Neutron Scattering (SAXS and SANS), Electron microscopy, Positron Annihilation Spectroscopy (PAS), and others. In the following section, the principles, advantages, limitations of some of these characterization methods will be discussed with a focus on the PAS method.

1.5.1   Gas adsorption

Adsorption means an attachment of a molecule of liquid or vapor to a surface atom of solid under specific conditions (pressure and temperature) by means of surface's forces. It differs from absorption which means a penetration of mass into a solid or a liquid. The term "sorption" refers to the process when the adsorption and absorption occur together while when the process is to extract the attached or adsorbed molecules from a material surface by reducing the pressure, this process is called "desorption". The adsorption method needs an

adsorbate, which is the (guest) gas or vapor, and adsorbent, which is the (host) material of interest. Adsorption is an exothermic process due to the entropy reduction of the surface gas molecules relative to the bulk ones. Depending on the type of the force acts on the material's surface, adsorption can be classified into two types, physisorption and chemisorption [36]. The physisorption process is characterized by weak interactions between the adsorbate and the adsorbent (Van der Waal's forces) [37], multilayer formation, and the small heat of adsorption. It also can occur on any surface (surfaces universality) and it needs no activation energy to be performed [37]. On the other hand, chemisorption, consisting of a chemical reaction confined to the solid surface, needs a high heat of adsorption to be performed, it is highly specific, it requires activation energy, and it forms monolayers. In order to use gas adsorption to characterize porous materials, this gas must be enforced to enter the whole pores in the porous materials. This can be done by changing the applied pressure of the adsorbate. With changing the applied pressure of the gas, the amount of the adsorbate changes as well. Since the changing of the applied pressure and the adsorbed volume is performed at a constant temperature, the resulting relation is called sorption (due to the adsorption and desorption) isotherm.

By performing the adsorption isotherm accurately, a number of different theories or models can be applied to extract information about the porous system within the samples. For analyzing micropore data, MP-method [38], Dubinin plots [39], t-Plot [40, 41], and Harvath-Kawazoe (H-K) [42] calculations have to be used. On the other hand, one can use Barrett, Joyner and Halenda method (BJH) [43], Brunauer, Emmett, and Teller (BET) [44] for mesopore analysis. Density Functional Theory (DFT) [45–47] can be used for micropores and mesopores [48].

1.5.1.1 Adsorption isotherms

According to the IUPAC [10], adsorption isotherms may be classified into six types (with two subgroups) as shown in figure 1.8:

Type I: It represents the adsorption of micropores having relatively small external surfaces (e.g. AC, Zeolites, and certain porous oxides). Type I(a) reflects isotherms in narrow micropores while type I(b) represents the isotherms exist in materials with broad pore size distribution from micropores till mesopores

Type II: It is given by the physisorption of most gases on non-porous or macroporous adsorbents and it is a result of unrestricted monolayer-multilayer adsorption. At point B, the filling of the monolayers ends and the filling of the multilayers starts.

Type III: This isotherm is not common because it has no indication about
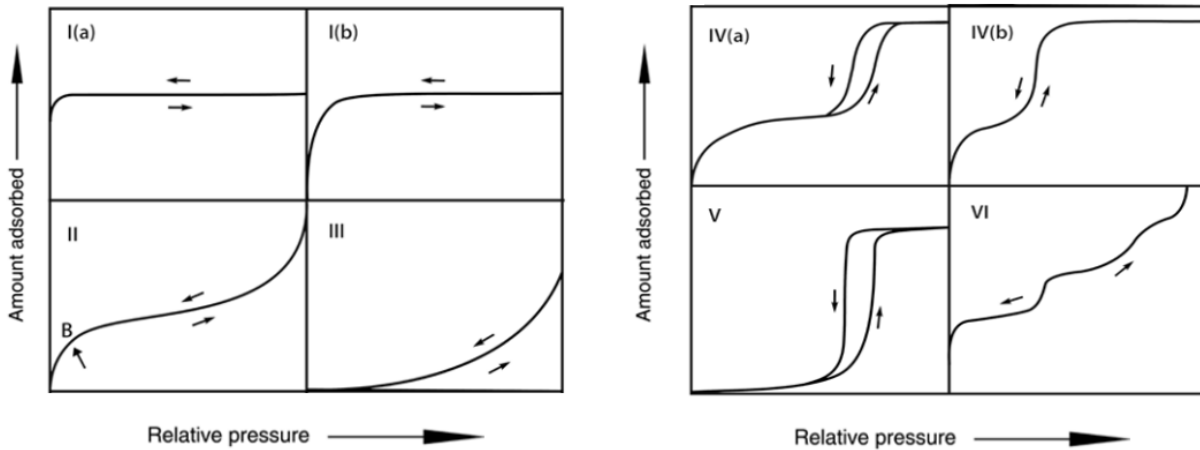
Figure 1.8: Types of adsorption isotherms(taken from [10]).

monolayer-multilayer filling (no point B) and it is characterized by weak interaction between adsorbent and adsorbate.

Type IV: It has hysteresis associated with capillary condensation taking place: (**a**) in mesopores having pore width exceed a certain width, depending on the adsorbent and temperature, and (**b**) in very narrow mesopores. This type is characterized also by a limiting uptake at high p/p_0.

Type V: This isotherm is not common as type III but it is obtained with certain porous materials.

Type VI: It is a representation of layer-by-layer adsorption on a highly uniform nonporous surface and the height of step-like isotherm gives the capacity of each adsorbed layer.

1.5.1.2   Specific surface area

The determination of the surface area is one of the main goals of characterization of porous materials because surface area plays an important role in the performance of porous materials, e.g. affects adsorption capacity, electron/ion current density, and dissolution rates. If the adsorbed gas molecules represented a close-packed monolayer and each molecule accommodated at a definite site from the entire pore surface, and these molecules of the monolayer filled all the space in the entire pore surface, the determination would be direct. But this is not the case in the chemisorption because the molecules in the chemisorption are widely spaced and the saturation limit does not reveal a clear relationship to the specific surface area. On the other hand, physisorption involves multilayer adsorption. This problem is solved by using the simple model isotherm of Brunauer, Emmett, and Teller (BET) [44] based on Langmuir model [49]. BET model considered multilayer adsorption and it was used to extract the mono-

layer capacity to determine the specific surface area ($S_{sp.}$). This model based on the following assumptions [50]: each molecule in any layer provides only one site for another molecule in the subsequent layer. The molecules in the first layer are in contact with the surface of the adsorbent while the molecules in the second and subsequent layers are in contact with other adsorbate molecules which means that all the molecules which are not in the first layer have the same liquefaction energy of the adsorptive. There is no lateral interaction between the adsorbed molecules and there is a uniform array of surface sites. The multilayer has an infinite thickness when the ratio between the equilibrium, P, and the saturation pressure P_0 equals unity. At the equilibrium pressure P, the covered surface remains constant and both rates of condensation on the uncovered surface and evaporation from the first layer are equal so one can write the following equation:

$$a_i P \Theta_{i-1} = b_i \theta_i exp \left(\frac{-E_i}{RT} \right) \tag{1.1}$$

where a_i and b_i are adsorption and desorption constants, θ_{i-1} and θ_i are the surface areas covered by $i-1$ and i layer, E_i is the adsorption energy (positive) of layer i, R is the gas constant, and T is temperature. Since the infinite multilayer thickness occurs at relative pressure $\frac{P}{P_0}$ =1 so, the amount of the adsorbed gas in all layers can be summed and simplified to get the following BET equation

$$\frac{\dfrac{P}{P_0}}{n \left(1 - \dfrac{P}{P_0} \right)} = \frac{1}{n_m C} + \frac{C-1}{n_m C} \left(\frac{P}{P_0} \right) \tag{1.2}$$

where n is the adsorbed gas quantity (for example, in volume units), n_m is monolayer adsorbed gas quantity, and C is the BET constant which relates the adsorption energy of the first monolayer via:

$$C = exp \left(\frac{E_1 - E_L}{RT} \right) \tag{1.3}$$

where E_1 is the heat of adsorption for the first layer, and E_L is that for the second and higher layers and is equal to the heat of liquefaction. In equation 1.2, a plot between $\dfrac{1}{n \left(\dfrac{P}{P_0} - 1 \right)}$ versus $\left(\dfrac{P}{P_0} \right)$ in the range of $0.05 < \dfrac{P}{P_0} < 0.35$ yields a straight line with the slope, $s, = \left(\dfrac{C-1}{n_m C} \right)$ and intercept, $i, = \left(\dfrac{1}{n_m C} \right)$, which means that both C and n_m can be determined from the plot where $C = \left(1 + \dfrac{s}{i} \right)$

and $n_m = \left(\dfrac{1}{s+i} \right)$.

The BET specific surface area, $S_{sp.}$, of the adsorbent has the following form:

$$S_{sp.} = \frac{n_m \sigma_n N_A}{n M_s} \tag{1.4}$$

where M_s, σ_n, N_A, n are the mass of the sample, the cross-section area of a single nitrogen molecule (16.2 Å^2), the Avogadro's number, and, again, the adsorbed gas quantity, respectively. The surface area of a single molecule, σ, is calculated by using the occupied area by one molecule and with the assumption of forming a close pack of spherical molecules at the surface; the following expression can do this:

$$\sigma_n = 1.09 \left(\frac{M}{N_A d_L} \right)^{\frac{2}{3}} \tag{1.5}$$

where 1.091 is the coefficient related to the spherical shape and hexagonal close packing of molecules, M is the molecular weight, and d_L is the density of the adsorbed liquid (which is obtained experimentally using a reference system of a known surface area).

1.5.1.3   Pore Size Distribution (PSD)

Capillary condensation (pore filling) is used to calculate the PSD. During gas sorption (for example, N$_2$) experiments, an adsorbed film is formed in the pore wall and the thickness of this film increases with increasing the pressure. The process continues until the condensation pressure is reached where the adsorbed vapor is condensed and the pore filing begins. This condensation process occurs only in pores having pore sizes larger than a critical value [51]. Most methods of pore size distribution (PSD) determination are based on the application of Kelvin equation [53]. Kelvin equation, equation 1.6, is a relation between the pore size and relative pressure of a condensed liquid in pores and it provides a suitable method to determine PSD for mesopores.

$$ln\frac{P}{P_0} = \frac{-2\gamma\nu_l}{RT r_c} \tag{1.6}$$

where γ is the liquid-vapor surface tension, ν_l is liquid molar volume, R is the universal gas constant, and r$_c$ is the radius of curvature. In micropores, the adsorbed gas is not considered as fluid interacting with the bulk (pore walls) as the physical properties (surface area and molar volume or density) of the confined fluid are assumed to be different from those of the bulk liquids [51]. Therefore,

Kelvin equation breaks down and fails for pore sizes in the micropore range as it underestimates them [52].

Methods, based on Kelvin equation, like Barret-Joyner-Halenda (BJH) [43] or the Horvath Kawazoe (HK) method [42] can be used to overcome the limitation of Kelvin equation by "extrapolating" it to small pore sizes (micropores). BJH model is widely accepted for the analysis of gas adsorption/desorption and it is based on considering the pore as a collection of cylinders. Simply, within the BJH method the total access of gas adsorbed in a pore is given by a pore filling part plus another part due to a surface layer of thickness t, this means that "r_c" in equation 1.6 is expressed as r_c = r - t where "r" is the real pore radius.

In the BJH method, the adsorption on the pore walls is described by an isotherm measured on a non-porous surface of the same chemical nature as the pore walls [48]. This assumption of modeling the adsorption on the pore walls by an isotherm measured on an isolated surface is only valid if the pore walls are far apart. In case of narrow pores, the molecules adsorbed to the opposing pore walls will interact significantly hence, the adsorption will be enhanced relative to that on the non-porous surface. This interaction between molecules on the opposing walls and the increase in the adsorption energy in micropores (due to the overlapping of the wall potentials) were neglected in the BJH method and in the model described in [54]. Based on aforementioned limitation for calculating the PSD in micropores, the Density Functional Theory (DFT) was proposed firstly for infinite slite pores in carbon [48] then it was developed to incorporate various pore structures and morphologies [55]. DFT method is based on a molecular model for nitrogen adsorption and it can reliably determine the PSD of micropores and mesopores. The experimental adsorption isotherm measured on a sample of a porous solid is considered as an aggregation of the isotherms for the individual pores that make up the pore structure of the solid. In mathematical terms, the experimental isotherm is the integral of the single pore isotherm multiplied by the pore size distribution. A detailed explanation of the method and derivation of its equations can be found elsewhere [45–48, 55, 56].

1.5.1.4 Pore volume

The total specific pore volume is defined as the liquid volume at a certain $\frac{P}{P_0}$ (= 0.95, after the pore condensation). This should be done if the isotherm showed a plateau-like in case of type IV and V [57]. Because in this case, the adsorbed amount measures the adsorption capacity and one can convert the adsorbed amount into a liquid volume to calculate the total pore volume by assuming that both the density of the adsorbate and that of the bulk liquid are equal at

saturation. If V_{ads} is the amount of adsorbed vapor at a relative pressure close to unity, the total pore volume, V_{liq}, is [58]

$$V_{liq} = \frac{P_a V_{ads} n_m}{RT} \tag{1.7}$$

where P_a is the ambient pressure, R is the gas constant, and T is the temperature in K. The specific pore volume is the sum of volumes of all pores in one gram of adsorbent. Pore volume, V_{liq}, specific surface area, $S_{sp.}$, and the average pore radius, $\overline{r}_p$ of cylindrical geometry, are related to each other by the following equation [36]:

$$\overline{r}_p = \frac{2V_{liq}}{S_{sp.}} \tag{1.8}$$

$S_{sp.}$ can be determined by BET model.

1.5.2   Mercury intrusion

Mercury intrusion porosimetry is valid for macroporous media and larger mesopores (4-10000 nm) [59]. Information obtained from the mercury intrusion can be divided into three types [58]: (i) volume and mass information-material volume, density, porosity, and percentage of filled porosity; (ii) information obtained from Washburn's Equation-pore volume distribution, specific surface area; and (iii) information of special or multiple methods-ratio between pore cavity and pore throat and PSD of pore throat. The only information obtained from Washburn's Equation will be discussed here which is more relevant to the gas sorption part. In contrast to the gas adsorption, mercury is a non-wetting fluid (contact angle > 90°) and hydraulic pressure must be applied to force mercury to enter the pore. Mercury intrusion porosimetry shows hysteresis-like gas adsorption (capillary condensation). In the mercury intrusion experiment, the volume of mercury entering the pores can be measured as a function of the applied pressure directly. This P-V information represents a unique characterization of the pore structure. It is known that the required pressure of mercury to be penetrated the pores is inversely proportional to the pore size or opening. This can be shown in Washburn equation:

$$P = \frac{2\gamma \cos\theta}{r} \tag{1.9}$$

where P is the applied pressure at which mercury enters the pore, γ is the surface tension of mercury ($0.485\ Nm^{-1}$), θ is the contact angle between mercury and the solid surface, and r is the cylindrical pore radius. From equation 1.9, the pore size can be directly obtained from pressure values with $0.485\ Nm^{-1}$
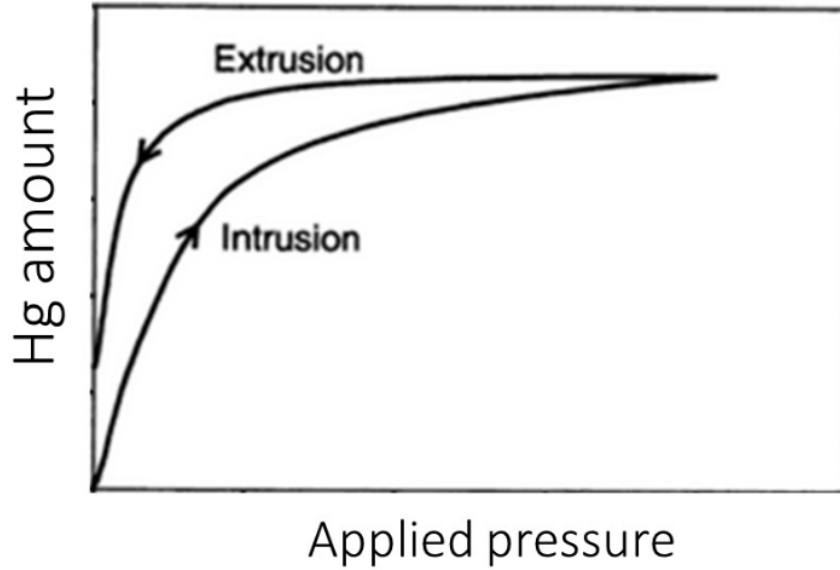
Figure 1.9: Intrusion-Extrusion hysteresis of Mercury intrusion modified from [61]).

mercury surface tension and 141 ° contact angle. It was found that mercury intrusion porosimetry agrees with data obtained from other methods and it produces pore sizes and volume which can be repeated better with a small standard deviation. The extrusion process is performed by the pressure reduction according to equation 1.9. Hysteresis between mercury intrusion and extrusion (figure 1.9) is a general feature of mercury intrusion porosimetry [61]. This hysteresis would have a lot of reasons such as the presence of ink-bottle pores (entrapping of mercury in the wider pores till emptying the narrower necks), different contact angle of mercury (during intrusion and extrusion), pore potential of pore walls (competition between extrusion and trapping due to the pore wall potentials), networking effect, surface roughness of the pore walls (contamination of the material's surface by mercury).

1.5.2.1 Pore size distribution

Pore size distribution produced by differentiating Washburn equation (equation 1.9) by considering both the surface tension and the contact angle as constants;

$$Pdr + r_p dP = 0 \tag{1.10}$$

where r_p is the pore radius. But according to [61], $dr = \dfrac{dV}{D_v(r)} dV/(D_V(r))$ so equation 1.10 reads;

$$D_v(r) = \frac{P}{r_p}\left(\frac{dV}{dP}\right) \tag{1.11}$$

where $D_V(r)$ is the pore size distribution, dV is the change in the pore volume, and dP is the change in the applied pressure. From equation 1.11, it is clear that the amount of mercury enforced to enter the pore will be increased as the applied pressure increased and the corresponding intruded volume will increase as well. The pore size distribution, $D_V(r)$, can be determined from the plotting of dV vs. dr. To probe pore sizes less than 10 nm by the mercury intrusion method, a very high pressure is required which may affect the porous structures or pore collapse and it can result in instrumental limitations for pores less 4 nm in size [59].

1.5.2.2   Specific surface area

Rootare and Prenzlow [62] have tried to calculate the specific surface area of porous materials directly from mercury intrusion data. They considered this method as a rapid check on gas sorption results. In this calculations, cylindrical pores having no bottle-ink pores were assumed. The reversible work required to intrude mercury to enter a cylindrical pore, dW_1, is given by:

$$dW_1 = -dS\gamma\cos\theta \tag{1.12}$$

where dS represents the surface area. This intrusion of mercury is done when an external pressure P forces a volume of mercury V into the pores exerting a work dW_2 on the pores where

$$dW_2 = PdV \tag{1.13}$$

dW_1 and dW_2 are equal and one can find by equating equations 1.12 and 1.13;

$$dS = \frac{PdV}{\gamma\cos\theta} \tag{1.14}$$

the total surface area of a sample is the summation of the surface area of all pores and it can be calculated by integrating equation 1.14 over all the range of pore radii intruded by mercury. So, the total porous specific area is given by:

$$S = \frac{1}{\gamma\cos\theta}\int_0^V P\,dV \tag{1.15}$$

It should be noted here that since the small pores are not measured by mercury intrusion, the results are not always comparable with those obtained from the BET method. Additionally, the assumption of the cylindrical pore shape makes the calculations so simple and their error would be large. So for concrete calculations, it is not recommended to use the specific surface area given by mercury

intrusion whereas the BET surface area is more accurate.

Although gas sorption and mercury intrusion are the widely used methods, they suffering from limitations. The using of gas or liquid restricts the detection of accessible (open) pores only. In the gas sorption method, the analyses of the PSD have many different methods and needs efforts. In mercury intrusion, pores with diameters < 4 nm cannot be detected as the pressurizing of mercury collapses the porous structure. So, the complete characterization of porous materials requires other additional methods. SAXS can be used as a porosimetry tool to detect open and closed pores by applying the Chord-Length-Distribution (CLD) theory. Curves given by the CLD theory give merging distributions having maxima due to pore sizes, pore walls, pore-to-pore distance and an exact assignment of each effect is quite difficult. Thus, a CLD analysis should be accompanied by another tool like gas sorption [63]. Scanning electron microscopy only gives information about pore sizes > 5 nm. A contrast improvement is indeed with the transmissions electron microscopy possible, however, the sample preparation is not trivial.

1.5.3 Positron Annihilation Lifetime Spectroscopy (PALS)

Positron Annihilation Lifetime Spectroscopy (PALS) offers a complementary and unique method for the characterizing porous materials in the range of 0.3-50 nm [64] (the highest accuracy lies in the 0.5-10 nm range [65]). Porosimetry by PALS relies on the correlation between the ortho-Positronium (o-Ps) lifetime and the pore size. When positron enters low-density materials such as insulators, gases, liquids, and porous materials, positron can form a bound state of positron and electron (produced during positron thermalization) called "Positronium" (Ps) which is a "hydrogen-like" atom [66–68]. In porous materials, Ps is attracted to the pores because they have an attracting potential for Ps. This Ps atom has two states depending on the relative spin orientations of the electron and positron [69]. When the spins of the electron and positron are parallel to each other, ortho-positronium (o-Ps) with an intrinsic lifetime in the vacuum of 142 ns is formed. While if they are antiparallel to each other, para-positronium (p-Ps) of an intrinsic lifetime in the vacuum of 0.125 ns is formed. P-Ps can be considered as a self-annihilating state as it is weakly affected by the surrounding media while o-Ps, inside the pores, will stay alive there for a definite time (depending on the size of these pores) before annihilation [70]. Some models were proposed to correlate the o-Ps lifetime inside the pores to the pore sizes by assuming certain shapes for the potential wells (pores) where Ps is trapped in. These models are described in details in section 2.8.

Since PALS is the main tool used in this thesis, and it contains a lot of details, comprehensive descriptions of PALS as a tool of porosimetry is given in the next chapter.

Chapter 2

Positron Annihilation spectroscopy principles

2.1 Introduction

When a positron (or Ps) and an electron annihilate, two or three (in case of o-Ps in very large pores or in vacuum) γ quanta are produced. The goal of Positron Annihilation Spectroscopy (PAS) is to detect a property of these quanta which give us some information about the site of the annihilation. When one measures the time difference between the birth of the positrons in the material and that of its annihilation, this means Positron Annihilation Lifetime Spectroscopy (PALS). Doppler Broadening Spectroscopy (DBS) means the measurements of the slight differences in energy of the 0.511 MeV annihilation quanta due to the energy and momentum of the electron in the positron-electron annihilation site. When the two γ quanta emitted, they can exhibit a deviation from the collinearity or the 180 ° back-to-back emission and the measurements of this deviated angle is the main concern of Angular correlation of annihilation radiation (ACAR).

The mean energy of the conventional positron source (^{22}Na) implanted into a solid is in the order of 200 keV [71]. These positrons are slowed down (thermalized) by the collision and excitation in the solid. The penetration depth of the positron depends on the material's density and positrons can screen the bulk of the material due to its relatively high energy. If the goal of the experiment is to measure defects or structure of thin films or to detect the structures at the surface or near the surface of a material, the conventional ^{22}Na source is not valid for this purpose. Slow Positron (SLOPOS) beam is suitable for the depth profiling of the material by tuning the energy of the implanted positrons allowing them to penetrate to a definite depth.

The detailed explanation of positron annihilation spectroscopy is described in the following sections which describe positron's and positronium's creation, in-

teraction with matter and annihilation, detection, data treatment, porosimetry by means of positronium annihilation lifetime, and finally slow positron beam.

2.2 The positron

The positron was predicted in 1928 by Dirac [72] as one of the big successes of relativistic quantum mechanics theory. The equation that relates the total energy E to the momentum p of a particle of rest mass m_o is;

$$E^2 = p^2c^2 + m_o^2c^4 \tag{2.1}$$

and it has two solutions which are $E = c\sqrt{p^2 + m_0^2c^2}$ and $E = -c\sqrt{p^2 + m_0^2c^2}$. The negative energy, as stated by Dirac, had a real physical meaning and it means that there is a negative energy sea or electron sea with negative energies extended from $-\infty$ to $-m_oc^2$. In this negative energy sea, a hole would show itself as a positive particle. This positive particle was assumed at first to be a proton [73] but by calculating the correction of Coulomb interaction, it was realized that the predicted particle was not proton because its mass was 1800 lighter than that of the proton. The new particle had the same rest mass and magnetic moment as that of the electron but with an opposite charge. The new particle was the positron. Experimentally, positron was observed in 1932 by Anderson [74, 75].

2.3 The positronium

The positronium (Ps) is a bound state of a positron and an electron. Its energy levels and orbits are similar to hydrogen [76]. The annihilation of the Ps is governed by a selection rule. If S is the total spin of the Ps and L is its total orbital momentum, so we have

$$(-1)^{L+S} = (-1)^N \tag{2.2}$$

where N is the number of the emitted photons. For singlet state, the equation is correct only when N is even, while for triplet stat Ps must annihilate by the emission of an odd number of photons. It was observed that the two photons (singlet) and three photons (triplet) decays have high probabilities in comparison with any other decay.

In insulating materials, positron can form Ps. The formation of Ps in metals and semiconductors is rare as a result of the high electron density. In some case, positronium can be formed in these materials at the surface and internal surfaces of voids. There are three models to describe the Ps formation:

Ore model$\longrightarrow$ Ps (of E_b binding energy) formation is possible when the positron energy satisfies the following inequality and lies in the ore gap E_g

$$E_{ion} - E_b < E_g < E_{ex} \tag{2.3}$$

where E_{ion} is the atomic or molecular ionization energy and E_{ex} is the excitation energy of its electrons. Accordingly, hot positrons will combine with hot electrons (kicked out from the molecule) to form Ps. Ore model is used to describe Ps formation in gases but it is unsuitable to be applied for liquids because the Ps binding energy there is about 0.1 eV [77, 78].

Spur model$\longrightarrow$ Ps can be formed as a result of the interaction of the positron with the ionized electronic spur generated during the positron thermalization. The spur contains a cluster of ionized electrons, positive ions and possibly radicals which generated at the end of the positrons flight and they are close together. When the positron comes close to one of the spur electrons before its recombination with other species, Ps will be formed. According to this model, the recombination of Ps is ignored [79].

Blob model$\longrightarrow$ In contrast to spur model, blob model assumes that at the end of positron track the ionization of molecules will be efficient with a decreasing in the distance between glancing collisions (collisions responsible for ion-electron pairs creation inside a spherical shape with 30-70 Å [78]) caused by positron's energy reduction. Therefore, spurs overlap with a great number of created ion-electron pairs. The required energy of positron to form a blob, E_{bl}, is 500 eV, and positrons with $E < E_{bl}$ will diffuse through a nonlinear path but inside a sphere of radius 40 Å [80]. Inside the blob, positron can either be trapped, thermalized, and form Ps or it can escape from the blob and annihilate outside it without forming Ps. The formation of Ps according to the blob model is depicted in figure 2.1.

2.4 Positron production

Positrons can be obtained either by the decay of radioactive isotopes or by the pair production process.

2.4.1 Radioactive isotopes

Positrons can be produced by the β decay of radioactive elements like ^{22}Na, ^{58}Co, and ^{86}Sr. Practically, positron source must have the following characteristics:
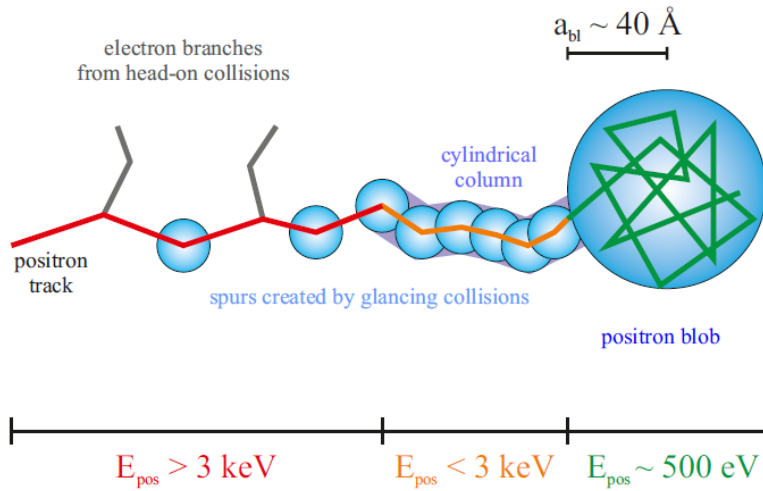
Figure 2.1: Description of Ps formation according to the blob model (from [78, 80])

- The source must have a relatively long half-life time in order to be used through a series of experiments.

- The positron yield must be sufficiently high.

- The source must be available commercially and its production and handle are easy.

^{22}Na is the preferred source for long-term measurements because it offers a good compromise between cost per Bq and half-lifetime (2.6 y). Additionally, the biological half-lifetime of ^{22}Na is a few days [72]. ^{22}Na positron source is available for activities up to 3.7 GBq [81]. For studies of bulk materials, conventional (non- moderated) ^{22}Na is the best choice because, as shown in its decay diagram (figure 2.2), it decays to the first excited state of ^{22}Ne by the emission of positrons (yield of 90.4%) and electron capture (with 9.5%). The first excited state of ^{22}Ne has a very short lifetime (3.7 ps) and it de-excited to the ground state of ^{22}Ne by the emission of a photon of 1274 keV energy. Thus we can say that both β particles and γ photons are produced at the same time so we can use the γ photon as an indication of the birth of the positron (the start signal). After interacting with the material of interest, positron will annihilate with an electron giving a 511 keV photon (the rest mass energy of the positron) (the stop signal). The time difference between the start (E_γ=1274 keV) and stop (E_γ=511 keV) signals is the positron lifetime. The decay diagram in figure 2.2 is according to:

$$^{22}Na \longrightarrow^{22} Ne + \upsilon_e + \gamma \Rightarrow^1_1 p \longrightarrow^0_1 e + \upsilon_e + \gamma (Dirac) \qquad (2.4)$$
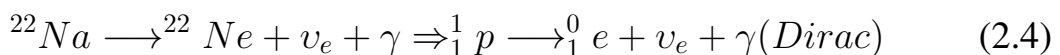
Also, ^{22}Na is available in a dilute Na $_2$CO$_3$ solution which is easy to handle and
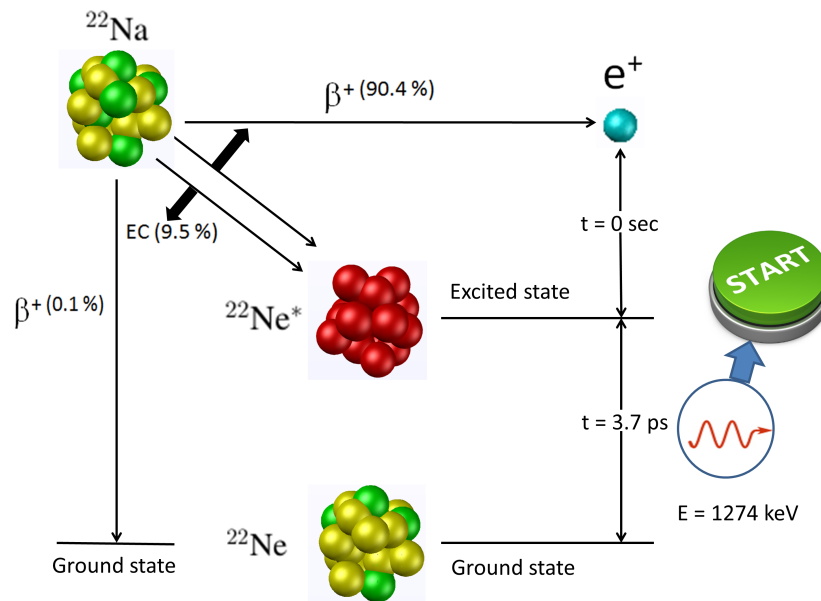
Figure 2.2: Decay scheme of the radioactive isotope ^{22}Na (based on [72]).

chemically stable.

Radioactive isotopes can be produced artificially by irradiation. For example, ^{63}Cu can be irradiated in the core of a research reactor to give ^{64}Cu radioactive isotope via the reaction ^{63}Cu(n,γ)^{64}Cu, the strong ^{64}Cu source is a self-moderator and it gives eV slowed positrons but its main problem is its low half-time (12.7 h) which means that the source will require regular replacements [81].

2.4.2   Pair production

Pair production is a method used to create positrons in the positron beams. In this method, an electron beam of a LINear ACcelerator (LINAC) is hitting a high atomic number target such as W, Pt, or Ta causing bremsstrahlung γ radiations. These γ radiations are highly energetic hence, they can penetrate into thick ($\sim$ cm) samples. After their interaction with matter, these γ radiations can create electron-positron pairs, because the γ radiations have energy $E_\gamma > 1.02$ MeV ($> 2m_e c^2$, the condition of pair production), deep inside the sample. This way, positrons can be created and annihilated inside thick samples whereas the conventional ^{22}Na of 540 keV endpoint energy is not enough to probe such thick samples as its information depth is limited (depending on the density). The use of this idea is applied in the Gamma-induced Positron Annihilation Spectroscopy (GiPS) system at ELBE-HZDR facility. On the other hand, the highly energetic γ radiations can enter a converter, in the vicinity of their cre-

ation, where the pair production process occurs inside it and electron-positron pairs are created. The produced positrons can be extracted and moderated (e.g. 3 eV in case of W) which, in turns, can be guided for surface and thin layers studies (Monoenergetic Positron Source (MePS) at ELBE-HZDR).

2.5   Positron interaction with matter

Positron annihilation is a non-destructive technique used for the detection of defects and structure of materials. It competes with other techniques like XRD, SEM, .., etc. due to its sensitivity to defect type and concentration. In order to understand how positron annihilation identifies defects, we need at first to know the mechanism of its interaction with matter. To use the positron as a probe, a positron source is prepared to match with the practical conditions. Positron drops taken from a Na_2CO_3 solution are deposited on the surface of a polymer material like Kapton foil or on the surface of Al foil to prevent the sample contamination and to re-use the source for additional measurements. After preparing the source and its foil cover, the source is enclosed between two identical samples ("sandwich" configuration) as shown in figure 2.3. In the sandwich
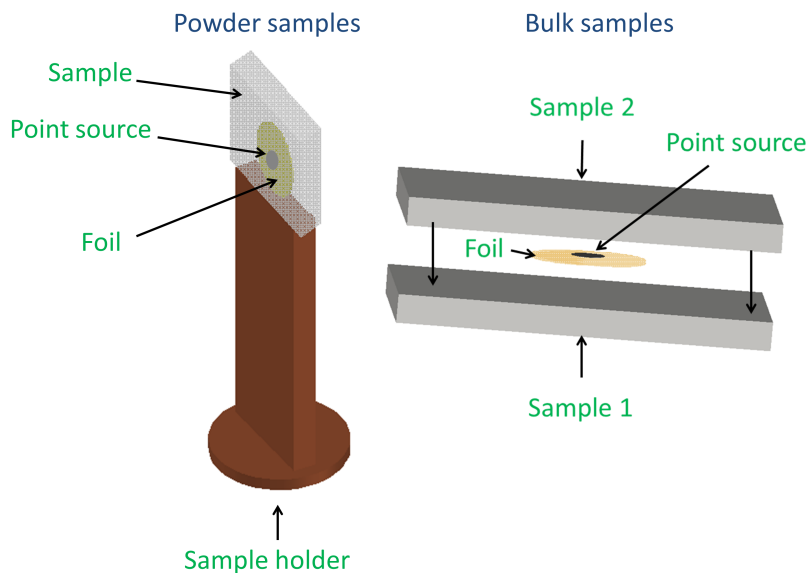
Figure 2.3: Scheme of the sample–source sandwich arrangement (modified from [72]).

configuration, the samples' thickness depends on their mass density in order to get 100% of positron annihilating in the sample (e.g., Si sample with $\rho \sim 2.3$ g.cm^{-3} the smallest required thickness for each sample of the pair should be $\sim$ 400-500 μm whereas for porous material with $\rho \sim 1$ g.cm^{-3} it was found to be

$\sim$ 1200-1600 μm) (500 μm is enough to stop 90 % of positrons, see appendix A.1).

Upon entering the material, energetic positrons lose their energy by the collisions with the electrons and ions of the medium by creating electrons-ions (holes) pairs and at lower energies by positron-phonon interaction. Positron finally comes to thermal equilibrium with its environment. After being a thermalized particle, with a mean energy$< E_{th} > = \frac{3}{2} K_B T \approx 40$ meV, positron starts the diffusion in the material and its typical diffusion length in the order of 100 nm and it depends on the host material. Positron can interact with defects during the diffusion process and trap in these defective sites because of their attraction potential for positrons. After the trapping, positron annihilates with an electron of its surrounding and produce γ rays. These processes can be summarized in figure 2.4. The annihilation signal provides information about
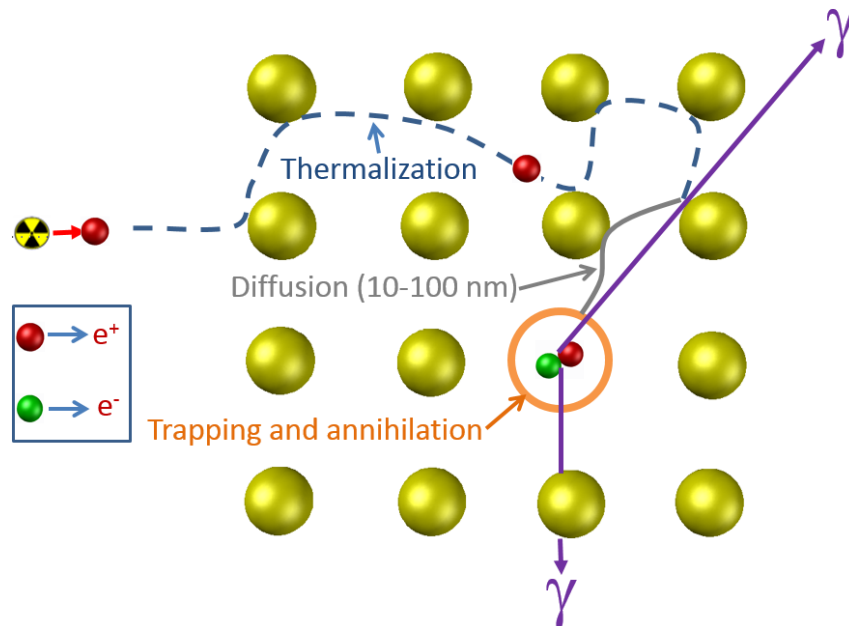
Figure 2.4: Schematic diagram shows a single positron penetrating through matter undergoes various processes influencing the state from which the positron annihilates with an environmental electron.

nature of the localized state and the defect itself.

2.5.1   Positron trapping model in metals and semiconductors

The positron traps (open-volume) have an attractive potential for positrons owing to the missing of the repulsion force of the nuclei. To describe the trapping process of thermalized positrons, a trapping model must be formulated assuming that defects are distributed homogenously in the material. The idea behind

the trapping model is to set some conditions and assumptions to describe the defect and measure the parameters of that model. Then to identify the defects because the trapping model analyses aim to determine the trapping rate and defect concentration. To show a simple example of positron interaction and annihilation in metals and semiconductors, the single defect trapping model is described below.

2.5.1.1   One defect trapping model

In this part, the quantitative estimation of the defect parameters will be discussed. As a result of the mutual interactions between the positrons and the host material, the thermalized positron is obtained. In case of one defect type exists in a sample, thermalized positrons may annihilate from the delocalized state in the defect-free bulk with annihilation rate λ_b. Also, another fraction of positrons can be trapped in the defect with a trapping rate κ_d when the defect concentration is high enough to trap these positrons. After some time, positrons trapped in the defect will annihilate with the emission of γ quanta with annihilation rate λ_d. The lifetime of positron annihilating from defect, τ, is the reciprocal of λ_d. These processes are shown in figure 2.5 and the rate equations of annihilation can be expressed as following [72]:
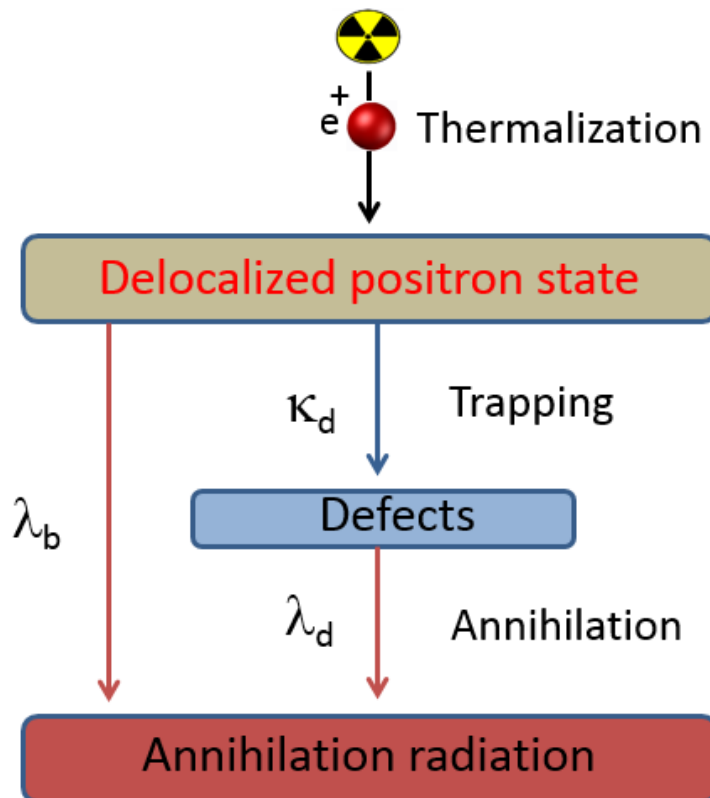
Figure 2.5: Description of the one-defect trapping model [72].

$$\frac{dn_b(t)}{dt} = -(\lambda_b + \kappa_d)n_b(t)$$

$$(2.5)$$

$$\frac{dn_d(t)}{dt} = -\lambda_d n_d(t) + \kappa_d n_b(t)$$

where n_b and n_d are the numbers of positrons in the bulk and defect, respectively. λ_b and λ_d are, in respect, the annihilation rates in the bulk and defect and κ_d is the trapping rate of the defect. At t = 0, $n_b(0) = N_0$ (the total number of positron at t =0) and $n_d(0) = 0$. Using these initial conditions, the solution of equation 2.5 gives the decay spectrum of positrons,

$$D(t) = I_1 exp(-\frac{t}{\tau_1}) + I_2 exp(-\frac{t}{\tau_2}) \qquad (2.6)$$

where $\tau_1 = \dfrac{1}{\lambda_1} = \dfrac{1}{\lambda_b + \kappa_d}$ is the bulk lifetime (defect-free sample) and $\tau_2 = \dfrac{1}{\lambda_d}$ is the defect lifetime which is constant for a specific defect and changes only with any change in the size and the type of the defect. Their corresponding intensities are

$$I_1 + I_2 = 1, \qquad I_2 = \frac{\kappa_d}{\lambda_b - \lambda_d + \kappa_d} \qquad (2.7)$$

The lifetime spectrum is the first derivative of the decay spectrum i.e.

$$N(t) = |\frac{dD(t)}{dt}| = \frac{I_1}{\tau_1} exp(-\frac{t}{\tau_1}) + \frac{I_2}{\tau_2} exp(-\frac{t}{\tau_2}) \qquad (2.8)$$

The trapping rate is proportional to the defect concentration C_d according to the following equation

$$\kappa_d = \mu C_d = I_2(\frac{1}{\tau_1} - \frac{1}{\tau_2}) = \frac{I_2}{I_1}(\frac{1}{\tau_b} - \frac{1}{\tau_d}) \qquad (2.9)$$

where μ is the trapping coefficient, τ_2 is determined experimentally from the decomposition of the two- components of equations 2.6 and 2.7. Worth mentioning, τ_2 is identical to τ_d as it is a measure of the reduced electron density in the open-volume defect thus, it is longer than the bulk lifetime. τ_d is independent of the defect concentration, it can be taken as a characteristic value of the open volumes. The average lifetime which is given by

$$\tau_{avg} = \sum_{i=1}^{k+1} I_i \tau_i \qquad (2.10)$$

is used widely because it can experimentally be determined but it is insensitive to the fitting procedure applied. The relation between the trapping rate and the

average lifetime (when τ_b and τ_d are known) is given by [72]

$$\kappa_d = \frac{1}{\tau_b}\frac{\tau_{avg} - \tau_b}{\tau_d - \tau_{avg}} = \frac{\eta}{\tau_b(1 - \eta)} \tag{2.11}$$

where η is the annihilation fraction and it is obtained by

$$\eta = \int\limits_0^\infty n_d(t)\,dt = \frac{\kappa_d}{\lambda_b + \kappa_d} \tag{2.12}$$

When the defect concentration is high and the spacing between defects is much smaller than the positron diffusion length in the bulk, one component spectrum with average lifetime, τ_{avg}, $= \tau_d$ and $I_2 = 1$ is obtained and only lower limit of defect concentration can be given which means a saturated trapping.

2.6   Positronium interaction with insulators

When positrons enter an insulating material (e.g., porous material), and after thermalization and diffusion, it might be that some free positrons reach a place having a high electronic density and annihilate by two γ emission. On the other hand, 10-50 % [82] of these positrons can form Ps either by capturing a bound molecular electron (hot positrons) or combining with free electrons from the ionized electronic spur (slow positrons). The formed Ps has two states of p-Ps and o-Ps with a 1:3 formation probability, respectively. The lifetime of p-Ps is short and it varies slightly according to 125ps / η, where η represents the relaxation of Ps [83] in the matter. While the lifetime of o-Ps is strongly affected and changed (from its intrinsic value of 142 ns to a few nanoseconds) due to interaction with the matter. The reduction of the o-Ps lifetime may be caused by one of the following processes [84]:

- Pick-off annihilation

- Spin conversion

- Chemical reaction

Pick-off annihilation is the most common process applied to all substances and it is independent of their properties while the other two processes are applied to processes which form the Ps chemistry like oxidant and paramagnetic substances. In pick-off annihilation process, o-Ps interacts with the matter and its lifetime decreased. The interaction occurs between an o-Ps and an electron with an opposite spin from the media. Two γ photons are emitted as a result of the

pick-off annihilation with a decrease in the o-Ps lifetime. The annihilation rate of the pick-off process depends on the electronic properties of the media. O-Ps interacts with media's molecular electronic cloud as [84]

$$\lambda_p = \frac{1}{\tau_p} = \frac{N_A}{M\rho\upsilon\sigma_p} \tag{2.13}$$

where λ_p is the annihilation rate of the pick-off, N_A is the Avogadro number, M is the molecular weight of the media, ρ is the density of the media, υ is the positron's velocity in the media, σ_p is the efficient section of the annihilation by pick-off. However, one has to relate the annihilation rate of the pick-off λ_p and the characteristic of the material of concern because both υ and σ_p can't be calculated directly.

2.7 Annihilation detection

The signals of either positrons or Ps annihilation can be detected by the different positron annihilation spectroscopies (i.e. PALS, DBS, and ACAR) as shown in figure 2.6. For defect identification, PALS and DBS are used predom-
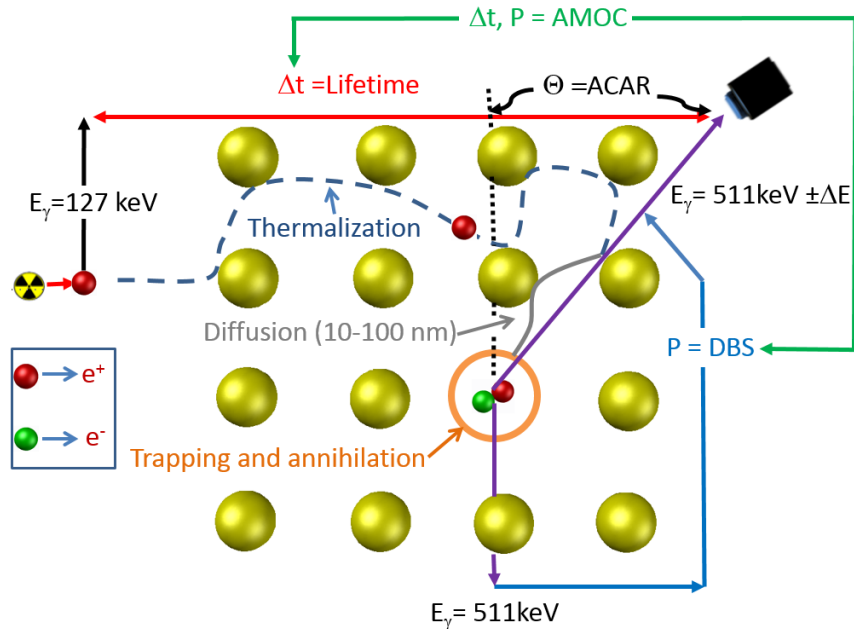
Figure 2.6: The scheme of positron experiments (PAS techniques) (modified from [72]).

inately while ACAR is used for studies of the bulk electronic structure. The presence of defects (mono-vacancies, vacancy clusters, dislocations, and voids) in the materials affects the mechanical and electrical properties. The detection of the annihilation signals could offer a clear vision of theses defects and help

for understanding material's properties. Another importance of defect identification by the PAS is in semiconductors. Such an identification is important as the vacancy-type defect plays a crucial role in the electrical and optical properties of semiconductors and the functionality of semiconductors can be changed through the defect engineering. Porosimetry by calculating the pore size, pore distribution, and pore interconnectivity of closed and open pores is also important because it gives a clear porous mapping of the material of interest. PALS is a powerful technique for such a porosimetry.

In the next section, the principles of PAS will be discussed in details

2.7.1 Positron Annihilation Lifetime Spectroscopy (PALS)

PALS is a measure of the time difference between the emission of the positron and the detection of the annihilation photons. The birth of the positron in the material is marked by the detection of a 1.27 MeV γ ray which is emitted from a ^{22}Na source simultaneously (after 3.7 ps) with positron creation. While the annihilation is defined by the detection of either a 0.511 MeV annihilation photon (in the 2γ annihilation in metals, semiconductors, and pick-off process in porous materials) or 0-0.511 MeV annihilation photons (in the 3γ annihilation of o-Ps in vacuum). The sum of the energy in the 2γ annihilation or the 3γ annihilation is 1.022 MeV. A PALS measurement is made by collecting and storing the individual lifetimes of positrons in a histogram giving the overall positron lifetime spectrum. To enhance the statistics which is necessary for data fitting, a high number of counts or events must be stored. The time resolution is a very important characteristic of the lifetime spectrometer. It is affected by different factors like the scintillators (type, dimensions, shape), the photomultiplier tube (PMT) (applied high voltage and transit time spread), the pulse shaping, and the radiation interaction in addition to the used electronic modules. The time resolution is characterized by the Full-Width at Half-Maximum (FWHM) and its minimization is the goal of many researchers. Values of FWHM vary from 200 to 300 ps are common for the PALS timing resolution. The count rate or the rate of data collection is another important parameter of the spectrometer especially in case of volatile samples and spectrometers having instabilities with time. Positrons will annihilate from different lattice sites (bulk and defected sites) with a characteristic lifetime ($\tau_i = \frac{1}{\lambda_i}$) for each component following an exponential decay shape (equation 2.6) and the positron lifetime spectrum is the summation of the first derivatives of these decays (summation of equation 2.8)

$$N(t) = \frac{dD(t)}{dt} = \sum_i \frac{I_i}{\tau_i} exp(-\frac{t}{\tau_i}) \qquad (2.14)$$

where I_i are the relative intensities and $\sum I_i = 1$.

The lifetime spectrum is convoluted with the time resolution function of the spectrometer. This resolution function, $G(t)$, may be one simple Gaussian function (in case of the plastic detector) or one, two, or three complex Gaussian functions (in case of Barium florid, BaF_2). Generally, the resolution function has the following form ([72]):

$$G(t) = \frac{1}{\sigma\sqrt{\pi}} exp(-(\frac{t - \tau_0}{\sigma})^2) \tag{2.15}$$

The term $t - \tau_0$ appears in this equation because there is a shift in time due to the use of delay cable (in case of the analog spectrometer). The time resolution is characterized by the Full Width at Half Maximum (FWHM) as FWHM = 2 $\sigma_s\sqrt{ln2}$ where σ_s is the standard deviation.

Digital Positron Annihilation Lifetime Spectroscopy (DPALS) is used in the course of this work and it is the topic of the next section.

2.7.1.1 Digital Positron Annihilation Lifetime Spectroscopy (DPALS)

The DPALS needs few pieces of equipment [86] as it composed of, as shown in figure 2.7, two scintillation detectors coupled to two PMTs, one high voltage module, one coincidence unit, and a fast digitizer connected to a PC. The anode
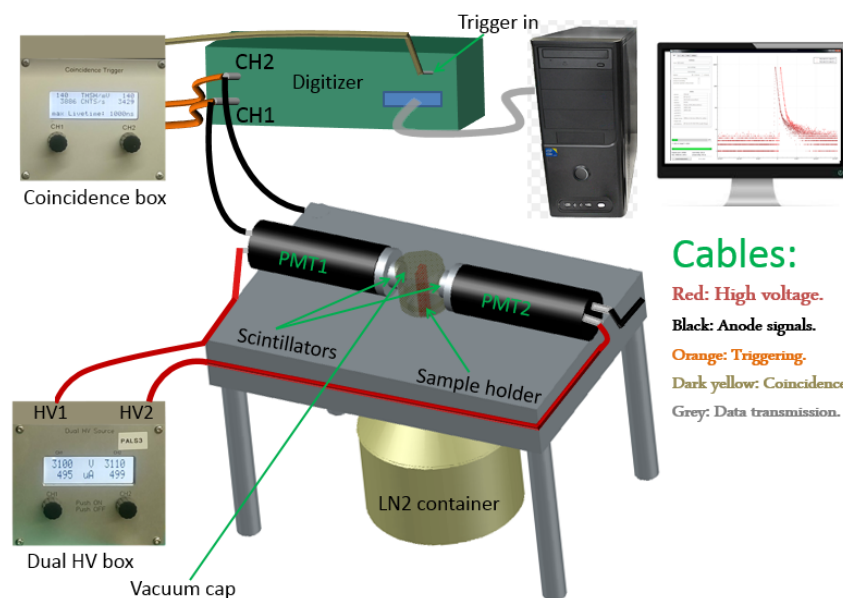
Figure 2.7: Illustration of the digital positron lifetime spectrometer.

pulses from the PMTs are converted to digital values in the digitizer and sent to a PC for processing. The time information is then analyzed from the voltage sample sequences from the software on the PC. The sampling rate must be sufficiently high (at least 2GS/s) to capture the leading edge of the detector's signal

to enhance the time resolution [86] in order to get a timing resolution purely determined by the detectors. There are some advantages of the DPALS over the analog one such as [86, 87]

- Easy setup, reduced size, cabling, power consumption, and cost

- Energy, timing, and pulses analysis are done on a PC using a software

- Faster tuning and calibration and very accurate time determination

- It can work with very small detector pulses (few millivolts)

Here, the digitization process means the conversion of the analog pulses to digital values by an Analog-to-Digital Converter (ADC) unit for a number of samples following a trigger event. These events are moved into a memory buffer available for readout. In the start-of-the-art of DPALS, digital oscilloscopes were used and showed a comparable performance to an analog spectrometer but with a low data throughput (15 count per second) [88]. Later on, this problem was resolved by using a commercial digitizer with a sampling rate of 2GS/s, 8-bit amplitude resolution, and 500 MHZ analog bandwidth [87] which allowed the storing and analysis rate $\geq$3000 event per second. Also, digitizers allow the triggering syncing between multiple units and they are equipped with higher bandwidth readout suitable for high counting rates. Digital coincidence systems using digitizers allow for software-based event correlation which means that the pulses information is preserved as all of the digital information is passed to PC for processing.

Timing process and data storage

After reading out the anode data, a software inverts the values and searches for the first value above the software threshold (the point I in figure 2.8.a). The area around this spot is separated to improve the performance. This separated area is interpolated by a cubic spline interpolation. After the interpolation, the interpolated maximum of the pulse is obtained with a smoothed leading edge. The interpolated maximum shall be multiplied by the constant fraction level. The first interpolated point above this constant fraction value will be searched at the leading edge of the pulse. Thereafter, the interpolated points below and above the constant fraction value are used for a linear fit with two points to get the exact value of the signal time zero (figure 2.8.a, inset). If a start-stop pair is measured and the signal time positions are well defined, the positron lifetime is the difference between these two values. The digitizer is triggered by a self-designed coincidence trigger unit. Basically, the trigger is executed if there are pulses in two channels above the threshold. Thereby the first pulse started a definite time window, which is closed by the second. If both pulses are measured
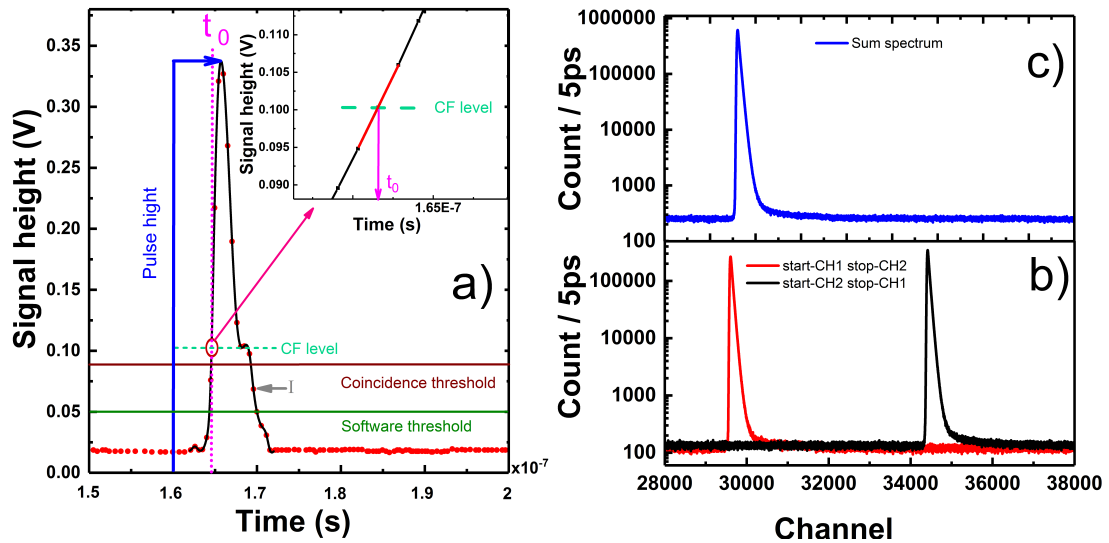
Figure 2.8: a) Digital timing process with constant fraction principle with flipped anode pulse of one pulse only; b) Two-lifetime spectra with 140ps FWHM. Red points represent start signal from PMT 1 and stop signal from PMT2 and black points according to PMT1-stop signal and PMT2-start signal combination; c) The calculated sum spectrum after shifting spectra.

within this window the trigger will be executed.

The digital lifetime is sorted equivalently to the analog system in a histogram. In contrast to the analog system, the fixed channel width of the analog spectrometer is free in the digital one as well as the definition of both start and stop signals. This means that with two PMTs, it is possible to get two spectra simultaneously; one spectrum with PMT 1- start and PMT 2-stop and vice versa (see figure 2.8.b). For this reason, it is possible to improve the count rate by the DPALS according to n(n-1) number of simultaneous spectra rule where n represents the number of the used PMTs. To sum the two spectra in figure 2.8.b, a parabolic fit around the highest channel to get the real maximum of the spectra is applied. Thereafter, both spectra are shifted into this channel and sum up both spectra to get a new sum spectrum, which has nearly the same result as the average of the two individual spectra and it includes the statistics of both spectra as shown in figure 2.8.c (double statistics).

Different routines are used to extract the positron lifetimes and their intensities from the decay spectrum and the physical model function must be convoluted with appropriate instrument functions. The theoretical function will be fitted to the experimental data using non-linear least square fitting and provides optimum values for the model parameters. Fitting codes used for the decomposition of the lifetime spectra are LT [89] or PALSfit [90]. The common of these routines is that the physical information is linked to specific lifetimes. The positron

---

[1]Maximum Entropy of LifeTime

lifetime distribution in the sample can be obtained by fitting the experimental data by the MELT[1] program. MELT gives the number of lifetime components of a sample which is an advantage of MELT [91] over LT but MELT is a time consumer because it needs very high statistics and it is very sensitive to τ_0 which should be defined precisely.

2.7.2   Doppler Broadening Spectroscopy (DBS)

When a positron annihilates with an electron, the conservation laws of both energy and momentum must be conserved. In the case of two-photon annihilation, one can write for the momentum and energy conservation laws [92]

$$k_1 + k_2 = 2mv$$

$$k_1 c + k_2 c = 2mc^2$$

(2.16)

where k_1 and k_2 are the photons momenta, m is the relativistic electronic mass, v is the velocity of the pair's center of mass in laboratory reference frame, and E is the total energy positron-electron pair.

In laboratory frame, the center of mass is assumed to be fixed ($v = 0$) and the two photons will fly in opposite directions with respect to each other. But in center of mass frame which has $v \neq 0$, an angle appears between the two emitted photons as indicated in figure 2.9. The momentum of the positron and electron
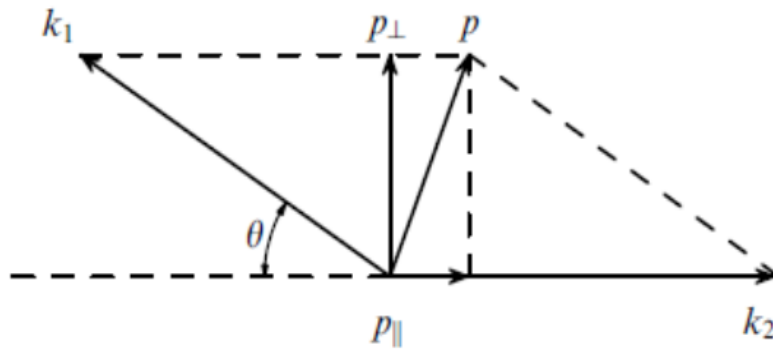
Figure 2.9: Vector representation of the momentum conservation in 2γ annihilation. P is the momentum of the electron-positron pair [92].

can lead to Doppler shift of the emitted photons. The total momentum of the electron-positron pair along the x-axis is $p_{||} = \text{M } v$ with $\text{M} = 2m$, the total mass of the particles. If ν is the frequency of a moving light source along the x-axis, the observed frequency shift can be written as

$$\Delta \nu = \left(\frac{v}{c}\right)\nu$$

(2.17)

where c is the light speed. The energy of the emitted photon, E, equals to $h\nu$, (h is Planck's constant). The energy of Doppler shift, ΔE, is

$$\Delta E = h\Delta\nu = (h\nu)(\frac{\upsilon}{c}) = E(\frac{p_{\parallel}}{Mc}) = E(\frac{p_{\parallel}}{2mc}) = (mc^2)(\frac{p_{\parallel}}{2mc}) = \frac{cp_{\parallel}}{2} \quad (2.18)$$

Since the annihilation process takes place only when the positron becomes thermalized so, at RT its momentum is neglected as its energy is $\sim$ KT. Accordingly, it is possible to consider that $p_{\parallel}$ is the momentum of the electron only. This assumption simplifies the investigation of samples with DBS because it gives a pure picture of the electronic structures and defects exist in the samples. Since the probability of the two γ emission is possible in two directions, so both positive and negative energy shifts are measured which gives rise to the Doppler broadening of the annihilation line of 511 keV (511±ΔE) and Doppler spectrum is an accumulation of numerous annihilation events.

2.7.2.1 Measurement of DBS parameters

To measure the Doppler broadening, a high purity Ge (HPG) detector, cooled by liquid Nitrogen (LN$_2$), is used. When the γ annihilation photons strike the detector crystal, electron-hole pairs are created. The charge separation is performed by the application of a high voltage to the detector and the separated electrons generate an electronic pulse which is fed to a preamplifier. The amplitude of this electric pulse is proportional to the energy of the incident annihilation photon. The output of the preamplifier is connected to an amplifier and these signals are stored after digitization into a Multi-Channel Analyzer (MCA). A block diagram of DBS is shown in figure 2.10. There are two line shape pa-
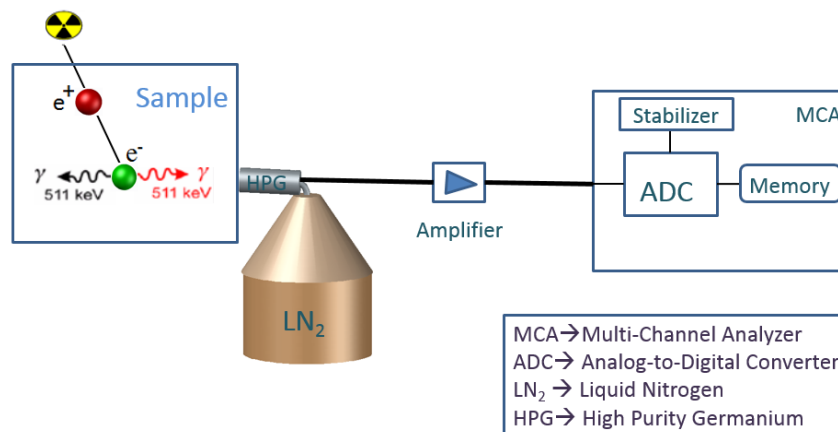
Figure 2.10: Schematic diagram of the Doppler broadening experiment [72].

rameters used for describing the Doppler broadening. These two parameters are used to detect positron annihilation with core and valence electrons. For

detecting valence annihilation, S- parameter is used which gives the number of events of the central low momentum region, N_s, divided by the total area under the curve N_0, without background [72]. In case of the presence of a defect in a sample, the annihilation with valence electrons will increase and hence, the value of S- parameter increases as shown in figure 2.11. Mathematically,
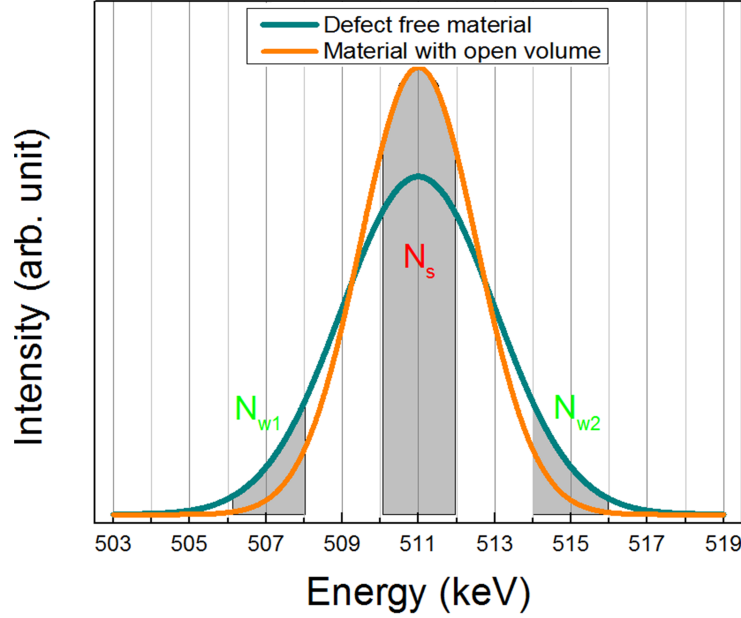
Figure 2.11: Defination of Doppler broadening line shape parameters of the 511 keV for materials with and without open volume defects [72].

S-parameter is given by

$$S = \frac{N_S}{N_0}, \qquad N_s = \int_{E_0-E_S}^{E_0+E_S} N_D \, dE \qquad (2.19)$$

where N_D is the Doppler broadening spectrum.

The line shape parameter of positron annihilation with core electrons parameter, W-Parameter, is defined as the number of events in the wings, N_W divided by the total number of events under the curve N_0. From this definition, it implies that W-parameter decreases as a function of the defect concentration found in the sample

$$W = \frac{N_W}{N_0}, \qquad N_W = \int_{E_1}^{E_2} N_D \, dE \qquad (2.20)$$

The limits of both S and W must be fixed for all spectra to be compared. The interval limits of S are chosen to give S of 0.5 for a defect-free sample. The

limits of W parameter must be chosen to be far away from the limits of S parameter. S and W parameters can be used to identify the type and concentration of defects but W parameter is more sensitive to the chemical surrounding of the annihilation site. Beside S and W parameter, a third parameter, R, can be used to give us the defect type [93]. Its absolute value is,

$$S = |\frac{S - S_b}{W - W_b}| = |\frac{S_d - S_b}{W_d - W_b}| \tag{2.21}$$

where S_b and W_b are the parameters for bulk defect-free samples and S_d and W_d for defected samples. The slope of the straight line through (S_b and W_b) and (S_d and W_d) gives the value of R for one defect type. On another word, we can say that the S-W diagram can be used to evaluate the number of defects in the sample.

2.7.3   Angular correlation of annihilation radiation (ACAR)

ACAR also measures the momentum of the annihilation photons of the electron-positron pair as it measures the angle between the emitted 511 keV photons [82] (rather measuring their energy broadening, like DB). Once the annihilating pair moves relative to the lab frame, a small angle, θ, appears (figure 2.9) between the produced photons [82]. From figure 2.9, we can find that $\sin(\theta) = \frac{p_\perp}{m_0 c^2}$ but for $p_\perp \ll m_0 c^2$, one can write,

$$\theta \approx \frac{p_\perp}{m_0 c^2}$$

where $p_\perp$ is the perpendicular momentum component. The deviation angle, θ, can be measured in a coincidence measurement because γ annihilation photons are produced simultaneously [72]. The coincidence count rate is the integral of the momentum distribution of the annihilated photons versus the momentum component in the propagation direction. The angular resolution is measured by lead slits and can be adjusted from 0.2 to 5 mrad [72].

2.8   Positron annihilation lifetime as a tool of poro-simetry

In this section, the Ps term is referred as to o-Ps because the p-Ps cannot be used in the porosimetry due to its short lifetime.

2.8.1   Tao- Eldrup (TE) model for small pores (Radius < 1)

In this model, the Ps atom is considered to be a single scalar particle trapped in the ground state of an infinite spherical potential well [94–96]. The assumption of Ps ground state occupation restricted the investigated pore size to be small because its applicability for large pores requires the insertion of the excited states (with a pore of width l, the energy level separation, $E_n, \propto \frac{1}{l^2}$). To simplify the picture, according to figure 2.12, the o-Ps is confined in a potential well of height V and radius R. In vacuum (center of the potential well), Ps has 142 ns lifetime but this lifetime will be reduced due to the interaction of the Ps with electrons in the wall of the potential well.

Mathematically, solving the Schrödinger wave equation of a particle in a spherical potential well of radius R and the condition of the finite wave function at 0 and ∞, the Ps wave function, ψ, give:
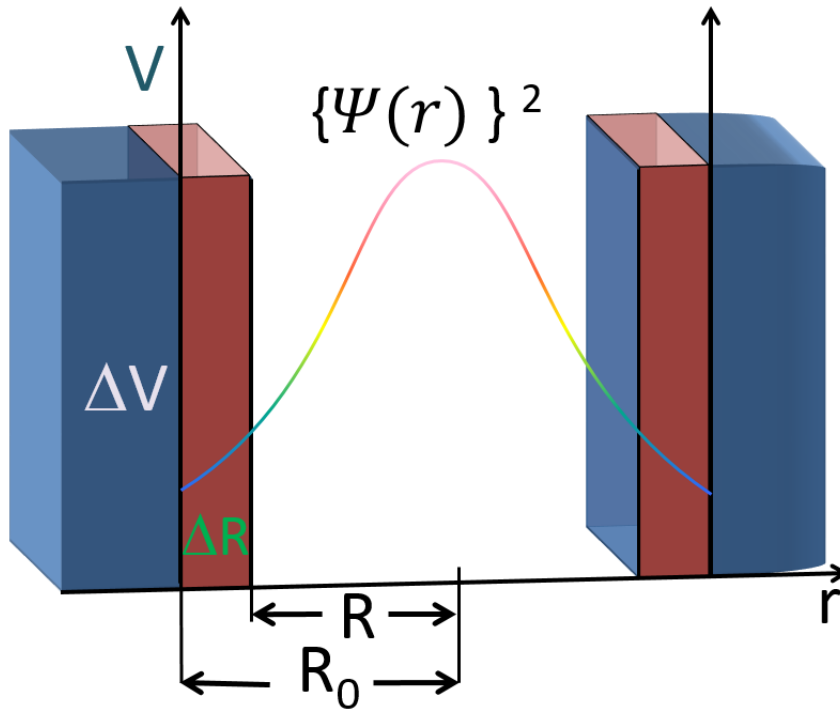
Figure 2.12: TE model for small spherical pores and a rectangular potential well of radius R and height V. The thickness of the overlapping region (pick-off) annihilation is ΔR and its height is ΔV. The o-Ps wave-function occupies the ground state of the infinite potential well.

$$\psi = \begin{cases} \dfrac{A\sin(k_1 r)}{r} & for \qquad 0 \le r \le R \\ B\dfrac{e^{(-k_2 r)}}{r} & for \qquad r > R \end{cases} \qquad (2.22)$$

where A and B are constants and $k_1 = \dfrac{\sqrt{2m(E-V)}}{\hbar}$, $k_2 = \dfrac{\sqrt{2m(E-\Delta V)}}{\hbar}$ and r is any distance measured from the center of coordinates. But for a Ps in a pore, the electron density is zero for $r < R$ (inside the pore, figure 2.12) while it is constant (but non-zero) in a layer between R and R_0 [95]. Tao [94] has suggested that this constant-electron density-layer (ΔR) is there due to the attraction between Ps and the surrounding molecules. This means that the original pore radius, R_0, will be reduced by ΔR thick layer. The electronic wave function in this ΔR layer will overlap with the Ps wave function and the pick-off annihilation takes place there. Physically, the wave function has no extension outside the infinite potential well. This implies to the following condition: the Ps wave function, $\psi(r)$, $= 0$ for $r \geq R+\Delta R$. Applying this condition to the first part of equation 2.22 with $\psi(r) = \sin(k_1(R+\Delta R)) = 0$ or $k_1(R+\Delta R) = \pi$, it reads:

$$\Psi(r) = A\frac{\sin\left(\dfrac{\pi r}{R+\Delta R}\right)}{r} \tag{2.23}$$

where the constant A can be evaluated from the normalization of the wave function.

The annihilation rate, λ, of Ps in a pore is the annihilation rate over the volume of the pore. Consequently, the overall annihilation rate is the annihilation rate inside the electronic layer of thickness ΔR, λ_a, and, if exists, the annihilation rate of Ps in the vacuum, $\lambda_{3\gamma}$. λ_a is the spin average annihilation rate of the pick-off annihilation in electronic layer ($\lambda_{2\gamma}$) and the vacuum annihilation rate ($\lambda_{3\gamma}$) [96] hence, $\lambda_a = 2$ ns $^{-12}$. So, if P is the probability of finding the Ps inside the well, therefore,

$$\lambda = \lambda_a P + \lambda_{3\gamma}(1-P) \tag{2.24}$$

Because the pore is small ($R < 1$), the vacuum Ps lifetime ($\lambda_{3\gamma} = 142$ ns) is ignored and the pick-off process is only considered. Therefore, the decay rate of the o-Ps inside a small pore (R < 1 nm) can be written as

$$\lambda = \lambda_a P \tag{2.25}$$

The probability of finding the Ps inside the electronic layer between R and $R+\Delta R$ is

$$P(R) = 1 - \left(\frac{\int\limits_0^R |\Psi(r)|^2 r^2\, dr}{\int\limits_0^{R+\Delta R} |\Psi(r)|^2 r^2\, dr}\right) \tag{2.26}$$

$^2\lambda_a = \frac{1}{4}\lambda_{2\gamma} + \frac{3}{4}\lambda_{3\gamma} = \frac{1}{4}(0.125)^{-1} + \frac{3}{4}(142)^{-1} = 2ns^{-1}$

By using equations 2.23 and equation 2.25, equation 2.26 yields

$$\lambda = 2 \left[1 - \frac{\int\limits_{0}^{R} \sin^2(\frac{\pi r}{(R + \Delta R)})\, dr}{\int\limits_{0}^{R+\Delta R} \sin^2(\frac{\pi r}{(R + \Delta R)})\, dr} \right] \tag{2.27}$$

After evaluating the integral in equation 2.27 (according to $\int sin^2(x) = \frac{1}{2}x - \frac{1}{4}sin(2x)$), we get

$$\lambda = 2 \left[1 - \frac{R}{R + \Delta R} + \frac{1}{2\pi} \sin\left(\frac{2\pi R}{R + \Delta R} \right) \right] \tag{2.28}$$

which is the well-known TE formula whereby the small pore sizes and free volumes can be deduced. This equation involves one free parameter, ΔR, which is not a universal value and it is material dependent, hence its definition is crucial for different classes of porous materials. The value of ΔR varies from 0.16 -0.17 nm [96, 97]. TE model is a temperature-independent model because the pore size is small and the excited energy states are very high. This represents a limitation of this model

2.8.2 Tao- Eldrup model for averaged pores

As stated before about TE model, it cannot determine the pore size of large pores (R > 1 nm) due to its simplifications and assumptions. One may think that to use TE model for large pores we need only to extend that model by introducing the annihilation of 3γ in the calculations and the Ps lifetime reaches 142 ns as R becomes large. A model has been constructed depending on this idea and it gave good results for even small pores although the small contribution of the 3γ annihilation [98]. Figure 2.13 represents the results of this model. This model is described by the following equation,

$$\lambda_{avg.} = 2[1 - \frac{R}{R + \Delta R} + \frac{1}{2\pi} \sin(\frac{2\pi R}{R + \Delta R})] + \frac{1}{140} \tag{2.29}$$

But as we can see from figure 2.13, by varying the $\lambda_{3\gamma}$, experimental data deviate from the overestimated correlated curve. The solution of this deviation was thought to be a modification of the potential and it was observed also that the assumption of one set of parameters cannot be used as a generalized set to fit well with the experimental data.
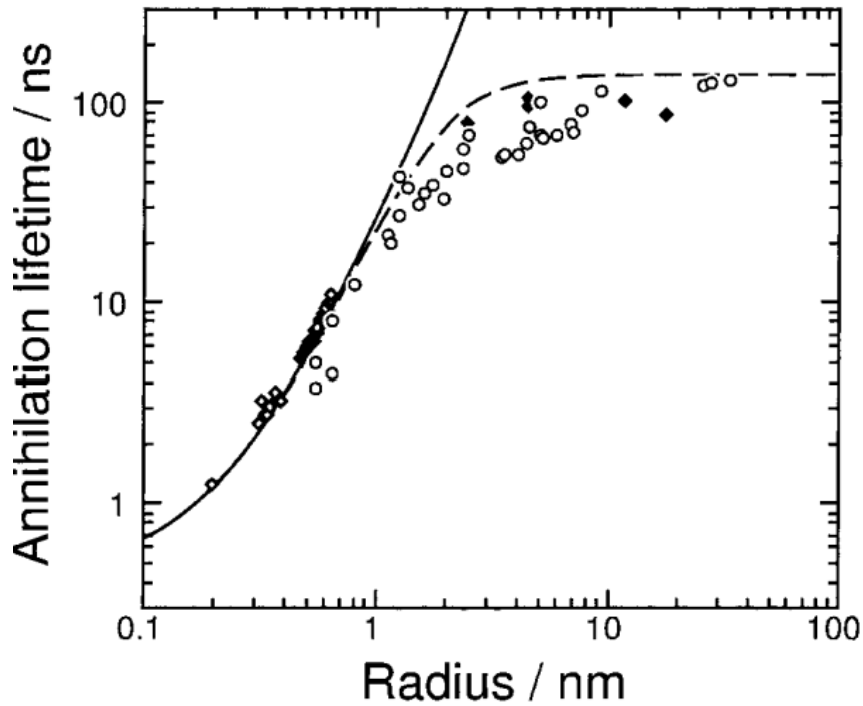
Figure 2.13: Annihilation lifetimes of o-Ps measured in various porous material as a function of average pore radius. The solid line is a correlation curve between o-Ps lifetime and a pore radius calculated from equation 2.28. The dashed line is calculated from equation 2.29 with a contribution from the o-Ps intrinsic annihilation [98].

2.8.3 Tokyo model for large pore

Tokyo model took into account the 3γ annihilation and the fact that for large pore the wave function of the Ps cannot be represented as a standing wave packet but it must be a Gaussian wave packet [98]. Also, it was proposed that Ps atoms occupy two regions inside large pores. A region of the pick-off annihilation near the pore walls of radius R_{Ps} and a second region at the center of the pore where the 3γ annihilation of Ps is predominant. Figure 2.14 shows an illustration of this model. Thus the total annihilation rate will be the sum of the annihilation rate of Ps inside these two regions i.e,

$$\psi = \begin{cases} \lambda_{TE}(R) + \lambda_{3\gamma} & for \quad R < R_a \\ \lambda_{TE}(R)(1-P) + \lambda_{3\gamma} & for \quad R \geqslant R_a \end{cases} \quad (2.30)$$

where P is the probability of finding the Ps inside a sphere of radius R- Ra which means the fraction of Ps free from interacting with the wall electrons. This probability can be given by considering that the Ps may be found in the region of radius R- Ra as a ratio from the all possible space available for it, R
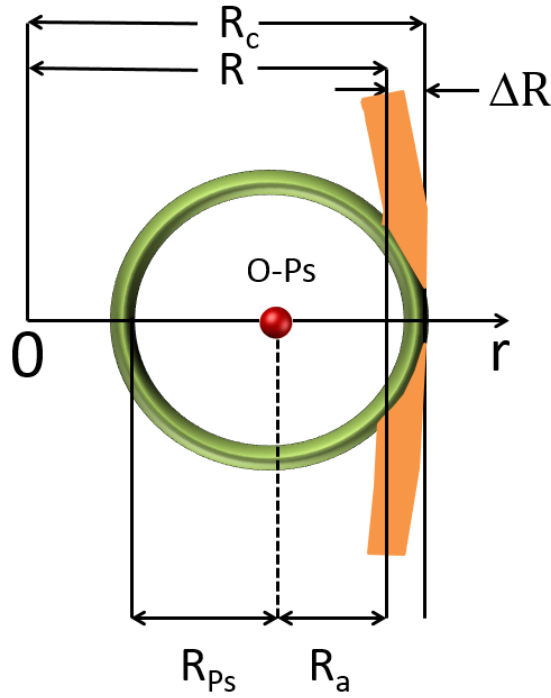
Figure 2.14: Schematic diagram of the Tokyo- model for Ps annihilation in large pores. R_{ps} represents a quantum radius of o-Ps [98].

$+ \Delta R$. This probability is given by an empirical parameter b;

$$P(R) = \left(\frac{R - R_a}{R + \Delta R}) \right)^b \tag{2.31}$$

It was found that R_a = 0.8 and b = 0.55. Figure 2.15 represents the experimental data for Ps in large pores which shows a perfect agreement between the experimental and the correlated data. However, it failed to predict the temperature dependence of the o-Ps also it is a semiempirical model, it means that this model depends strongly on the quality of the data used in the fitting [96]. These problems led researchers to try another model.

2.8.4   Extended TE (ETE) model

This model describes the behavior of the Ps in cylindrical and spherical pores by extending the TE model and solving higher orders of Bessel function [99–101]. The probability of the Ps accommodating any energy state is given by Boltzmann statistics. According to the ETE model, the total annihilation rate,
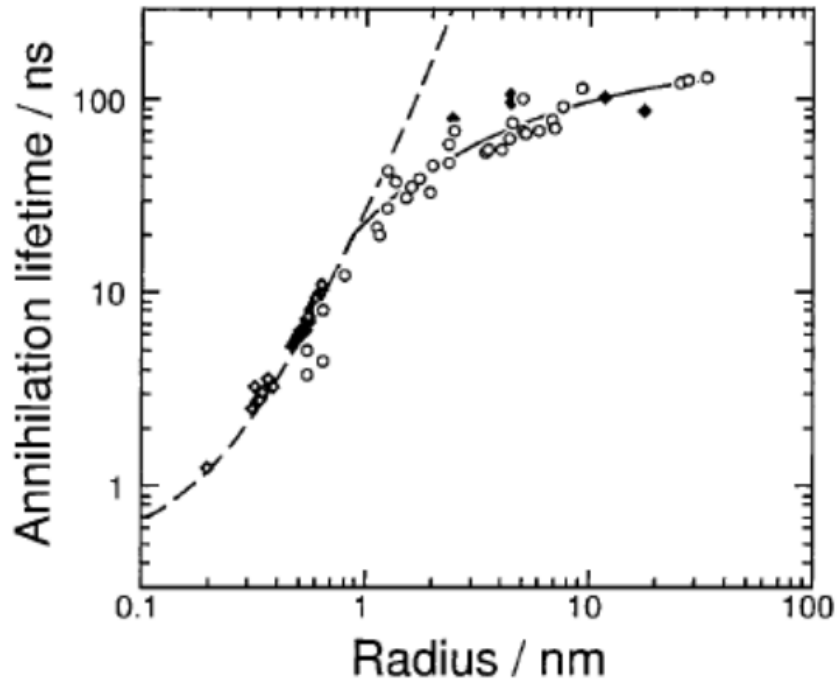
Figure 2.15: Annihilation lifetimes of the o-Ps measured in various porous materials as a function of average pore radius. The dashed line is a correlation curve calculated from equation 2.28. A solid line shows the correlation curve calculated from the extended equation, equation 2.30, where fitting parameters are determined as $b = 0.55$ and $R_a = 0.8$ with a correlation coefficient of 0.962, where ΔR is fixed at 0.166 nm [98].

λ, of Ps is given by

$$\lambda_{ETE}(d, T) = \lambda_a P + \lambda_T = \frac{\sum\limits_{i=1}^{N} \lambda_{ETE}^i g_i e^{-\frac{E_i(T)}{KT}}}{g_i e^{-\frac{E_i(T)}{KT}}} + \lambda_T \qquad (2.32)$$

where λ_{ETE}^i and E_i represent the annihilation rate and the energy state at the ith level. The factor g_i is used to describe the statistical weight of each state ($g_i = 2l+1$ for spherical geometry and $g_0 = 1$, $g_m \neq 0 = 2$ for cylindrical geometry). The annihilation rate for cylindrical pore symmetry (calculations for spherical geometry is presented in [102, 103])

$$\lambda_{ETE}^{nm} = \lambda_{2\gamma} \left(\frac{\int\limits_{\chi_{nm}R/R+\Delta}^{\chi_{nm}} J_m^2(r)r^2 dr}{\int\limits_{0}^{\chi_{nm}} J_m^2(r)r^2 dr} \right) \qquad (2.33)$$

where χ_{nm} is the nth nodes of the Bessel functions j_m and R is the pore size of a cylindrical pore. Δ is an empirical parameter related to the penetration of

Ps wave function into the bulk. This parameter is slightly dependent on the assumed pore geometry.

According to [96], the ETE model is not practically preferred. This is because the necessity of calculating the higher orders of Bessel function and their zeros means many terms should be included in the sum. For this reason, the Rectangular TE (RTE) model was proposed which offered an easier way to extend the TE model by switch the spherical pore geometry into a rectangular one.

2.8.5   Rectangular TE (RTE) model

The assumption of the rectangular shape of the pore came from the fact that the pore has no a specific shape and there is no constrains to choose a certain geometrical shape [96]. The success of this model appears if it fits well with the data of the pores of different sizes and at different temperatures. According to this model, the Ps was supposed to be confined to a rectangular potential well of sides a, b, and c along x, y and z directions respectively [96]. By using this potential well, the Schrödinger wave equation has the following solutions

$$\Psi_{ijk} = \Phi_i(x)\Phi_j(y)\Phi_k(z)$$

where;

$$\Phi_i(x) = \sqrt{\frac{2}{a}}\sin\left(\frac{i\pi x}{a}\right), \Phi_j(y) = \sqrt{\frac{2}{b}}\sin\left(\frac{i\pi y}{b}\right), \Phi_k(z) = \sqrt{\frac{2}{c}}\sin\left(\frac{i\pi z}{c}\right)$$

And the energy states populated in that potential well are,

$$E_{ijk} = \beta\left(\frac{i^2}{a^2} + \frac{j^2}{b^2} + \frac{k^2}{c^2}\right), \qquad \beta = \frac{\hbar^2}{16m} = 0.188\ eVnm^2$$

The Ps will annihilate by the 3γ emission when it will be in the center of the pore with the annihilation rate of $\lambda_{3\gamma}$. While once it lies in the electronic layer of thickness δ, it will annihilate by the 2γ emission via the pick-off process which is similar to TE model. For the three dimensional potential well, the annihilation rate may be written as [96]

$$\lambda(x,y,z) = \lambda_a - \begin{cases} \dfrac{\lambda_{2\gamma} - \lambda_{3\gamma}}{4} & for\ \delta \leqslant x \leqslant a - \delta, \delta \leqslant y \leqslant b - \delta, \delta \leqslant z \leqslant c - \delta \\ 0 & for\ other\ sizes \end{cases}$$

$$(2.34)$$

The annihilation rate can be determined statistically because in that model the Ps is assumed to be in thermal equilibrium with the pore and it can occupy all

possible states according to the Boltzmann distribution. Hence, the annihilation rate is

$$\lambda(a, b, c) = \sum_{i,j,k \neq 1}^{\infty} \rho_{ijk,ijk} \lambda_{ijk,ijk} \tag{2.35}$$

where $\rho_{ijk,ijk} = \dfrac{exp\left(-\frac{E_{ijk}}{KT}\right)}{\sum\limits_{i,j,k=1}^{\infty} exp\left(-\frac{E_{ijk}}{KT}\right)}$ is the density matrix which is non-zero and,

$\lambda_{ijk,ijk} = \lambda_a - \dfrac{\lambda_{2\gamma} - \lambda_{3\gamma}}{4} G_i(a,\delta) G_j(b,\delta) G_k(c,\delta)$ are the diagonal elements

of the annihilation rate matrix with $G_n(x,\delta) = 1 - \dfrac{2\delta}{x} + \dfrac{1}{n\pi} \sin\left(\dfrac{2n\pi\delta}{x}\right)$, so

equation 2.35 reads

$$\lambda_{ijk,ijk} = \lambda_a - \dfrac{\lambda_{2\gamma} - \lambda_{3\gamma}}{4} F(a,\delta,T) F(b,\delta,T) F(c,\delta,T) \tag{2.36}$$

where

$$F(x,\delta,T) = 1 - \dfrac{2\delta}{x} + \dfrac{\sum\limits_{i=1}^{\infty} \dfrac{1}{i\pi} \sin\left(\dfrac{2i\pi\delta}{x}\right) exp\left(-\dfrac{\beta i^2}{x^2 KT}\right)}{\sum\limits_{i=1}^{\infty} exp\left(-\dfrac{\beta i^2}{x^2 KT}\right)}$$

Equation 2.36 is the RTE model. In this model, there is only one free parameter, δ, which is similar to ΔR in TE model. Here, the Ps atom is assumed to be interacting with pores of radii extended to the hard walls of the pore. This means that the radius of the pore, in the definitions of TE model, will be $R + \Delta R$ not only R. To correlate the RTE model to the TE model, the mean free paths of a cube of side width a and a sphere of radius $R + \Delta R$ were equated which gave $a = 2(R + \Delta R)$.

To determine the value of δ, a has to be replaced with $2(R + \Delta R)$ and let T = 0 K, varying the value of δ to get a close agreement with TE results. With this procedure, it was found that the value of δ is 0.18 nm [96] compared with ΔR = 0.166 nm for TE model. A challenge of this model is the confirmation of the relatively weak dependence between the pore geometry and the o-Ps lifetime. To illustrate this, authors of [96] calculated the o-Ps lifetime for different geometrical shapes of 1D sheets, 2D square channels, and 3D cubes as functions of the mean free path, l, where $l_{1D} = 2a$, $l_{2D} = a$, and $l_{3D} = \left(\dfrac{2}{3}\right) a$. In figure 2.16, there is a perfect agreement with the lifetimes at large mean free path regardless the pore shape of the large pore. This is understood due to the fact that
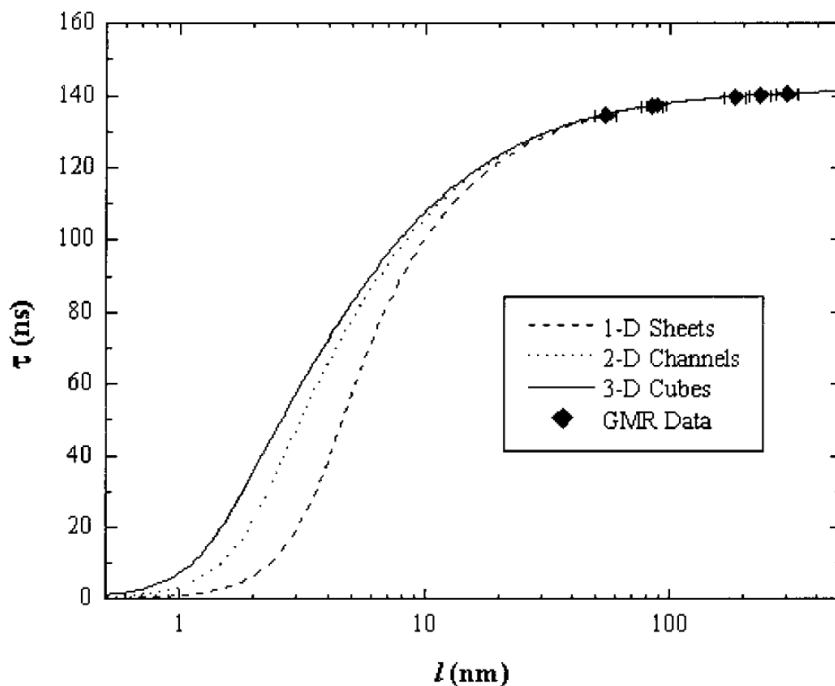
Figure 2.16: RTE model correlating the o-Ps lifetime to the mean free path, l, for three pore geometries [96].

the Ps mean free path between wall collisions is different for each of the three dimensionalities considered.

As a final examination of the RTE model, the temperature dependence must be evaluated. Figure 2.17 shows RTE model at different temperatures. From the figure, we can see that, as stated before, at T= 0 K, there is a perfect agreement between the TE and the RTE models in the sub- nanometer regime with a modification of the TE model to include the o-Ps lifetime of 142 ns. Since it correlates the Ps lifetime with small and large pore sizes well and it can be used for different pore geometries and at different temperatures, the RTE model is widely used and accepted with reliable results for porosimetry. It has only a drawback at low temperatures where it overestimates [104] or underestimates [85] the pore sizes. Worth mentioning, the ETE model does also.

2.9   Slow positron (SLOPOS) beam

In addition to the bulk probing of samples by the conventional positron sources, SLOPOS offers the ability to investigate thin layers and surfaces. SLOPOS has this feature via the production of mono-energetic low-energy positrons [105] which, thereafter, can be accelerated to the required energy (and penetration depth). Typical acceleration energy ranges from ∽ eV to several keV. The num-
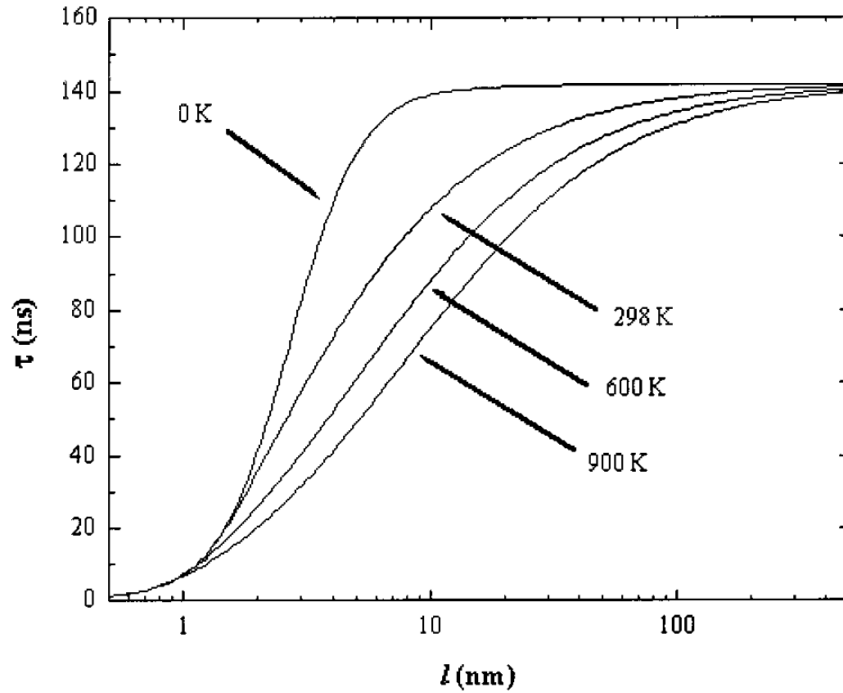
Figure 2.17: Temperature dependence of the Ps lifetime for cubical pores according to the RTE model. The mean free path, l, is related to the cube side length by $l = \left(\dfrac{2}{3}\right) a$ [96].

ber of slow positrons divided by the fast incident positrons is the moderation efficiency, ε [106]. ε represents a practical challenge because only a small fraction of the incident positrons slowed down. Positrons come out from the moderation are fluxes of fast and slow positrons and since only the slow positrons are needed, so a separation of the slow positrons from that flux is important. This separation can be established by using a slow positron beam guidance system.

2.9.1 Positron production and moderation

The energy spectrum of emitted positrons from ^{22}Na before and after the moderation [72] is shown in figure 2.18. It is clearly seen that positron energy without moderation is a continuum while that of the moderated positrons peaked at narrow (single) energy value equals to 3 eV in case of tungsten as a moderator. When high energy positrons are injected into a sample, they will undergo inelastic collisions and they will lose their energy to reach thermal equilibrium with their surroundings. The diffusion length, L_+, is defined as the average distance traveled by thermalized positrons before annihilation. In case of a (110) tungsten foil, it was found that about 13 % of the incidence positrons will annihilate inside the sample (figure 2.19) and the remaining thermalized positrons will reach the surface of tungsten and undergo one of the following processes;
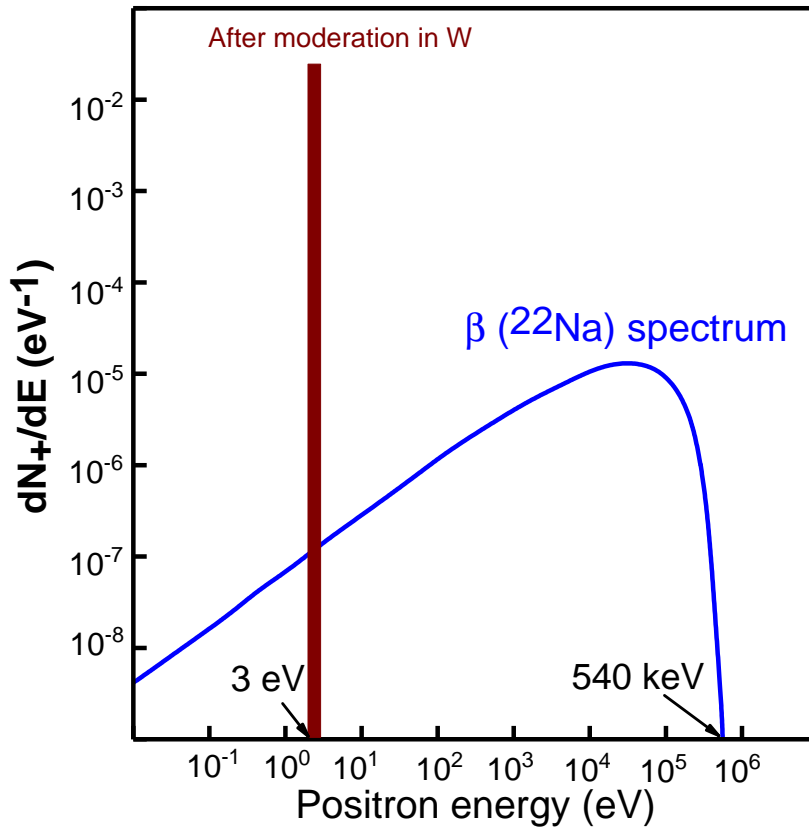
Figure 2.18: Spectrum of positron emission from a ^{22}Na source. $\dfrac{dN}{dE}$ is the number of positrons per energy channel E. The narrow curve positioned at 3 eV shows the energy distribution after moderation in tungsten [72].

- leave as a fast positron (87 % in figure 2.19)

- free positrons leave into the vacuum with a kinetic energy equals to the work function of the sample (moderator in this case) (0.05 % in figure 2.19)

The idea behind the emission of slow positrons from the surface is the moderator's negative work function [72, 81]. The moderation process of positrons in tungsten foil is shown in figure 2.19. The ratio of slow emitted positrons will increase by increasing the moderator's negative work function [106]. Tungsten is a widely used moderator with $\varepsilon_W \sim 3.2\pm0.4 \times 10^{-4}$ and -3 eV work function (in the 110 orientation [106]). Well annealed tungsten had $\varepsilon < 0.7 \times 10^{-3}$ [107]. ε was measured for solid Ne and it was 0.7×10^{-2} [81, 108] using cylindrical geometry. Moderators should allow slow positrons to reach the surface efficiently so, their surface transmission probability is important. This transmission probability depends on the effective diffusion length [81] and the highest moderation efficiency was obtained from rare gases condensed directly on the radioactive capsule owing to the long L_+ (incomplete thermalization).
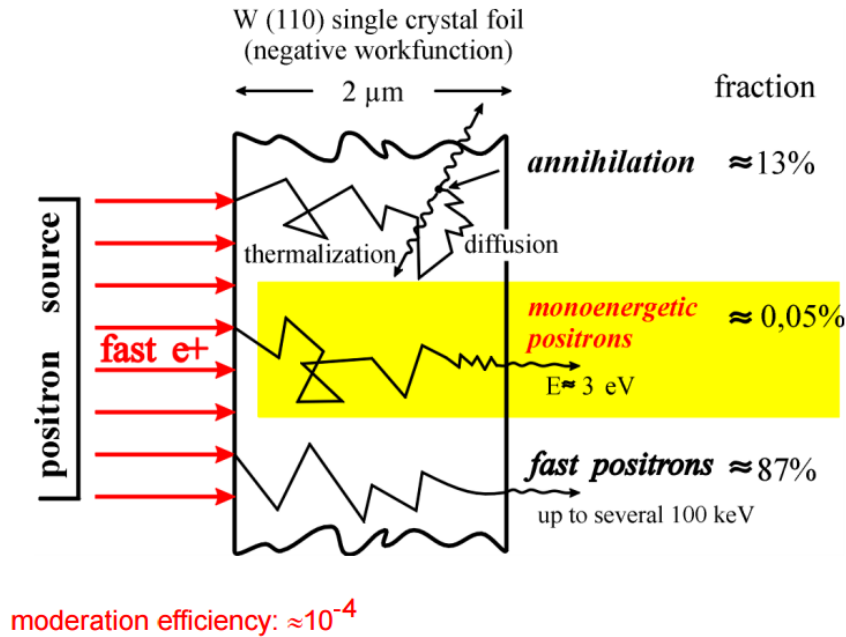
Figure 2.19: Positron moderation process in transmission geometry by a (110) tungsten foil. A small fraction stops in the foil and annihilates there. Another very small fraction may spontaneously release upon reaching the surface due to the negative work function of W. The majority of positrons leave the moderator foil with a high energy [72].

Alternatively, as a field assistant moderator, SiC may be used [109]. The low moderation efficiency requires a strong positron source which means an intensive radiation protection must be performed.

2.9.2 Beam transport and acceleration

Positrons come out from the moderators are a mixture of slow and fast positrons these positrons should be separated before they can be utilized in experiments. Slow positrons can be transported from the moderator to the target by magnetic, electrostatic, or a mixture of both [110] through reflectors, filters, apertures, accelerators, and lenses [81]. For magnetic guidance, it can be performed by the use of an $\mathbf{E} \times \mathbf{B}$ filter, or by using an external magnetic field perpendicular to the beam direction. A bent solenoid is an additional method for the beam guidance [72] (and references therein). The system used at Martin Luther University is a bent solenoid system as shown in figure 2.20 and it is dedicated to surfaces studies and thin layers by Doppler broadening technique. As indicated in figure 2.20, the source- moderator is placed in front of the bent tube which works as a filter to stop the fast positrons. Slow positrons are guided into the system axis and it can be accelerated by the use of a linear accelerator which accelerates the positrons by high voltage (supply the positron of energy till several keVs). Afterwards, positrons are obligated to move in a helical path of a longitudinal
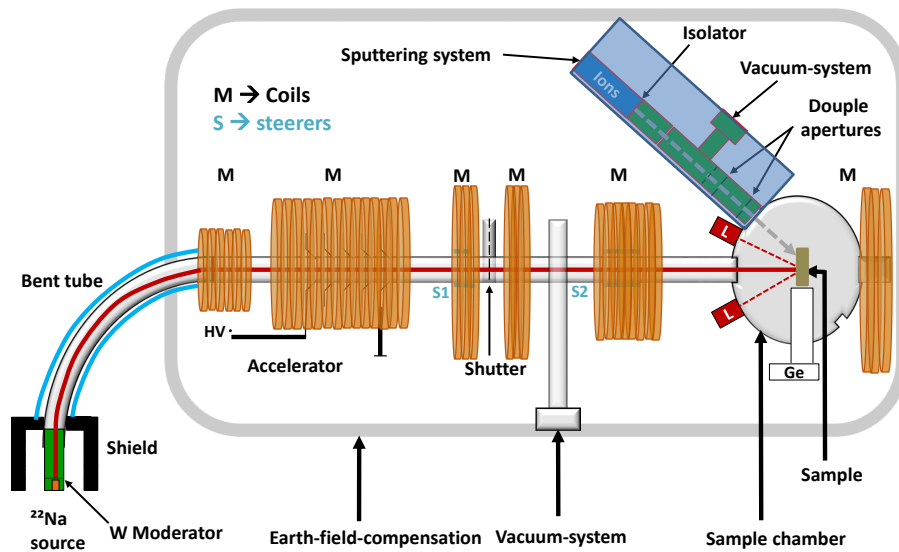
Figure 2.20: The slow-positron-beam system POSSY at Martin Luther University Halle– Wittenberg. Moderated positrons are fed through the collimator by the solenoids and are accelerated to the sample. The whole longitudinal magnetic field is generated by the guidance coils (M) (modified from [112]).

magnetic field generated by a system of coils [111]. Two steerers should be used to direct the positron beam to the sample. An additional part (sputtering system in figure 2.20) was designed principally to perform sputtering experiment which aims to enhance the depth resolution of positron distribution in samples [112]. The concrete sample position should be known precisely to guide the positrons there so a calibration must be done. To perform such a calibration, the current values for X-Y deflection of the steerers should be determined from the count rate contour plot. By varying the current of the coils, the scan can be performed. Measurement for 5 seconds for each point during the scan gives a clear picture, from which one can determine the position of the sample [111].

2.9.3   Measurement

The POSSY system cannot be used for lifetime measurement because of the missed start signal (pulsed positron beam can supply it) and it is used principally for DBS measurement. The Ge detector is placed in the vicinity of the sample outside the sample chamber and out of the vacuum. From DBS, one can measure both S and W parameters to identify defects in samples. As a main function of the slow positron beam, the depth profiling can be evaluated and both S and W parameters are measured as functions of positron energy (depth)

in the sample.

2.10 Pulsed slow positron beam

In case of surface, near surface, thin layers, and depth profiled studies, the slow positron should be used. One of the main challenges of constructing a positron beam for positron lifetime measurements is the realization of the start signal. Pulsed or bunched slow positron beam is used to carry out PALS measurement because it supplies the start signal for the lifetime measurement. Rather than ^{22}Na source for positron production, a high energetic electron beam from a linear accelerator (LINAC) can interact with a converter producing high energetic photons via the Bremsstrahlung [113] process. These energetic photons will be converted into electron-positron pairs by pair production process. The positron yield (which depends strongly on the incident electron beam energy and possess a mean energy of about $\frac{1}{5}$ of the electron beam energy for $E_{e^-} >$100 MeV) is moderated in tungsten and it is extracted to the beamline while the produced electron is separated from the slow positron beam. It was found that the moderation efficiency decreases at high electron energies also, the positron yield is saturated at about 60 MeV of the incident electron beam, therefore, it is recommended to use an electron beam energy in the 40-60 MeV range [114]. The Electron Linear accelerator with high Brilliance and low Emittance (ELBE) system at Helmholtz Zentrum in Dresden-Rossendorf (HZDR) is a pulsed electron beam and it is constructed based on the aforementioned physical meanings and quantities. ELBE is a superconducting linear accelerator working in the continuous wave mode of the electron beam with adjustable frequency (26MHz divided by 2^n) [115] and it has unique beam structure and intensity for performing PALS measurements. Currently, the electron beam energy of the ELBE facility is about 30 MeV with an average current of up to 0.1 mA [116]. The EPOS (ELBE Positron Source) project is a collaborative effort between HZDR and the Martin-Luther-University Halle-Wittenberg. EPOS consists of several parts [78]

- **Mono-energetic Positron Source (MePS)**$\longrightarrow$ a pulsed slow positron beam with high intensity for depth profiling measurements. Both PALS and DBS are available. Information depth: 0-5μm

- **Conventional Positron Source (CoPS)** $\longrightarrow$ consists of two parts, one of them is a continuous positron beam for Coincidence DBS (CDBS) with a high energy resolution and the second part is the DPALS from ^{22}Na. Information depth: 10-200μm

- **Gamma-induced Positron Annihilation Spectroscopy (GiPS)**$\longrightarrow$ Pulsed bremsstrahlung is used for positron spectroscopy of bulk samples, liquids, etc. Information depth: 0.1 mm-2 cm

In the presence of these techniques, the use of most essential PAS techniques, like PALS, (C) DBS and AMOC, is available.

2.10.1 Mono-energetic Positron Source (MePS)

MePS is a high-intensity and bunched beam using mono-energetic positrons for positrons and Ps studies. The intensity increased by a factor of 20 after the replacement of Pt foil by 10 tungsten meshes [117]. According to [117], very short electron bunches in a time interval less than 5 ps hit the electron-positron converter in the presence of continuous wave mode with a frequency of 26 MHz divided by 2^n (with n=0,1,2,...). For short positron lifetime, a repetition frequency can be set to be 77 ns and it can be adjusted to be 616 ns for long time measurements (for porosimetry) which needs a high bunch charge in order to maintain the intensity. The ability to change the repetition frequency to measure small and long lifetimes with the change of the bunch charge to get rid of the intensity degradation is an advantage of the Linac-based beam over the reactor-based beam. A schematic representation of MePS system is shown in Figure 2.21. The converter (W) is a package of 50 W foils (0.1 mm each) and it is water cooled directly. After the electron beam hits the converter, positron-electron pairs are produced. The produced electrons can be stopped at the beam dump which made from 5N-Al. The moderator is placed in the front of the converter and parallel to the direction of the motion of the moderated positrons which can be extracted by the use of an Einzel lens. The positron bunch can be directed into the magnetic field by the lens and it is transported to the beamline with an optimized driving energy of 2 keV applied at the grids of the lens. Energies lower than 2keV will result in a larger time spread at the buncher and hence a bad resolution and energies higher than 2keV imply to increase the buncher voltage which is limited and reached its maximum at 2keV. Steering coils pairs are used for the adjustment of the beam inside the beamline at any place. The moderated positrons in the first cave (111b) are fed to the second cave (111d) through a cable tunnel which lies at the bottom of a 3.2 m shield of concrete. Straight beam transportation implies to a very high radiation dose in the measurement cave due to the high intensity of the produced radiations in the converter. The time broadening of the positron beam reaching the positron lab 6 m away from the site of positron production is about 10 ns which arises from the moderation process, inhomogeneity in the acceleration
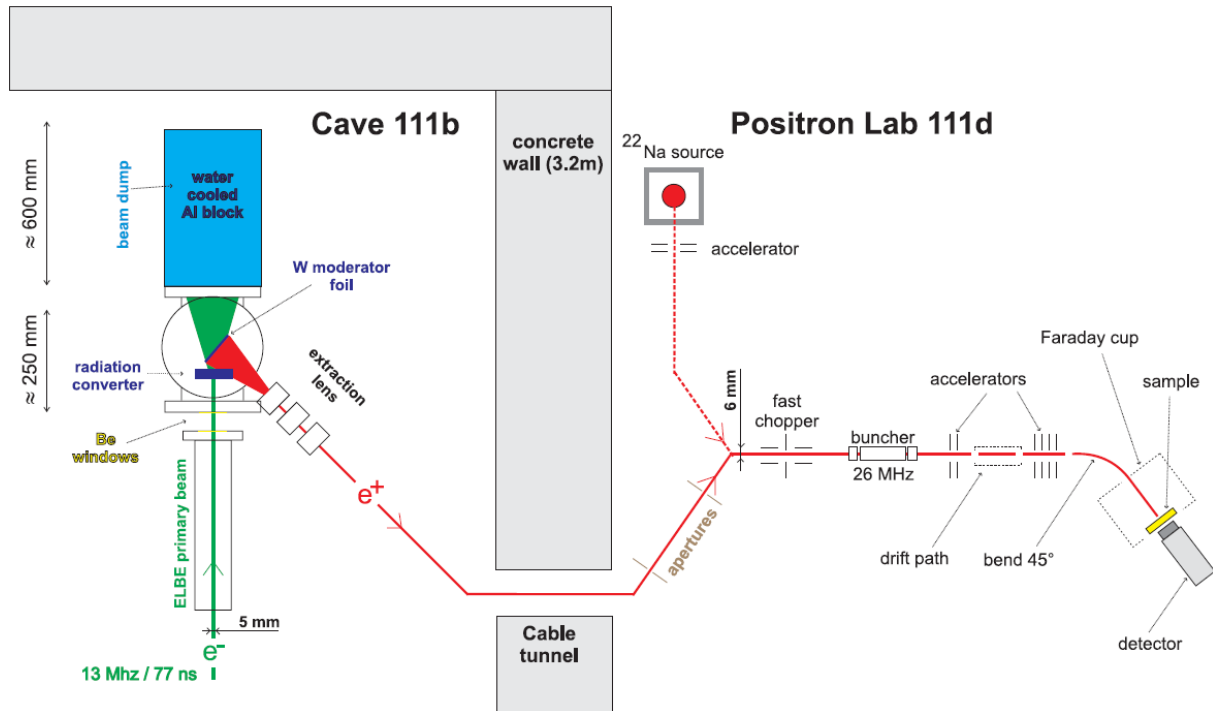
Figure 2.21: Illustration of the Mono-energetic Positron System (MePS) of the ELBE facility at HZDR. The place of positron production (Cave 111b) and the positron lab (Cave 111d) are separated by a 3.2 m concrete wall. The beam length is about 12 m. The ^{22}Na source is a future extension of the system to allow experimental work when the electron beam is not available [117].

field, and finally from the three paths of the beamline. This broadening can be overcome by the use of a combination of chopper and double slit buncher. Also, any backscattered positrons can be prevented from reaching the detector by the application of a bent with 45°. The PMT is placed outside the vacuum and close to the sample. The timing process of the pulsed slow positron beam and the functions of both chopper and buncher are discussed in the next section.

2.10.1.1 Chopper and buncher

Simply, the lifetime measurement using the pulsed slow positron beam can be understood from figure 2.22. Due to the moderation process and the beam transportation, the coming slow positron beam has a large time spread which means a very bad time resolution and bad time focusing. The main task of the pulsed beam is to detect the start signal precisely of a narrow positron pulse which should arrive the target at a definite moment with a definite energy. This can be done by using a combination of chopper and buncher.

Chopper: Chopper is a simple device and consists of two capacitors with different polarities used to suppress the background by allowing the beam to pass
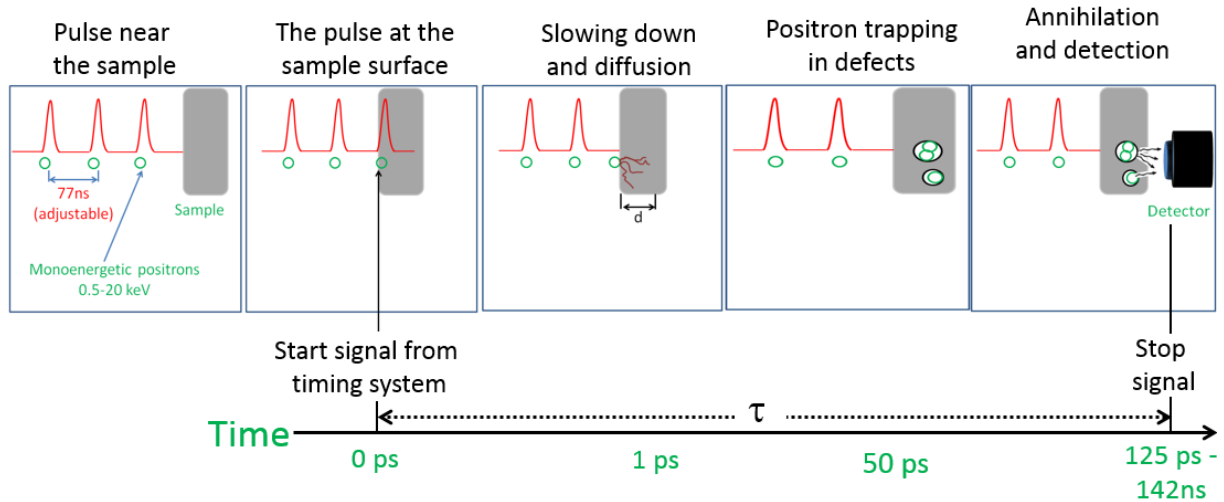
Figure 2.22: Idea of the timing system of the pulsed slow positron beams (modified from [118]).

through at a certain time window and preventing it at any other time. The reduction of the chopper time window is important for effective work of the buncher. Graphically, one stage of the two-stage deflected chopper working with an electric field only is represented in figure 2.23. As it can be seen there, a DC voltage is applied to the upper plate and a DC + a square Radio Frequency (RF) wave are applied to the lower plate. At first, when the amplitude of the RF wave is zero (no beam), any coming positrons are background and they will be deflected towards plate A (the blue line in figure 2.23). While in the presence of the beam pulse, the RF amplitude is being increased in such a way that the voltage in plate A, V_A, is compensated by the voltage in plate B, V_B, and the applied RF pulse. Hence, the beam will move unhindered through the slit (the green line in figure 2.23). Any positrons come during the RF but with insufficient amplitudes for doing the voltage compensation will not pass the slit but will hit the red metal plate and stop there (dotted black lines in figure 2.23). The output signal from the chopper has 5 ns full width at half maximum allowing an efficient buncher operation. It should be noticed here that the RF wave of the chopper should be synchronized with the coming beam which has 1.625 MHZ and 615 ns time spacing between pulses. In the first stage of the chopper, the beam has some transversal energy distortions which can be minimized by using a second stage which has the same working principle of the first stage but with different plates polarities. The incorporation of the second chopper stage does not affect the intensity too much.

In case of the presence of magnetic field B, the moving positrons, which have a perpendicular velocity to the motion direction (because of E), will have a gyration motion of radius r_g. The gyration radius depends on E and B which means that in addition to the dependence on the width of the slit, the RF amplitude,
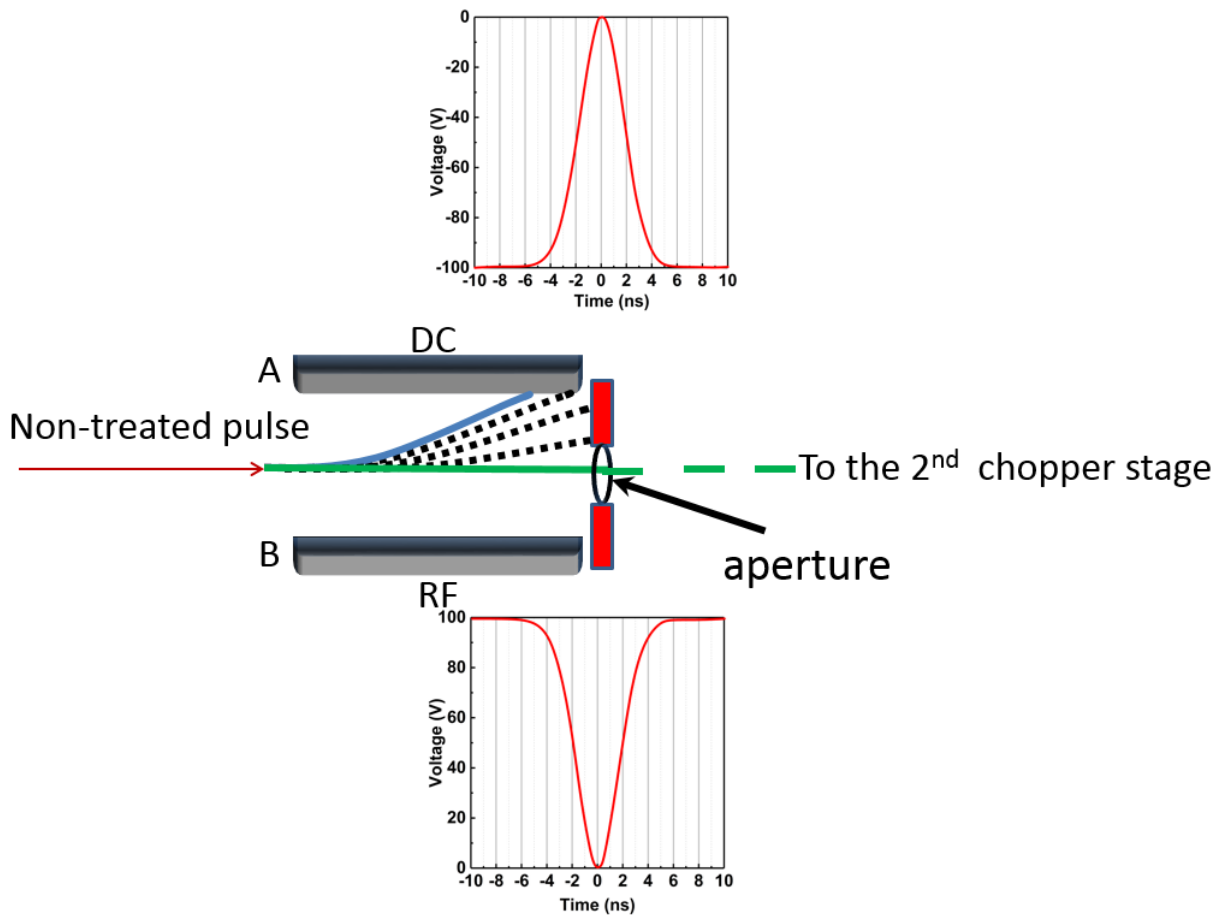
Figure 2.23: Working principle of a single stage of a deflection chopper in the presence of electric field only.

and the applied deflection potential, the time width of the resultant chopper pulse will depend on the magnetic field as well.

Buncher: To estimate the timing process properly, the slow positron beam should arrive at the sample surface at a definite time. Due to the moderation process and the beam transportation, the slow positron beam is not time aligned and it has a time spread, Δt, which should be minimized as possible. Such a time compression process can be understood as follows: Suppose that there are three particles traveling in the same direction at different speeds from point A to B in such a way that the faster particle is up to reach point B and the slowest one is located at point A and the third particle in the middle between A and B. If the middle particle is considered as a reference particle, it is possible to evaluate how much the deceleration/acceleration of the faster/slower particle is to be, after a certain time, at the same place of the middle particle. The same way, buncher is a velocity modulating device by accelerating too late particles and decelerate too early ones and its output is a time focused pulse with a very small time spread or width. This idea is depicted in figure 2.24 for a beam with
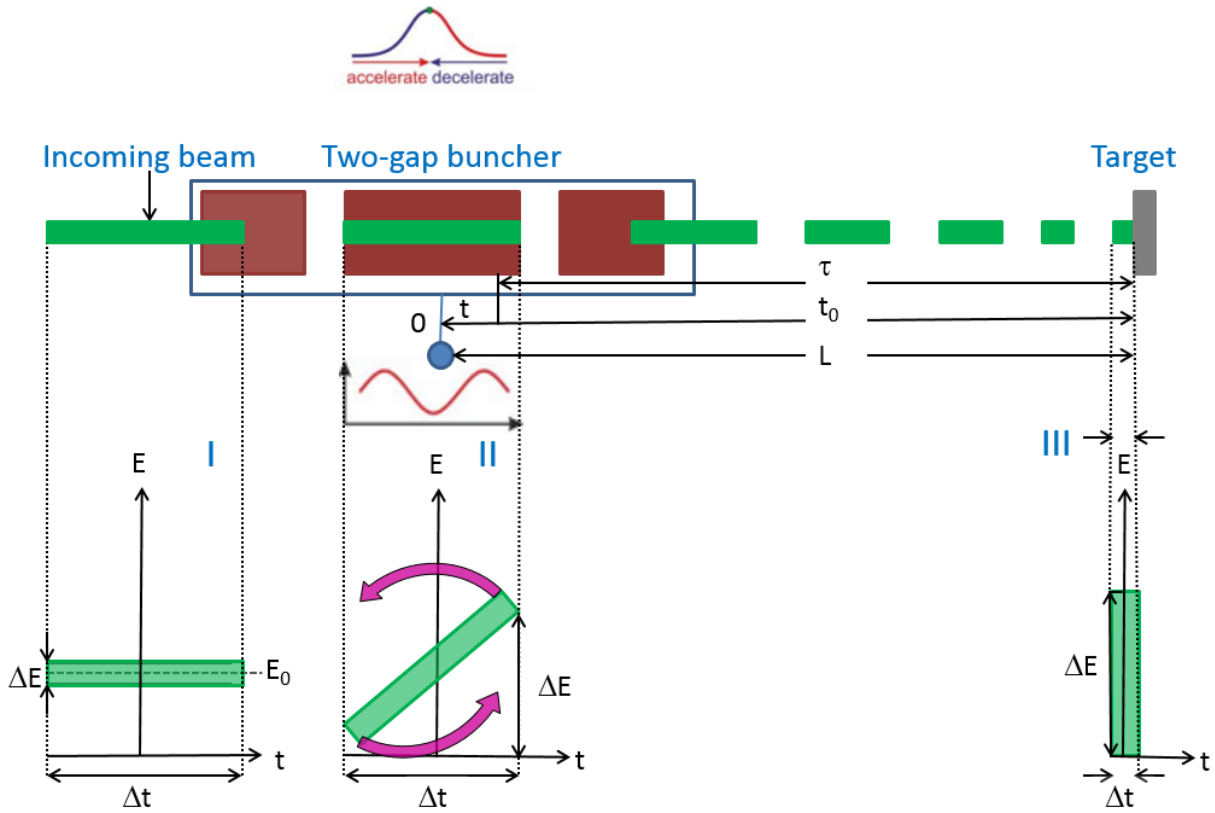
Figure 2.24: Schematic representation of the buncher working principle (modified from [117]).

initial energy E_0 and initial velocity v_0 where it is clear that the original beam has a large time spread with a relatively small energy spread, ΔE, (region I). Now the goal is to bunch the beam in order to allow all positron to reach the sample surface at the same time (region III).

Due to the conservation of the area covered by the beam, the time spread can be modulated at the sample surface to be minimum with a large energy spread. Such a modulation in ΔE (and hence Δt) can be done as follows: Suppose that t_0 is the time taken by an unmodulated reference particle to travel from the center of the buncher to the target (L). If another particle comes at the buncher gap after a time t, its time to reach the target is

$$t + \tau(t) = t_0 \tag{2.37}$$

here $\tau(t)$ is the time taken by a modulated particle to hit the target which can be expressed as

$$\tau(t) = \frac{L}{v(t)} \tag{2.38}$$

where $v(t)$ is the modulated velocity by the applied modulated voltage $V(t)$. The non-relativistic modulated velocity $v(t)$ would be $\sqrt{\dfrac{2(E_0 + eV(t))}{m}}$, where

m is the mass of positron and e is the electronic charge. Equation 2.38 reads

$$\tau(t) = L\sqrt{\frac{m}{2(E_0 + eV(t))}} \tag{2.39}$$

and equation 2.37 becomes

$$t + L\sqrt{\frac{m}{2(E_0 + eV(t))}} = t_0 \Rightarrow eV(t) = \frac{mL^2}{2t_0}\frac{1}{\left(1 - \dfrac{t}{t_0}\right)^2} - E_0 \tag{2.40}$$

with $E_0 = \dfrac{1}{2}mv_0^2$ and $v_0^2 = \dfrac{L^2}{t_0^2}$, equation 2.40 yields

$$V(t) = \frac{E_0}{e}\left(\frac{1}{\left(1 - \dfrac{t}{t_0}\right)^2} - 1\right) \tag{2.41}$$

Equation 2.41 represents the ideal form of the modulation voltage but unfortunately, it is a parabolic voltage and it is difficult to be carried out at high repetition frequencies. This problem can be overcome by applying a sin wave voltage. In equation 2.41, the bunch flight time, (t), $\ll t_0$, so we have $\left(\dfrac{t}{t_0}\right)^2 \simeq 0$ and

$$V(t) = \frac{E_0}{e}\left(\frac{1}{\left(1 - \dfrac{2t}{t_0}\right)} - 1\right) \xrightarrow{\text{binomial}} \frac{2E_0}{t_0 e}t \tag{2.42}$$

Equation 2.42 is the optimum applied modulating voltage with a sawtooth waveform but such a wave produces a small amplitude which results in a beam broadening and a bad time resolution. For further approximation and applicability, this sawtooth wave can be approximated by the linear part of a sinus function of amplitude V_0 and angular frequency, ω, around the zero crossing. For small angle ωt, we have $\sin(\omega t) \approx \omega t$ then

$$V(t) = V_0\sin(\omega t) \approx V_0\omega t \tag{2.43}$$

Since the left-hand sides of equations 2.42 and 2.43 are equal so we obtained

$$V(t) = \frac{2E_0}{e\omega t_0} = \frac{2E_0}{e\omega}\frac{1}{L}\sqrt{\frac{2E_0}{m}} \Rightarrow \boxed{V(t) = \frac{1}{e\omega L}\sqrt{\frac{8E_0^3}{m}}} \tag{2.44}$$

$V(t)$ in equation 2.44 is the modulating voltage and it is applied to the central electrode of buncher and the modulation is performed in both gaps. In addition to the modulating voltage, the length of the central electrode is crucial as well.

2.11   Survey of PALS in the field of porosimetry

PALS has some unique features which enabled it to be a strong competitor for the conventional tools of porosimetry. It is a non-destructive technique and, uniquely, can be used for in-situ measurements (different pressures, different temperatures) [119]. It can detect closed and open porous structure [120, 121]. Additionally, PALS measurements would reflect the PSD [82, 119], pore interconnectivity [82, 122, 123], pore filling [124–127], and it can give some indications about any changes in the electron density of the inner porous surfaces [128–130].

To mention some examples of previous work done by researchers, Zaleski at al. [119] performed an in situ measurement of PALS during the adsorption and desorption of n-heptane molecules in the mesoporous Amberlite XAD4 polymer. In this study, the n-heptane was chosen because it resembles a significant content of volatile organic compounds whose separation from air pollution is of an environment and economic importance. PALS results showed that the total pore volume decreases with the pressure of n-heptane and it becomes zero at the saturated pressure while the average pore size increases linearly. These result would mean that the polymer microspheres are swelling with adsorption due to penetration of the alkane inside them.

PALS was used by the group of Gidley [131] to get a deeper understanding of the adsorption mechanisms and the thermal stability, for the first time, of MOF-5. Two o-Ps lifetime components were obtained for this sample of 13 ns (85% of the formed Ps) corresponding to 1.5 nm (cubes) and 86 ns (15 % of the formed Ps) corresponding to 6 nm (defects). Neither gas sorption nor x-ray diffraction detected these defects in MOF which means a uniqueness of PALS to study MOFs. A temperature dependent measurement revealed that the 13 ns component was due to a free movement of o-Ps in the vacant framework sampling many thousands of cages (calculated from the diffusion length by a slow positron beam). This means after a complete adsorption of gases in the sample, the 13 ns would disappear. Surprisingly, in situ measurements of PALS during CO_2 indicated that the 13 ns became 4 ns, not zero meaning that there were still unfilled pores having 0.8 nm even at 400 psi of CO_2. This result showed that efforts should be exerted to exploit this remaining space in MOFs to increase their gas uptake. To test the thermal stability of the framework, the sample was heated for different times at 693 K, 173 K, and 733 K. It was found that an additional component of 7 ns is obtained at the cost of the 13 ns after heating the sample at 693 K for 3 h. This was explained as a framework collapse. This study provided a picture of the onset of the framework degradation due to heat-

ing the sample at temperatures higher than 673 K.

In [121], Wang et al. conducted a depth profiling measurement of two low-k (spin-coated methyl-silsesquioxane (MSSQ) and CVD SiCOH (or carbon-doped oxide, CDO)) films with different porogen loads by a slow positron beam. This study aimed to study the effect of the porogen chemistry and film capping on the nanoporous structure of the investigated films. Results of this study showed that using a porogen containing C, N, H, and O caused a threshold of 10 % load for forming open (interconnected) porosity in comparison with a 20 % load of another porogen having C, H, and O only. This means that the porogen of the 10 % threshold has a lower degree of penetration into the material matrix and it is removed faster after curing the sample which signifies the importance of the porogen chemistry. Closed pores are required in low-k materials to increase their mechanical stability and to prevent the adsorping of undesired substances (which will affect the k value of the films), this study showed that the capped CVD films have open and closed pores. The existence of open pores (tested by measuring their intensity with and without shielding the detector) would mean either a surface roughness which left some spaces on the surface open or the cap is polycrystalline having some holes.

Zaleski used his model described in [119] for converting the lifetime distribution given from MELT into PSD to compare the PSD derived from the low-temperature N_2 sorption and from PALS of polymer-silica composite [129]. The organic-inorganic composites (used in gas separation, catalysis, chemical sensing, and drug delivery) have different routes of synthesis. The aim of this study was to get a correlation between the structural parameters of the composites (synthesized by an alternative route [132]) from PALS and N_2 sorption measurements. This synthesis route depends on the swelling of preformed polymer particles in TEOS and condensation of the silica precursor. PALS results confirmed the swelling of the polymer due to silica precursor penetration within the polymer. The mesopores of the initial sample become smaller and uniform after condensation while micropores in the polymer matrix become slightly larger. Pores having pore size > 2 nm disappeared after calcination. Despite the reasonable correlation between PALS results and sorption ones of accessible pores, PALS showed that there are closed pores in the investigated samples. It was found that the best correlation between PALS and sorption results was obtained by using the BJH model for getting the PSD from the sorption data.

Another attempt was done by our group [133] to correlate the pore volume calculated form N_2 adsorption to the integration of the peak area of o-Ps signals obtained from MELT analyses of PALS data. The studying system was a bimodal system of 15 nm pores of silica gel and 4 nm pores of MCM-41

produced by pseudomorphic transformation process. In this method, the main concern was not to calculate the PSD from PALS data. After normalizing the peak area of the MCM-41 pores to unity, by assuming a constant pore volume after the transformation, the correlation between the peak area of PALS signal and the pore volume of MCM-41 pores exhibited a good fit except for 10 mlg^{-1} of CTAOH (as the peak area was nearly zero despite detecting about 0.13 gcm^{-3} pore volume). They ascribed this deviation at 10 mlg^{-1} of CTAOH to the disability of forming MCM-41 pores because the surfactant which are responsible for forming MCM-41 pores could not be removed via calcination as they were contained in closed volumes. However, the authors did not take into account the possibility of o-Ps migration from the accessible MCM-41 pores to silica gel pores which would reduce the intensity in the MCM-41 pores and reduce the detected pore size of MCM-41. This migration could be responsible for the deviation at 10 mlg^{-1} of CTAOH (especially, if one considers N_2 results , the detected signal at $\sim$ 25 ns, and the very high intensity of the silica gel pore given by PALS (and at 25 mlg^{-1})). Additionaly, this escape could explain the overstimation of PALS data for the starting pores of silica gel. This conclusion can be driven in the light of the discussions presented in [134].

The adsorption-desorption behavior of water in SBA-3 has been studied by using PALS measurements by Maheshwari et al. [135]. The aim of this study was to formulate a clear picture about the kinetics of adsorption-desorption and transport of water in porous materials. The water was selected because it was found that confined water in porous silica, alumina, and zeolites has a great relevance for pharmaceutical applications. It was concluded that at low pressures of adsorption water forms small numbers isles around silanol groups. The number of the formed isles was increased (reflected in the decreased length of the cylindrical SBA-3 pores and the reduction in the o-Ps escape probability) with increasing the pressure. These isles continued to form plugs and condensation starts at relative pressures > 0.3 which was able to host o-Ps bubbles. The formation of these plugs is not a continuous function with the pressure while the size of cavities between plugs was getting smaller. The desorption showed a reversible behavior of the adsorption but some water was confined in the micropores at low pressure and their removal requires heating the sample under vacuum.

Kullmann et al. [136] used PALS to study the filling of CPG samples having different pore sizes with Paracetamol. This study is important because polymorphous medicaments exhibit different crystallization once confined in a porous system. Understanding this property would help for controlling the crystalline state and optimizing the use of the medicament. PALS is considered as a power-

ful technique in such studies because closed pores can be easily formed during the filling. Investigating sample with 22 nm pores by PALS showed that loading the sample with Paracetamol resulted in ~ 92 % pore filling where the filled sample gave τ_4 =111 ns with 0.5 % intensity in comparison with τ_4 =121 ns with 6.2 % intensity in the unloaded sample. The 0.5 % intensity of the 111 ns lifetime is attributed to the formation of closed pores due to the filling process. Similarly, another sample with 9.3 nm pores showed ~ 88 % pore filling which means partially filled pores. Finally, a 2.2 nm sample showed only ~ 72 % pore filling. This study showed that the degree of filling depends on the pore size where they are proportional to each other.

He et al. [128] studied the effect of surface modification of a series of mesoporous silica films on the o-Ps lifetime. In a previous work of the authors of [128], they found that the Ps thermalization in mesoporous silica films was not efficient (given by time-of-flight) when the pore surface was modified by adding organic groups (CH_3) than in the pores covered with OH groups. This means that the interaction of Ps with the pore surface is weaker in case of the existence of organic groups in the pore surface. To examine this behavior of positron thermalization, they measured the same films by a slow positron beam where the positron implantation energy was 2 keV. PALS results showed that the average o-Ps lifetime was elongated by modifying the porous surface and adding CH_3 groups. Additionally, the o-Ps intensity was decreased after surface modification regardless the pore size. The decrease in the intensity would be due to the decrease in the surface area or the blocking of o-Ps diffusion from the solid to mesopores after surface modification. This elongation of the o-Ps lifetime in the organically modified films (despite the reduction in the pore size due to the formation of the bulky $OSi(CH_3)_3$) suggest a weak interaction of Ps with the CH_3 groups. To get an agreement between the pore size and the measured o-Ps lifetime in the modified films, the thickness of the electron layer ($\triangle$) in the RTE model was postulated to be different from 0.18 nm. Accordingly, the best fit was obtained by using $\triangle$ = 0.15 nm. The same strategy of changing the $\triangle$ value to get good agreement with the other porosimetry tools was considered in [130] to explain the results of polymer-silica composites which suggest the penetration of silica to the polymer structure. Therefore, these studies showed that PALS measurements can help for predicting the composition of the inner pore surface as the value of $\triangle$ is not universal and it is material-dependent.

Despite the various applications and uniqueness of PALS in porosimetry measurements, it suffers from some constraints. In case of samples containing interconnected or accessible pores and measured by the conventional PALS, the o-Ps will sample all the pores and it will give an average o-Ps lifetime and hence

an average pore size. This issue is problematic if the sample has large and small interconnected pores and their distinguishability is required (bimodal or multimodal porous system) because o-Ps prefers to migrate to the largest pores in view of the fact that its zero energy is the lowest there. Another problem appears in powder samples composed of small particles whose particle size is less than the positron diffusion length. In this case, the formed Ps (during the thermalization or in the beginning of the diffusion) will leave the particle and annihilate in the interparticle spaces. This escape (or migration) of o-Ps will result in an underestimation of the (small) pore sizes found in the sample. The migration of o-Ps should be taken into consideration for any attempts to correlate the intensity of o-Ps in a pore to the pore volume because the migration will reflect a fake intensity (hence pore volume) in the small and large pores. If the slow positron beam is used to study interconnected and open pores to the thin film's surface, the formed o-Ps will escape the sample into the vacuum. The logical solution for this problem is to cap the sample to prevent this escape. But if the sample's surface is so rough, it might be that there will be some uncapped spaces which allow o-Ps escape. Also, the capping process would affect the porous structure due to the diffusion of the capping substance to the pores. For this reason and only in case of there is an o-Ps escape, Liszkay et al. [137] proposed a model to correct the measured o-Ps lifetime in thin films by using the measured lifetime and intensity of the escaped o-Ps into the vacuum. Unfortunately, this model requires a very good detection efficiency of the 142 ns (escaped o-Ps lifetime) and its intensity which needs special geometry and detectors' arrangement. Another possible solution to get rid of the o-Ps escape was suggested by Petkov et al. [122] by using a W shield for the detector.

Chapter 3

Activation and its effect on the porous structure of Metal-Organic-Frameworks

3.1 Introduction

Hosting or confining of guest materials inside porous materials depends on the pore sizes found in the porous materials, their distribution and shape, porosity, and porous specific surface area. The chemistry of the inner pore wall is important because the interaction between the hosted materials and the pore wall or framework is governed by surface chemistry. The mutual interaction between the pore wall and the confined material can be increased by adding some functional groups into the inner pore walls. Such functional groups can direct a self-organization and can define the reactivity and chemical stability [138] of some materials. After the synthesis, the produced pore could have some impurities such as air, gases, and moister from the ambient environment especially, in case of pore interconnectivity with open-surface pores. All of these undesired particles or pollutions would affect the capacity of the pore (by decreasing the available space) as well as the chemistry of the inner porous surface. To get rid of these adsorbed substances and to purge the pores, IUPAC has recommended evacuating (outgassing) the porous samples before their characterization or usage [139].

Usually, researchers mention that they performed the evacuation before characterizing their samples but without enough information about the evacuation process despite its importance [140]. Because it does not have global conditions and it differs from a material to another, activation of porous materials under vacuum and at elevated temperatures should be carefully conducted. When the exact and the optimum activation procedure is not known, wrong estimations of textural properties would mean either an incomplete pore evacuation or pore collapse and the final conclusions are misleading. To recall some examples, physisorbed water in mesoporous materials requires not too high temper-

atures under vacuum while in micropores, as in some zeolites, its outgassing has to be carried out at high temperature, say < 573 K, for long periods [141]. Also, it was advised to apply a sensitive activation procedure with carefulness for organics-containing materials [141] because most of them have low softening or glass transitions points. A thermal stability test has been performed on two different mesoporous silica materials, MCM-41 and FSM-16 by evacuating them at two different temperatures [142]. It was found that the regular hexagonal structure of MCM-41 can be easily deformed upon activating it at high T (> 1073K). In contrast, FSM-16 showed no such a deformation at the same temperature while both samples have maintained their regular structure at 673K. Activation of Linde Type A (LTA) zeolite with sodium as a counter ion (LTA4A) at different temperatures was performed to estimate the CO_2 uptake and it was found that the adsorbed amount of CO_2 increased significantly with increasing the outgassing temperature [140]. The optimal evacuation temperature was found to be in the range 623-723 K. Such a high temperature does not cause any pore collapse because LTA4A is thermally stable and its complete surface cleaning requires a high temperature. This conclusion may explain the discrepancy with [143] for the same material because the samples have been activated till 323 K.

3.2   Objectives

In the first part of this chapter, the aim is to solve the discrepancies between the gas sorption and crystallographic porosities of a cadmium-imidazolate framework. Two different MOF materials, IFP-1 and IFP-6 (imidazolate framework Potsdam-1 and -6), were produced and it was expected, according to Powder X-ray Diffraction (PXRD) measurements, that $D_{IFP-6} > D_{IFP-1}$ where D is the pore diameter. However, the sorption isotherms of N_2, CO_2, CH_4, and H_2 showed a higher gas uptake of IFP-1 than that of IFP-6. It was argued that after IFP-6 activation, pores may be collapsed or blocked and prohibited the gas uptake. One of the main advantages of PALS over fluid-based methods of porosimetry is to detect accessible and buried pores thus PALS was used to prove the pore blockage claim. In the second part of this chapter, an optimized synthesis procedure for preparing a Hydrogen-bonded Imidazolate Framework (HIF-3) is given. The evacuated materials show good N_2, CO_2, and H_2 gas sorption, in comparison with other H-bonded networks. Form the first glance, it means a structure flexibility or induced defect as a result of activation. So, PALS is used, in addition to other methods, due to its sensitivity to defect detection in addition to being a porosimetry tool. Gas sorption of three different

MOF samples synthesized by the Microwave (MW)-assisted conditions showed a higher gas uptake with respect to those synthesized by the Conventional Electrical heating (CE) conditions. Gas sorption and PXRD were unable to explain the reason for such a high gas uptake. For this purpose, PALS was used to investigate the inner porous surface as a trial to explain this gas uptake enhancement. This is the goal of the third part of this chapter.

3.3 Part 1: A PALS study to address gas sorption and crystallographic porosities conflicts of Cadmium–Imidazolate Frameworks

3.3.1 Background

Metal-organic frameworks (MOFs) have been studied extensively during the past two decades due to structure orientated applications, such as gas storage and separation, luminescence, catalysis, sensing, and drug release [144, 145]. However, the predicted surface area estimated by crystallographic measurements is mismatched with the experimentally measured surface area from gas porosity for many MOFs [146]. The underestimation of the expected textural properties was ascribed to many processes like interpenetration, pore collapse, and incomplete guest removal [147–150]. Other compounds, e.g., Zn-HKUST-1 (Hong Kong University of Technology), have such a mismatch between PXRD and gas sorption porosities where Zn-HKUST-1 measured by PXRD showed a crystalline structure maintaining but it showed a negligible N_2 uptake at 77K [146]. Direct detection of such a discrepancy yielded ambiguous results [150]. The explanation of such a failure requires a method which can be used as a porosimetry method for open and collapsed pores and defects. PXRD can be used to study the purity of MOFs but it is not suitable for disorder or defect detection. On the other hand, gas sorption is well suited for accessible internal surface area analysis but it has mass transfer limitations and it cannot probe closed pores [145]. The formation of positronium inside polymers and insulating materials is used to detect any defects, free spaces, or pores. It is well-known that positronium can detect open and buried pores without any use of adsorbent molecules and can be used for in-situ measurements at different temperatures. Additionally, it is suitable for tracing the material changes due to pore blocking, pore-surface densification, pore collapse, and defects in the porous building blocks. Therefore, it is used here to figure out the reasons for the discrepancies between PXRD and sorption methods.

3.3.2 Motivation

A densified surface layer would prevent the entry of even small molecular species into the crystal framework and this can be revealed by PALS [151]. So, the discrepancies between the expected and measured porosities could be due to the pore blocking and pore openings-densification hence, we conducted a PALS study to investigate the porosity of a MOF, IFP-6, and to investigate the effect of the activation of the inner surface of the studied MOFs.

3.3.3 Experimental details

PXRD: Powder X-ray diffraction (PXRD) patterns of IFP-6 and Ln@IFP-6 were measured on a Siemens Diffractometer D5005 in Bragg-Brentano reflection geometry. The diffractometer was equipped with a copper tube, a scintillation counter, automatical incident- and diffracted-beam soller slits and a graphite secondary monochromator. The generator was set to 40 kV and 40 mA. All measurements were performed with sample rotation. Data were collected digitally from $3°$ to $70°$ 2ϑ using a step size of $0.02°$ 2ϑ and a count time of 4 seconds per step. The simulated powder patterns for IFP-6 and Ln@IFP-6 were calculated using single-crystal X-ray diffraction data and processed by the free Mercury v1.4.2 program provided by the Cambridge Crystallographic Data Centre.

The experimental details of single crystal X-ray are presented in the supplementary information of [150].

Gas sorption measurements: sorption isotherms were measured using a Micromeritics ASAP 2020 automatic gas sorption analyzer equipped with oil-free vacuum pumps (ultimate vacuum $< 10^{-8}$ mbar) and valves, which guaranteed contamination-free measurements. The sample was connected to the preparation port of the sorption analyzer and degassed under vacuum until the outgassing rate, i.e., the rate of pressure rise in the temporarily closed manifold with the connected sample tube, was less than 2.66×10^{-6} mbar/min at the specified temperature 473 K for 48 h. After weighing, the sample tube was then transferred to the analysis port of the sorption analyzer. All used gases (H_2, He, N_2, CO_2, CH_4) were of ultra-high purity (UHP, grade 5.0, 99.999%) and the STP volumes are given according to the NIST standards (293.15 K, 101.325 kPa). Helium gas was used for the determination of the cold and warm free space of the sample tubes. H_2 and N_2 sorption isotherms were measured at 77 K (liquid nitrogen bath), whereas CO_2 and CH_2 sorption isotherms were measured at 298 ± 1 K (passive thermostating) 273.15 K (ice/deionized water bath) and 195.0 K (acetone/dry ice). The heat of adsorption value and the NLDFT

with a "CO_2 on carbon based slit-pore" model were done using the ASAP 2020 v3.05 software. Supercritical CO_2 activation of the sample was done on Leica EM CPD300 Auto instrument.

PALS: The measurements were performed using a digital PALS with 225 ps FWHM consists of two plastic detectors with ϕ 40mm $\times$ 30mm coupled to two Hamamatsu PMTs connected to an 8-bit digitizer. LT10 [152] program has been used for extracting the lifetime components. The pore size determination, based on the ETE model (equation 2.33), was done using Excited Energy Levels and Various Shapes (EELViS) [153] program. LT10 gave for all the samples four lifetime components which have the following meanings; τ_1 is the parapositronium lifetime component (0.125 ns, fixed), τ_2 is the free positron annihilation lifetime in the sample, τ_3 is the o-Ps annihilation lifetime inside the material matrix and/or inside small micropores, and τ_4 is the o-Ps annihilation in the large pores.

The synthesis procedure is given in Appendix B.1.1.

3.3.4 Results and discussions

3.3.4.1 Structure determination

The structure of IFP-6 was determined by single-crystal X-ray crystallography and was found to be isostructural to that of IFP-1 with the same etb topology. The asymmetric unit contains one Cd^{II} ion and the bridging ligand L1 (figure 3.1.a). The Cd^{II} ion is pentacoordinated by the donor atoms of three L1
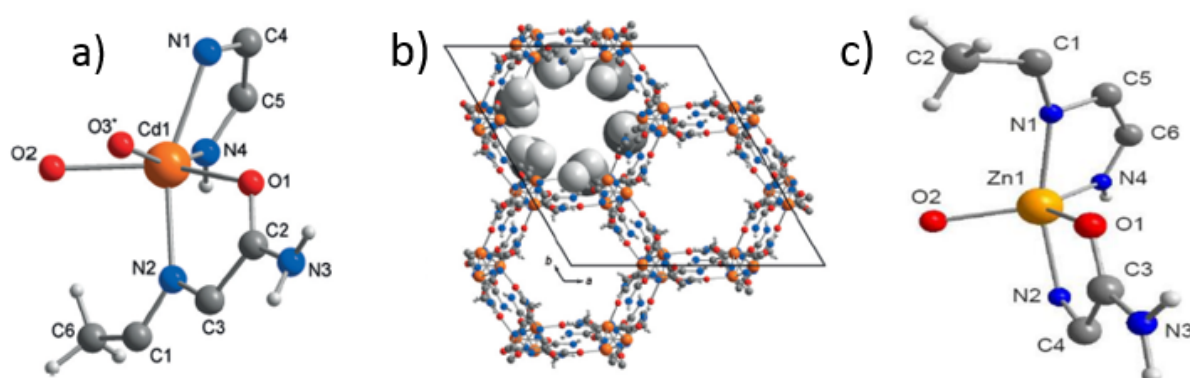
Figure 3.1: a) Asymmetric unit of as-synthesized IFP-6 (O3* is only 20% occupied). b) Hexagonal channels in IFP-6 (the methyl substituents at linker L1 are presented in space-filling mode). c) Asymmetric unit of the IFP-1 (orange Cd or Zn, blue N, red O, dark gray C, light gray H) [150].

.

ligands to form a distorted environment with a trigonal–bipyramidal geometry.

On the other hand, solvent molecules are not coordinated to Zn ions in the IFP-1 structure, which forms only pentacoordination by the L1 linkers in a distorted trigonal–bipyramidal geometry (figure 3.1.c). The structure of IFP-6 possesses 1D hexagonal channels running along the c axis. The methyl groups protrude into the open channels and influence the accessible pore window (figure 2.2.b). By taking into account the van der Waals radii, IFP-6 has an accessible pore window of 0.52 nm. The channel diameter of IFP-6 exceeds that of isostructural IFP-1 where (IFP-1 (0.42 nm, M=Zn^{II})<IFP-6 (0.52 nm, M=Cd^{II})). This is because of the larger cation radius of Cd^{II} and the 42.9% solvent accessible space contained in IFP-6 (given by PLATON toolkit [150]). This structure is obtained by PXRD in figure 2.3. From crystallographic data it was found that IFP-6 contains 0.75 H_2O and 0.5 DMF molecules per formula unit. In order to get rid of these solvent molecules, IFP-6 sample was activated at 473 K for 48 h. PXRD patterns of the activated sample exhibited similar diffraction peaks to those of the as-synthesized framework (figure 3.2). Thus, the porous framework has maintained the crystalline integrity, even without solvent molecules. Additionally, the asymmetric unit of activated IFP-6 showed fivefold coordination (similar to IFP-1 before and after activation) while it was sixfold before activation. Coordinated water and solvent molecules in the channels were removed through the activation process with very little effect on the cell parameters and volume, showing structural identity.
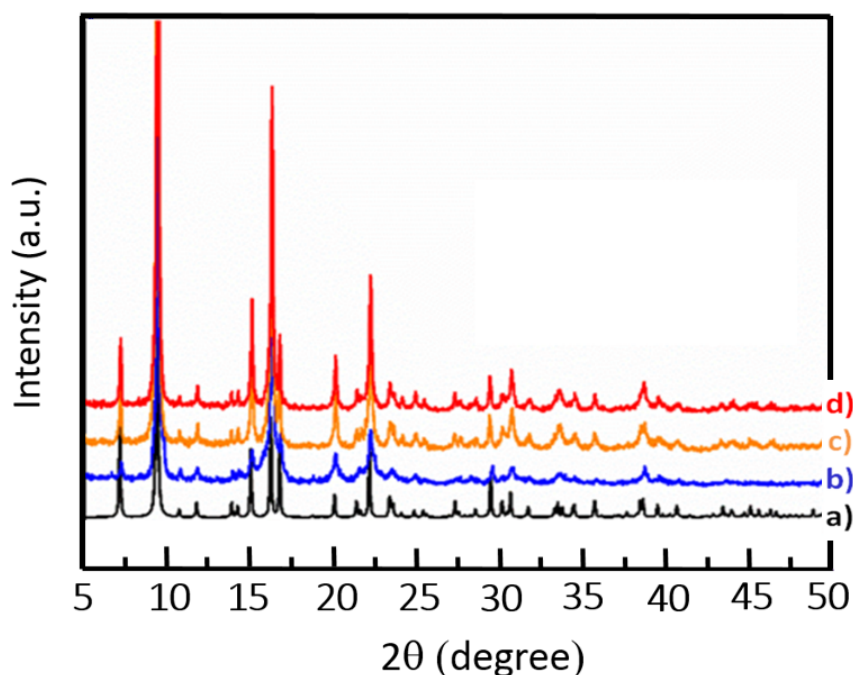
Figure 3.2: PXRD patterns of IFP-6: a) simulated, b) as-synthesized, c) activated, d) after gas uptake of CO_2 and CH_4.

3.3.4.2 Gas sorption

It was expected that gas uptake of IFP-6 should be comparable or higher than gas uptake of IFP-1 because of its larger pore aperture and void volume. Surprisingly, N_2, H_2, and CH_4 cannot be adsorbed by IFP-6 at various temperatures and 1 bar (figure 3.3 and table 3.1), although the kinetic diameter of the gases is smaller than the effective pore window size (0.52 nm). Compared with IFP-1, a low amount of CO_2 adsorbed by IFP-6 and a broad desorption hysteresis were observed (figure 3.3 and table 3.1). To figure out reasons for such a hysteresis, the adsorption enthalpy was calculated and it was found that it is increased as a function of the adsorbed CO_2 volume which has a similar behavior reported for several amide-containing MOF [150]. This led to the convincing interpretation of this broad desorption hysteresis as intermolecular amide interactions with CO_2 molecules based on isosteric heat measurements. To investigate the
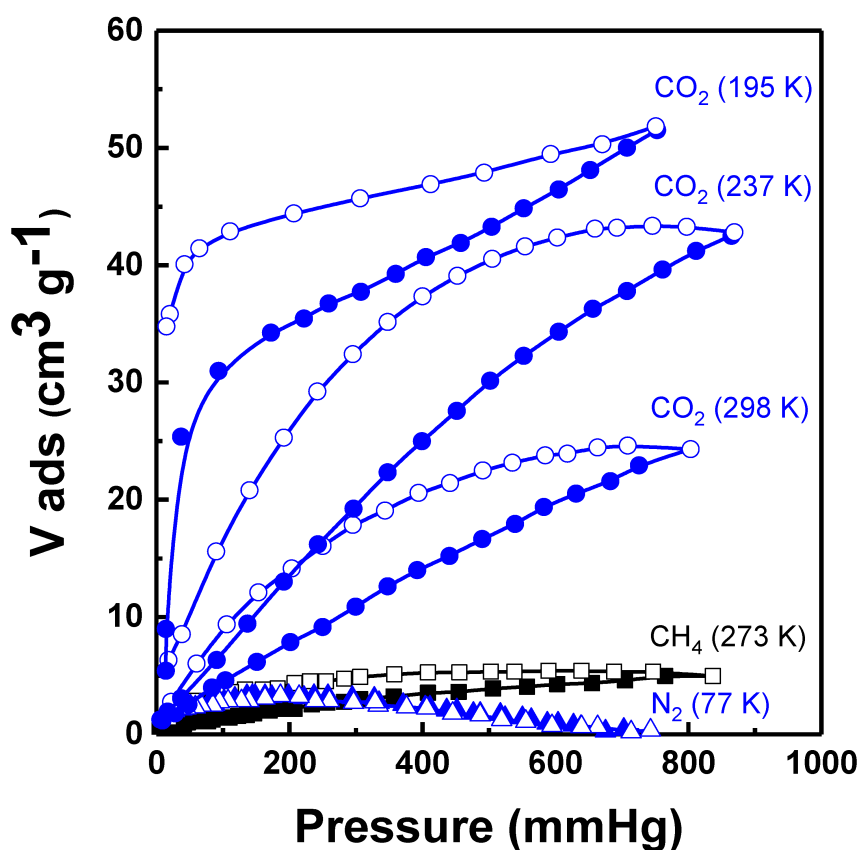
Figure 3.3: Gas sorption isotherms of IFP-6 for N_2, H_2, and CH_4 (adsorption and desorption branches are indicated by closed and open symbols, respectively). The higher CO_2 amount upon desorption at 273 K is an artifact of the low equilibration time of 20 s per data point. At equilibration intervals of 60 and 120 s, the desorbed amount of CO_2 stays below the adsorption maximum. Because the increasing equilibration time also increases the overall CO_2 uptake, the 273 K curve is shown herein for 20 s of equilibration for comparison with the other temperatures.

Table 3.1: Gas sorption data (in cm^3g^{-1}) of IFP-6 in comparison with IFP-1

Sample	IFP-6	IFP-1
pore window [nm]	0.52	0.42
N_2 (77K)	0	224.6[a]
CO_2 (298K)	22.4	48[a]
CO_2 (273K)	39.5 and 132.2[b]	-[c] and 156.9[b]
CO_2 (195K)	51.7	-[c]
CH_4 (273K)	4.2 and 87.4[b]	31.4 and 127.8[b]
H_2 (77K)	1.1	168.1[a]

[a]From ref. [154]; [b]Gas sorption at high pressure up to 50 bar [155]; [c]Not reported

adsorption properties at higher pressures, CO_2 and CH_4 adsorption isotherms on IFP-1 and IFP-6 were reported at 273 K up to 50 bar [155]. A significant amount is adsorbed by IFP-6 at high pressure; this is comparable to IFP-1. Interestingly, IFP-6 maintained crystallinity after high-pressure gas uptake (figure 3.2), whereas at least part of the IFP-6 framework broke down during the activation process to create an instability of the surface. Fractions, which turn amorphous, are not detectable by PXRD. It was assumed that a partial deterioration of the material and closing of the 1D channel pores was produced. Therefore, the diffusion of gas molecules at atmospheric pressure is restricted whereas at elevated pressure, gas molecules are compelled to diffuse into the pores. Such a phenomenon is not common but has been reported for microporous MOFs [156].

3.3.4.3 PALS

The PALS method can provide evidence for the presence of inner pores in solvent-free IFP-6, although the pores probably are blocked by amorphous phases. For comparison, PALS of IFP-1 was measured under similar conditions. The samples were activated at 473 K for different times and the effect of the activation on the o-Ps lifetimes and the related intensities is depicted in figure 3.4. As it can be seen in figure 3.4 (left), τ_3 for IFP-6 is larger than that of IFP-1 along all the activation periods and becomes nearly stable for both samples starting from 3 h of activation (except for 48 h for IFP-6). In the as-received IFP-6 sample (0 annealing time, measuring under vacuum at RT), since the value of τ_4 (3.7 ns) is close to τ_3 (2.8 ns) but it reaches ~22 ns after 3 h of activation, so τ_4 can be considered as a representation of defect formation due to the collapse of the linker of some primary pores. After 3 h of activation, τ_4 of IFP-6 is increasing with the activation times then, starting from 50 h of activation, it shows a constant value.

Regarding the intensities (which reflect the pore concentration); I_3 (in the small
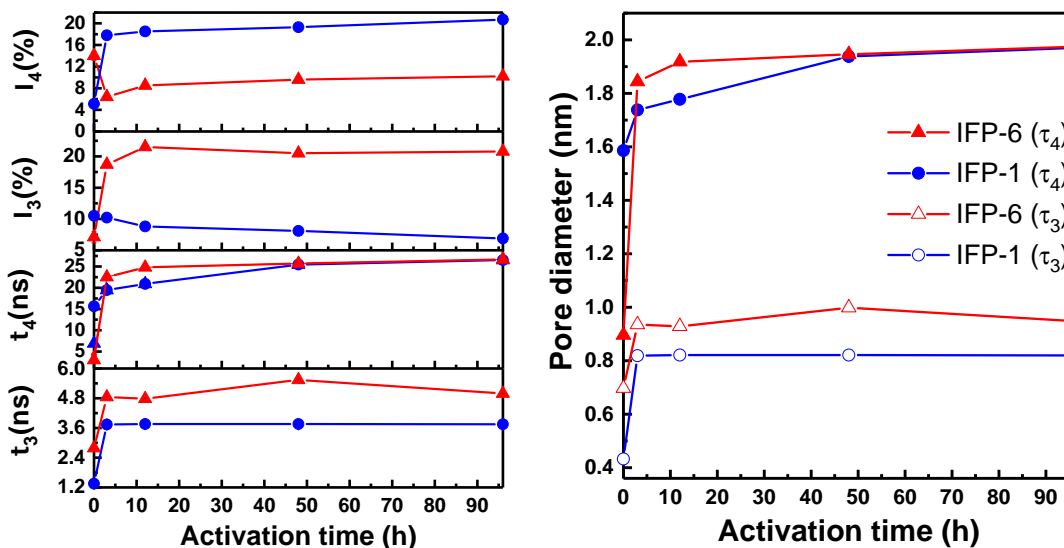
Figure 3.4: Left: o-Ps lifetimes and their intensities of IFP-6 (red triangles) and IFP-1 (blue circles) annealed at 473 K as functions of annealing time. Right: Spherical pore diameters of IFP-6 and -1, as functions of annealing time.

pores) of sample IFP-6 increases with the activation time reaching a stable stage at 12 h of activation while it reduces in IFP-1 from $\sim$ 11 % till 8 % at 12 h of activation and afterwards, it shows nearly equal values. I_4 (inside the large pores) of IFP-6 has its highest value for the as-received sample and it decreases with the activation time till 12 h of activation, with a minimum at 3 hrs of activation, then it becomes constant. While the intensity of IFP-1, I_4, is increasing due to the activation and it is nearly constant starting from 3 h of activation (with a very slight increase with the activation time) (figure 3.4, left); this may be understood as a nearly complete cleaning of sample IFP-1 after only 3 h of activation.

The effect of activation on the pore sizes is shown in figure 3.4, right and, based on crystallographic data, it is anticipated that the geometrical shape of the samples could result from spherical pores. The determined pores size of IFP-6 from τ_3 has a constant value after solvent removal (figure 3.4, right). From the CO_2 adsorption isotherm at 273 K for IFP-6, the pore size distribution was derived to be between 0.4 and 1.0 nm by using nonlocal (NL) DFT which showed a relative maximum at about 0.98 nm. This maximum value is comparable to a small pore diameter ($\approx$0.95 nm) obtained from the pore size versus annealing time data from PALS (the average pore size at different times of activation with excluding the value of the as-received sample) and the value is also close to that of a small pore (1.25 nm) obtained from the X-ray structure. Additionally, PALS shows a large pore of 1.95 nm in diameter. This value fits with pores (2.04 nm) obtained from the X-ray structure of IFP-6. Moreover, the pore size

behavior of IFP-6 is similar to that of IFP-1.

To this end, PALS has confirmed that the IFP-6 sample has pore apertures larger than those of IFP-1 and it can help for solving the conflicts between crystallographic and sorption porosities. From the intensity behavior of IFP-6 of the large pores (defect), it was found that the intensity decreases with the activation time (even at 3 h). Such a decrease means the disappearance of some pores (defects) as a result of the activation due to their filling by some linkers or collapse due to their densification. Such a densification would result in the blocking of the remaining small pores. It should be mentioned here that the increase in I_3 of IFP-6 could be a result of the missing of the large pores or higher Ps yield owing to the densification.

Thereby the behavior of IFP-6 could be reasonable due to inherent surface densification after solvent removal, which renders it impermeable to molecular guests. The reason could be the formation of an amorphous phase, as a result of the more flexible fivefold coordination of the Cd^{II} center of activated IFP-6, which was proved by single-crystal X-ray data, than that of fivefold coordination around the Zn^{II} center in IFP-1 (see section 3.3.4.1). The crystal structure showed that 20% of Cd^{II} ions were prone to sixfold coordination, which indicated that Cd^{II} preferred higher coordination. An alternative hypothesis can be supported by the water instability of IFP-6, which attains a higher coordination number in polar water solvent. Thus, the solvent removal process may facilitate instability at the Cd^{II} center. Hence, the amorphous material and rough surface can be generated by partial framework cleavage at the outer surface, which closes the pore window. Therefore, IFP-6 has inherent crystal defects [157, 158]. At atmospheric pressure, gas molecules could probably not diffuse due to blockage by the amorphous phase, created after solvent removal, whereas, at high pressure, gases are compelled to diffuse into the pore.

3.3.5 Conclusion

A rare example of an imidazolate anion based IL as a linker precursor for the fabrication of a MOF, IFP- 6, in DMF was employed. Such modification of a linker to an IL could be useful in the future for other tri- and tetrazoles or derivatives. IFP-6 showed low performance for N_2, H_2, and CH_4 uptake from vacuum to atmospheric pressure at various temperatures, although the channel diameter was higher than the molecular sizes of the gases and the bulk MOF exhibited structural integrity after solvent removal. At elevated pressure, CO_2 and CH_4 were taken up by the pores of IFP-6, and the respective uptake capacities were comparable to Zn^{II}-based isostructural IFP-1. For a deeper understanding of

the porosity, PALS has been undertaking to demonstrate the unique ability of exposing nanoscale porosity; this vindicated the supposition that the presence of inner pores in IFP-6 was comparable to those of IFP-1. From the annealing behavior, the intensities inside large pores (I_4) of IFP-6 decreased, which could be attributed to filling of the pore due to the collapse of pore apertures. In-depth porosimetry studies by using PALS have so far been performed for very few MOFs, such as MOF-5 and Zn-HKUST-1. From the results for IFP-6, it can be inferred that the channels to the inner pores are blocked by amorphous parts and defects in IFP-6 that are inherently formed upon removal of the water molecules coordinated to Cd^{II}. Hence, diffusion of gas molecules is only possible at elevated pressure, which forces gases through these barriers into the retained inner pores.

3.4 Part 2: Activation-induced defects of Hydrogen–bonded Amide-Imidazolate Network studied by PALS

3.4.1 Introduction

As a result of the extensive investigation of metal-organic frameworks (MOFs) and covalent-organic frameworks (COFs), novel porous materials with interesting properties suitable for gas storage/separation, sensing, catalysis, photovoltaics, and drug release [159] were produced. Compared with MOFs and COFs, the hydrogen-bonded organic frameworks (HOFs) and also including the rare class of hydrogen-bonded molecular building blocks (MBBs), self-assembled frameworks through weaker hydrogen-bonding interactions among molecular organic linkers are much more fragile and difficult to stabilize [160–162].

Few examples of HOFs with outstanding properties and stable porosities for the mixture gas separation were realized [163] which make these materials as a new class of functional materials [164]. The research on HOFs with the permanent porosities and functional properties is still not too much. Therefore, it is necessary to figure out the reason for the less porous behavior of the structural backbone of H-bonded networks as it is expected.

Recently, there has been a renewed interest in the exploration of defects in MOFs [165]. Introduction of defect sites into ordered structures is also a useful strategy to realize unusual heterogeneous structures and properties. Here, the "defect" term means the sites that locally break the regular periodic arrangement

of atoms or ions of the static crystalline parent framework because of missing or dislocated atoms or ions [163] which can be produced after solvent removal by thermal or vacuum activation [166]. Regarding the defect production in porous materials, the H-bonding is brittle and weak which means that its presence in HOFs may collapse the porous network or change the structure after solvent removal and produce defects in the material matrix. Thus, detailed studies of the organic linkers for the HOFs constructions and framework rigidity and flexibility are crucial before utilizing the rich chemistry of HOFs to synthesize porous functional materials. Such a detailed study is the goal of this part.

3.4.2   Methodologies

An optimized synthesis of an imidazolate- 4,5-diamide-2-olate (L2) linker based H-bonded Cd_{14}-MBBs network, named as HIF-3 and its gas uptake properties are reported here. Depending on the treatment conditions, two types of HIF-3 were produced; HIF-3-CE (under solvothermal conditions by conventional electric heating) and HIF-3-MW (via microwave-assisted conditions). The synthesis of these materials is shown in Appendix B.2.1. For the removal of solvents, the HIF-3 materials were not activated thermally in order to avoid any stress for the hydrogen-bonding pattern. Instead, the material was placed in a Soxhlet extractor and extracted with dry methanol over 5 days. The solvent-exchanged material was activated by degassing at 333 K under high vacuum ($\sim 10^{-6}$ mbar) for 24 h, prior to gas sorption measurements. PALS method was used in this study to investigate the temperature-dependent porosity of HIF-3 and to explain the behavior of the inner surface property and defects crystalline structures due to missing of MBBs. The experimental details of single X-ray, PXRD, gas sorption, and PALS measurements are the same as described in part 3.3.3.

3.4.3   Results and discussions

3.4.3.1   Structure identification

Single-crystal X-ray diffraction pattern showed that the as-synthesized HIF-3-CE has the structure $[Cd_{14}(L2)_{12}(O)(OH)_2(H_2O)_4(DMF)_4]$ $(DMF)_8$. Figure 3.5.a shows that the compound HIF-3-CE crystallizes is in a high-symmetry space group where such a symmetric unit contains five different cadmium centers (which is rarely observed [163]). Twelve L2 ligands, one O^{2-}, two OH^- ions, four water and four DMF molecules, assemble with fourteen Cd ions to form a tetradecanuclear Cd_{14}-MBB with peripheral amide groups. An oxido ion
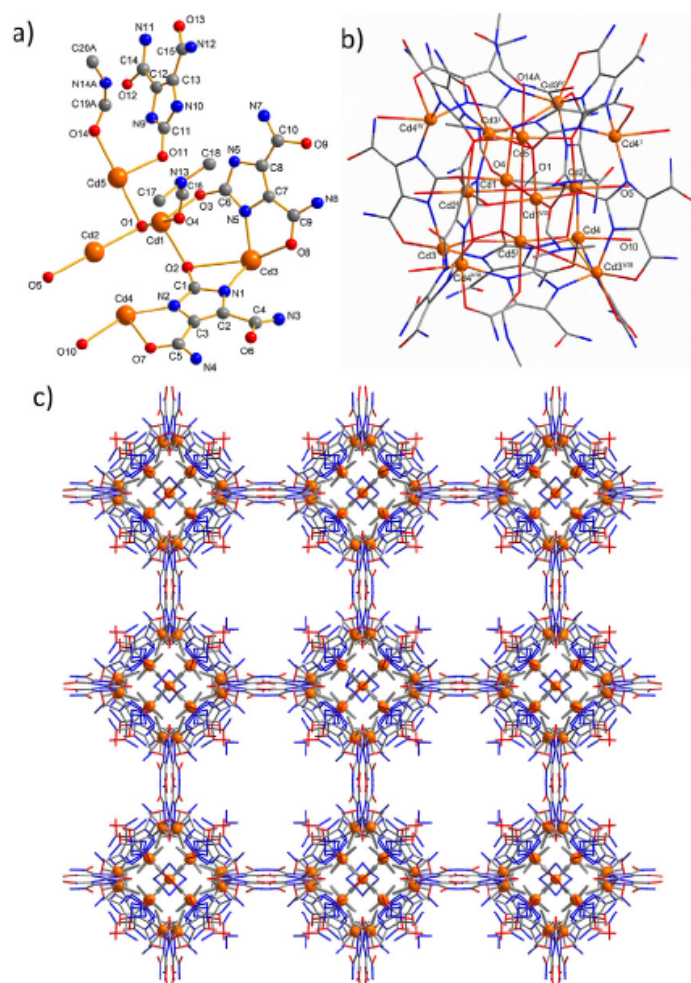
Figure 3.5: Crystal structure of HIF-3: a) asymmetric unit, b) tetradecanuclear Cd_{14}-MBB and c) hydrogen-bonded supramolecular assembly of HIF-3-CE (orange Cd, blue N, red O, and dark gray C; H atoms are omitted for clarity).

(O1) is located in the center of the Cd_{14}-MBB, surrounded by two Cd_1, two Cd_2 and two Cd_5 atoms in a octahedral coordination environment (figure 3.5.b). The MBB contains amide groups at its vertices and edges. Each cubic-like MBB is connected through its vertices with eight MBBs in a body-centered cubic packing (figure 3.5.c). The framework shows one type of infinite 1D channels with openings of 1.16 nm between the van-der-Waals surfaces (figure 3.5.c). The channels of as-synthesized HIF-3-CE contain two DMF molecules per formula unit, in a solvent-accessible void volume of 24% of the unit cell volume. The purity of the as-synthesized materials, HIF-3-CE and -MW was confirmed by PXRD patterns (figure 3.6).
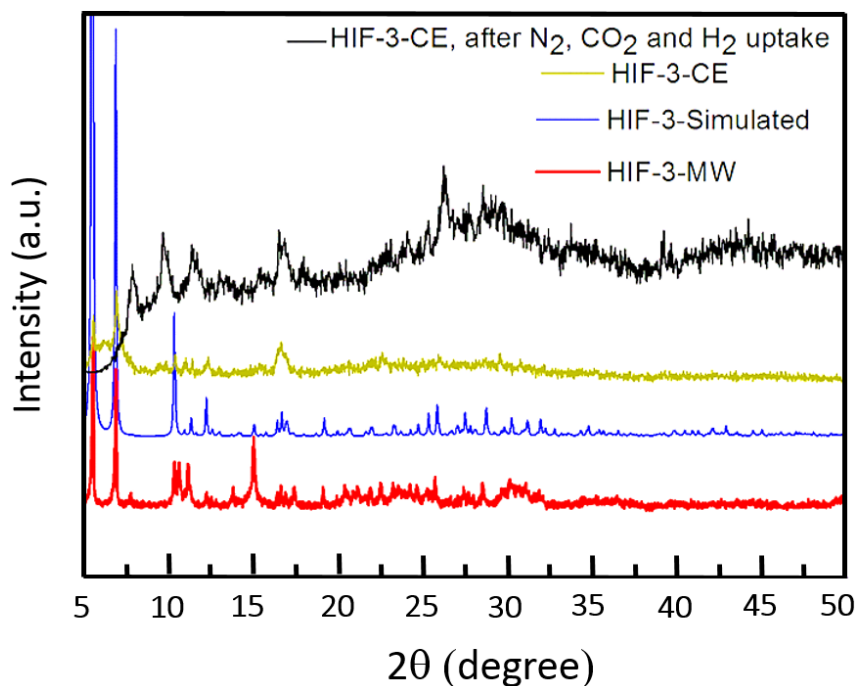
Figure 3.6: Powder X-ray diffraction patterns of as-synthesized HIF-3-CE and as-synthesized HIF-3-MW; Difference in the relative intensities is because of the simulated pattern does not account for the disordered solvent molecules in the HIF-3 pores.

3.4.3.2 Gas sorption

Nitrogen sorptions for the activated HIF-3-CE and -MW measured at 77.4 K up to a relative pressure of 0.995 are shown in figure 3.7.a which mimic type II of isotherms. The BET surface area for HIF-3-CE and HIF-3-MW was estimated to be 127 and 43 m^2g^{-1}, respectively. On the other hand, the CO_2 adsorption at 273 K for the samples is shown in figure 3.7.b and the adsorption capacities are 18 and 14 cm^3g^{-1} in the activated HIF-3-CE and -MW, respectively. The pore size distribution of HIF-3-CE driven from the CO_2 sorption isotherms at 273 K by using NLDFT (figure 3.7.c) was estimated between 0.4 and 1.0 nm which showed a relative maximum at ~0.88 nm that is comparable with the channel (1.16 nm) obtained from the X-ray structure. HIF-3-CE and -MW adsorb 15 and 9 cm^3 g^{-1} of H_2, respectively at 77 K and 1 bar. Obviously, all adsorption branches in figure 3.7.a and .b are irreversible with a wide hysteresis which may indicate a structural flexibility or structural irregularities of the material during the gas uptake. Such a flexibility maybe caused by the H- bonding in the material which hardly stabilizes the framework and the porous structure is anticipated to be collapsed or to produce structure transformations once the solvent guest molecules are removed after thermal and/or vacuum activation. This is proven by a certain degree of hysteretic desorption isotherms of other H-bonded porous materials [167,168]. After gases uptake, the HIF-3-CE structure
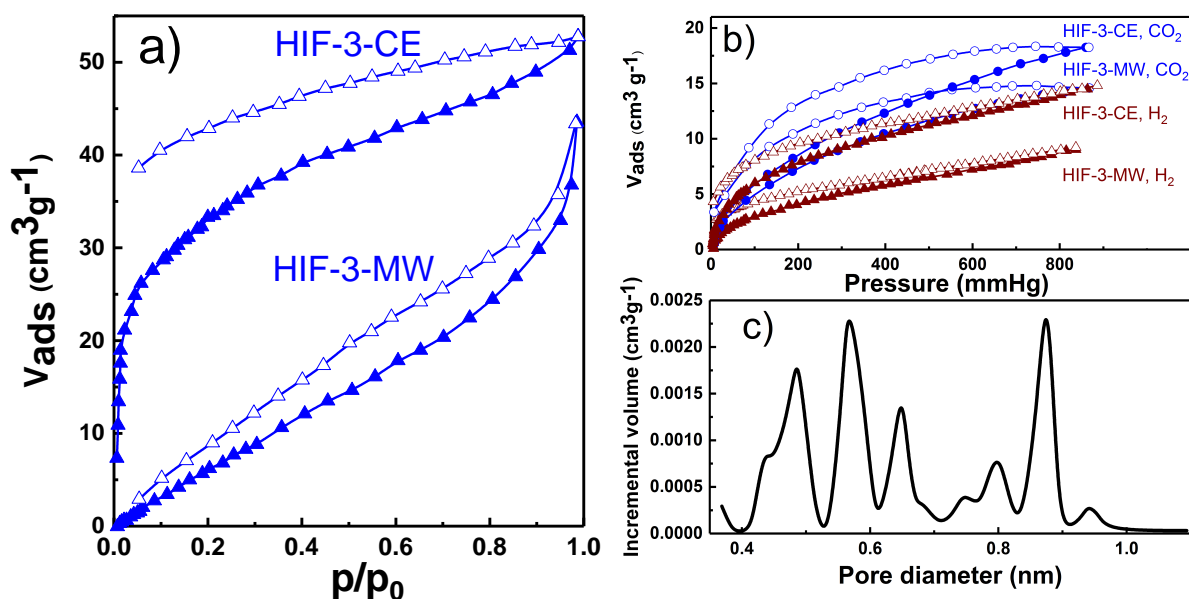
Figure 3.7: a) N_2 (at 77.4 K) , b) H_2 (at 77 K), and CO_2 (at 273 K) sorption isotherms of HIF-3(adsorption and desorption branches are indicated in closed and open symbols, respectively), and c) the pore size distribution of HIF-3-CE from a CO_2 adsorption isotherm at 273 K.

is transformed into an unknown crystalline material, although the crystallinity is maintained (figure 3.6) that could complementarily be supported by the broad desorption hysteretic isotherms during gas uptake. It is interesting to analyze the inner porosity and stability of the soft frameworks when the materials were heated at elevated temperatures. For doing that, variable temperature PALS measurements were conducted to probe the inner surface of HIF-3.

3.4.3.3   PALS

As discussed before, PALS is sensitive to defect detection due to the attraction potential of positron to the low electron density sites. Since porous materials contain low electron density and pores, positron forms positronium inside them and it is getting trapped in the pores where its lifetime (of o-Ps) is governed by the pore size. It was proven by Matzger-Gidley group that PALS has inherent advantages over gas sorption techniques as an analytical tool to study porous MOFs such as Zn- HKUST-1 and MOF-5 [151]. It should be mentioned here that the lifetime subscripts have the same meanings as in section 3.3.3.

The effect of the activation temperatures during different periods on the positron lifetime, the pore size, and the intensities of HIF-3-CE are shown in figure 3.8. The pore size (figure 3.8.b), derived from τ_3 is smaller and more stable than the pore size, getting from τ_4, and at 323, 373, and 473 K, it is constant after 12 hours annealing time while for 423 K, the pore size is slightly reduced. The small pore size is reduced with the increase of the activation temperature, indi-

cation the pore destruction upon heating the material. Interestingly, the PXRD
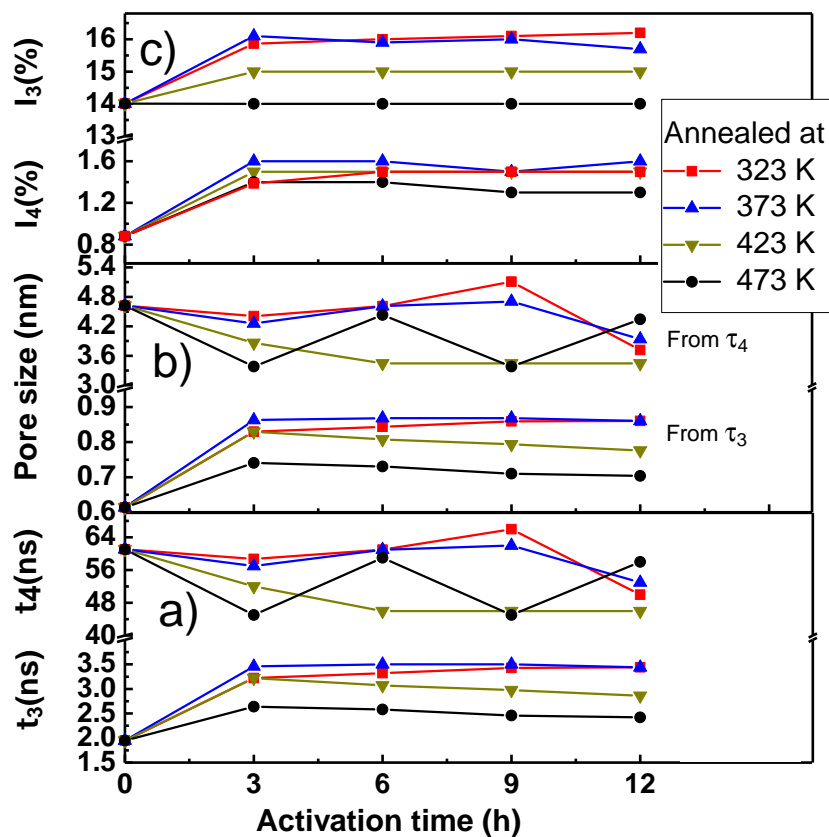
Figure 3.8: a) O-Ps ifetime, b) pore size, and c) o-Ps intensity of HIF-3-CE as functions of activation time at different temperatures (the data points have the same size as their errors). The symbols and colors meanings are shown in the figure.

reflections of activated HIF-3-CE are shifted toward higher Bragg angles, suggesting a structure contraction upon activation of the material (figure B.3 in Appendix B.2.2). The larger pore, obtained from τ_4, has changed drastically during heating above 423 K and τ_4 is inversely proportional to the annealing temperature along with all periods (except at 423 K for 9 hours). Importantly, at 473 K activation temperature, a more dynamic behavior of the large pore is observed. The small pore and large pore size, after 12 h of annealing time at 373 K, are 0.87 and ≈ 3.9 nm, respectively. The small pore diameter, obtained from τ_3 is comparable with the pore size distribution of CO_2 (relative maximum at ≈ 0.88 nm) and also close to X-ray structure (1.16 nm). It has been also noted that $I_4 < I_3$ during all periods of activation which means that the HIF-3-CE has a small concentration ($\approx 10\%$ at 373 K activation temperature after 12 h annealing time, figure 3.9.a) of large pores and the remaining of small pores. However, the crystal structure does not indicate such a small concentration (10%) of large pores with a pore size of 3.9 nm. This could probably the missing molecular building blocks at a few areas of crystal structure, creating
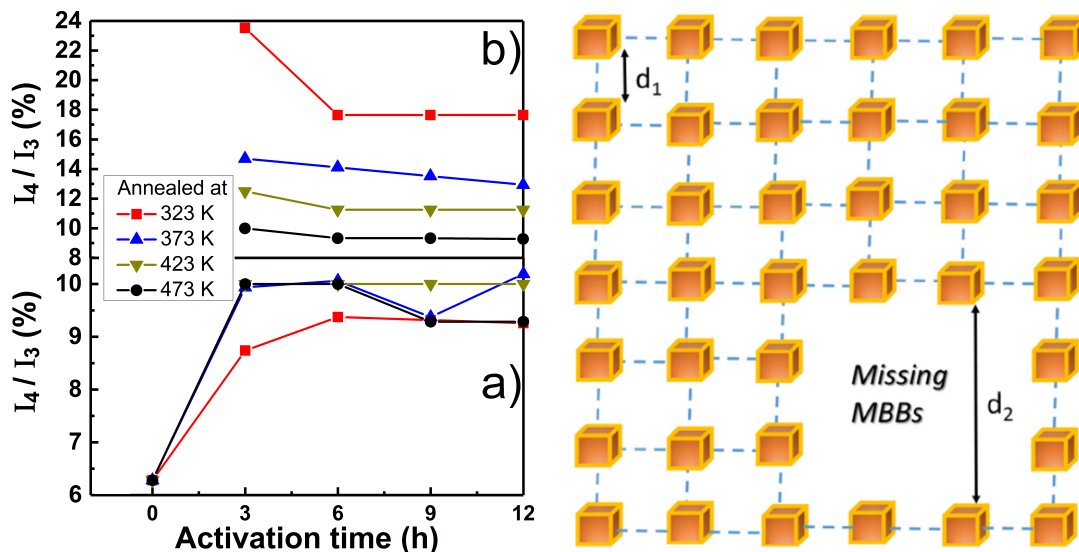
Figure 3.9: Left: intensity ratio of o-Ps lifetime of a) HIF-3-CE and b) HIF-3-MW at different annealing temperatures as functions of annealing time. Data points and their errors have the same size. Right: schematic illustration of H-bonding patterns with missing MBBs (d_1=0.87 nm (from τ_3) and d_1= ~3.9 nm (from τ_4)).

the mesopore regions that make instability of the H-bonded network (figure 3.9, right) and also a complementary proof by the hysteretic desorption isotherms. This phenomenon also suggests that at first the MBBs are formed and after that, these are connected by H-bonds. So, from here on the subscript "4" will be renamed to indicate defects due to the missing building blocks.

For HIF-3-MW, the effect of the activation on lifetime, pore size, and intensity is shown in figure 3.10 which showed a delayed appearance of τ_4 after 3 h activation at all temperature. It has been also observed that $I_4 < I_3$ (figure 3.9.b) during all periods of activation, confirming a small concentration ($\approx$ 14%, at 373 K activation temperature after 12 h annealing time, figure 3.9.b) of defects which are comparatively higher than HIF-3-CE (10%). The fixed (and lower) intensities of I_4 at temperatures higher than 323 K (figure 3.10.c) may suggest that during the activation at different temperatures, some of these defects have disappeared or filled with the protonated form of non-coordinated L2 linkers which could be stable in the reaction medium and unable to leave the defects. Additionally, inductively coupled plasma optical emission spectrometry results (table 4.4) for HIF-3 suggest that MW-assisted condition showed less Cd-content which implies defects in the structure and indirectly support the extra noncoordinated linkers incorporation. The reasons can be inferred that very fast crystal growth under MW-assisted conditions may not ensure enough time for the MBBs to quantitatively adhere to the growing crystal lattice at the right place, and hence, more pronounced missing MBBs defects are obtained, where
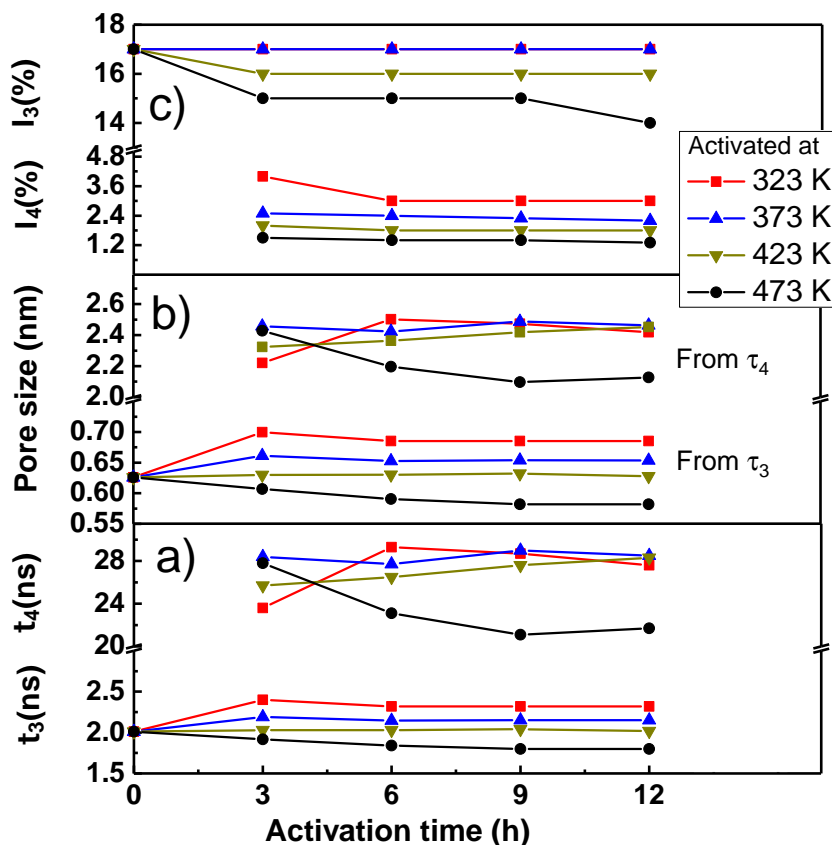
Figure 3.10: Effect of activation on a) o-Ps lifetime, b) pore size, and c) o-Ps intensity of HIF-3-MW. The errors have the same size as the data points.

the linkers are trapped inside pores, reducing the pore sizes obtained from τ_3 and τ_4 (small and large pore of 0.65 and 2.5 nm, respectively at 373 K activation time). Moreover, MW-assisted conditions, the pore size i.e., mesopore or defect formation, getting from τ_4 values, is highly dominant than CE-methods. Hence, the material synthesized under MW-assisted conditions is more flexible to the structural transformation during activation, proven by less gas uptake, compared to the material synthesized under CE-conditions.

Table 3.2: Inductively coupled plasma optical emission spectrometry (ICP OES) result for HIF-3

Material	Cd- content
HIF-3-CE	361.8 mg/g
HIF-3-MW	315.1 mg/g

3.4.4 Summary

In situ linker generation method for the synthesis of a rare class of molecular building blocks that are connected by H-bonds into a porous supramolec-

ular network was described. Thermodynamically driven HIF-3-CE exhibited slightly larger N_2, CO_2, and H_2 uptakes than the kinetically controlled HIF-3-MW. CO_2 uptake capacities are comparable with the known H-bonded porous organic compounds, although the broad hysteretic desorption isotherms imply structural changes during gas sorption. PALS was used to demonstrate these structural changes. Such an investigation by PALS clearly suggests that missing building blocks defects (10 and 14% for HIF-3-CE and -MW, respectively) are formed in the crystalline materials. This portion of defects showed more dynamic structural changes during annealing and activation process wherein, micropores remain static in annealing time and decrease with increasing the activation temperatures. The porosimetry investigations by PALS enable a basic understanding of the H-bonding patterns and defects as well as the porosity of the H-bonded porous materials.

3.5 Part 3: Insight into the porous structure of metal–imidazolate frameworks having high gas uptake

3.5.1 Scientific case

Several methodologies, like functionalization of the porous surface with amines [169–171], unsaturation of the metallic sites [172], and more recently defect engineering of MOFs [173] (defect formation during the synthesis or by post-synthetic treatment), have been evolved to improve gas uptake by MOFs. Also, it was reported that MW-assisted synthesis of MOFs exhibited an enhancement of N_2 and CO_2 uptake capacity, compared to the analogous CE-heating method based materials [174–176]. However, no detailed investigations on the origin of the high guest uptake capacity of MW-assisted materials have been carried out. In this part, three MW-assisted isostructural frameworks IFP which show strong enhancement of CO_2 and H_2 uptake capacities are investigated. These three samples have flexible methoxy and ethoxy linker arms of the chelating linker 2-substituted imidazolate 4- amide 5-imidate, named IFP-7-MW [177] (M = Zn, R = OMe), IFP-8-MW (M = Co; R = OMe) and IFP-10-MW (M = Co; R = OEt). Thus, the aim here is to understand the reasons for the high gas uptake of materials synthesized by the MW-assisted conditions compared with the same materials synthesized by CE-heating methods. This study is performed by PALS in addition to other characterization methods.

The preparation steps of the investigated samples (according to the procedure

given in [178, 179]) are given in appendix B.3.1 and the experimental details of the all used methods are the same as described in section 3.3.3.

3.5.2 Results and discussions

3.5.2.1 Structure investigation

The identity of these MW materials was verified by PXRD which showed a well matching with the diffractograms of samples synthesized under CE-conditions and simulated ones from the single-crystal X-ray structures (figure 3.11). Scanning electron microscopy (SEM) images revealed small particles with different morphologies for IFP-7, -8 and -10 each (figure 3.11.d). The materials are ac-
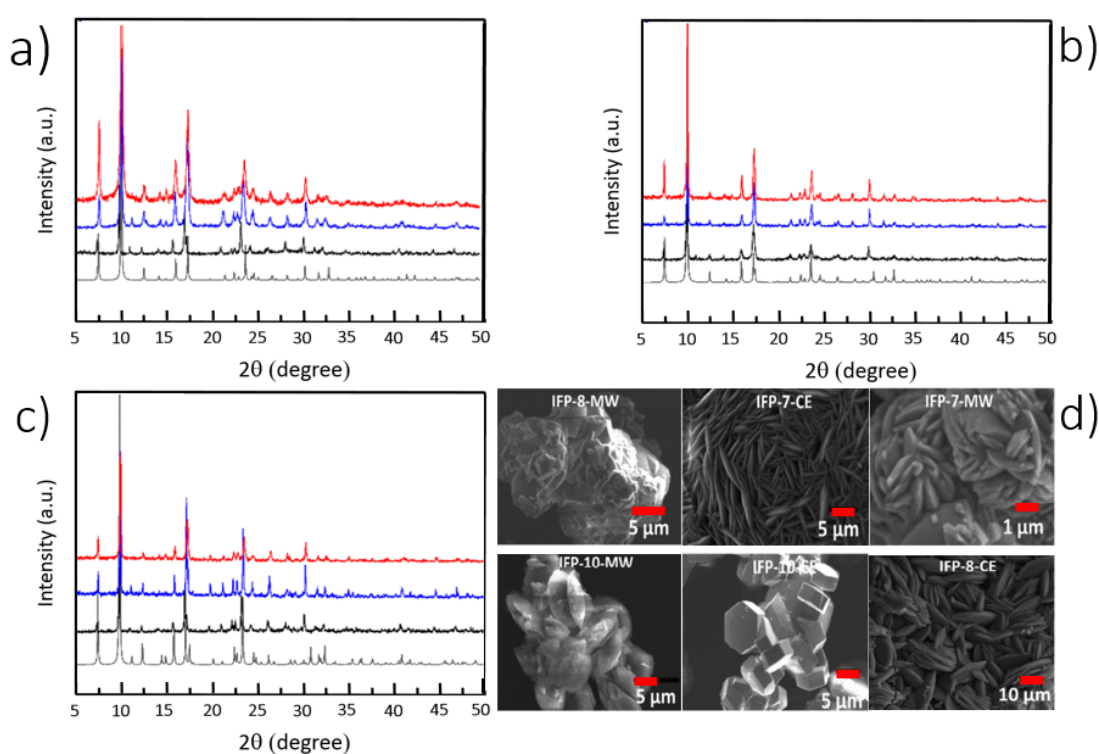
Figure 3.11: Comparison of PXRD patterns of (a) IFP-7, (b) IFP-8 and (c) IFP-10, synthesized under CE- and MW-assisted conditions (gray: simulated; black: as-synthesized under CE-conditions; blue: as-synthesized under MW-conditions and red: activated under MW-conditions), d) SEM images of IFP-7, -8, and 10, synthesized under CE- and MW-assisted conditions.

tivated by degassing at 473 K under high vacuum (10^{-3} mbar) for 24 h, prior to gas sorption measurements. PXRD patterns of activated materials exhibit diffraction peaks similar to those of the as-synthesized sample (figure 3.11). This indicates that the porous framework maintained the crystalline integrity after activation.

3.5.2.2 Gas sorption and separation

N_2 isotherms were obtained at 77 K up to a relative pressure p/p_0 of 0.995. The IFP pore aperture is too narrow for N_2 adsorption at 77 K. At cryogenic temperature diffusion of N_2 molecules into small micropores is very slow. This diffusion limitation at 77 K influences N_2 adsorption in ultramicropores (pores smaller than 7 Å) so that N_2 probably does not probe the 0.2 nm (2 Å) channels. The very low specific surface area of IFPs, synthesized under MW-assisted conditions, corresponds essentially to the outer surface of a powdery material and is comparable to the materials formed under CE conditions (table 3.3).

At pore sizes close to the kinetic diameter of N_2 ($\sim$3.64 Å), the diffusion limitation at 77 K can be alleviated by the use of CO_2 (kinetic diameter 3.30 Å) as an adsorbate at 273 K which ensures faster equilibration [163, 180]. The IFP pore aperture is too narrow for N_2 adsorption at 77 K. The saturation pressure of CO_2 at 273 K is $\sim$ 26141 Torr (34767 mbar) and low relative pressure measurements necessary for micropore analysis are achieved in the range of moderate absolute pressures (1–$\sim$1011 mbar). The advantages of CO_2 adsorption at 273 K versus N_2 adsorption at 77 K are faster analysis, greater confidence that measured adsorption points are equilibrated (both due to higher diffusion rates) and adsorption onto pores of smaller sizes that are accessible to CO_2 molecules but not to N_2.

Results of the CO_2 sorption measurements of IFP-7-MW at 273 and 298 K are shown in table 3.3. The uptake of CO_2 by IFP-7-MW at 273 K and 1 bar is 67.6 cm^3 g^{-1} which is higher than the previously reported IFP-7-CE, synthesized under CE-conditions (figure 3.12 and table 3.3). A pronounced increase in the CO_2 uptake takes place in the low-pressure region at 273 K with a small hysteresis in the desorption branch. Similarly, a high CH_4 uptake is given for IFP-7-MW compared to IFP-7-CE (figure 3.12). H_2 sorption of IFP-7-MW is nearly 2.5 times higher than that of IFP-7-CE but exhibiting a very broad hysteresis of type H2 with a steep desorption branch. The broad hysteresis is common for the MOFs with very narrow pores and/or flexible substituents [170] and is similar to IFP-7-CE (figure 3.12) [177]. These hysteresis loops of type H2 (shown in H_2 sorption isotherms) mean complex pore structures in which network effects are important. The very steep desorption branch, which is a characteristic feature of H_2(a) loops, would mean either pore-blocking/percolation in a narrow range of pore necks or cavitation [183]. The same broad hysteresis was observed for IFP-7-CE (figure 3.12, right). As an attempt to figure out the reason of the broad hysteresis of H_2, the measurement time was increased up to 50s (to increase the equilibration interval between measurements) but it showed an unaffected trend of the hysteresis (see supporting info. of [179]). This means that

Table 3.3: Adsorbed gas volumes in activated IFP-n-MW at 1 bar, in comparison with the gas sorption data of IFP-n-CE

IFP-n	Channel diameter[a] nm	Void space[b] %	S_{BET}^c m^2	V_{CO_2} cm^3 g^{-1} 273K	V_{CO_2} cm^3 g^{-1} 298k	Micropore volume[d] cm^3 g^{-1}	V_{H_2} cm^3 g^{-1} 273K	V_{CH_4} cm^3 g^{-1} 273K
7-CE[e]	0.21	34.0	3.0	57.0	40.0	0.096	50.3	17.0
7-MW			4.0	67.6	43.8	0.147	124.9	26.3
8-CE[f]	0.22	36.0	9.0	37.6	27.0	0.056	9.3	8.0
8-MW			10.0	80.9	53.9	0.148	112.7	34.9
10-CE[g]	0.3	26.0	13.0	39.0	32.0	0.052	4.4	6.0
10-MW			28.0	52.6	34.5	0.092	12.5	7.4

[a]By considering the van der Waals radii, the accessible channel diameter; [b]Potential solvent area ca-
lculated by PLATON; [c]A surface area below 20-30 m^2 g^{-1} is essentially the outer surface area of a powder; [d]CO$_2$-accessible micropore volume; [e] Ref. [177]; [f] Ref. [181]; [g] Ref. [182].
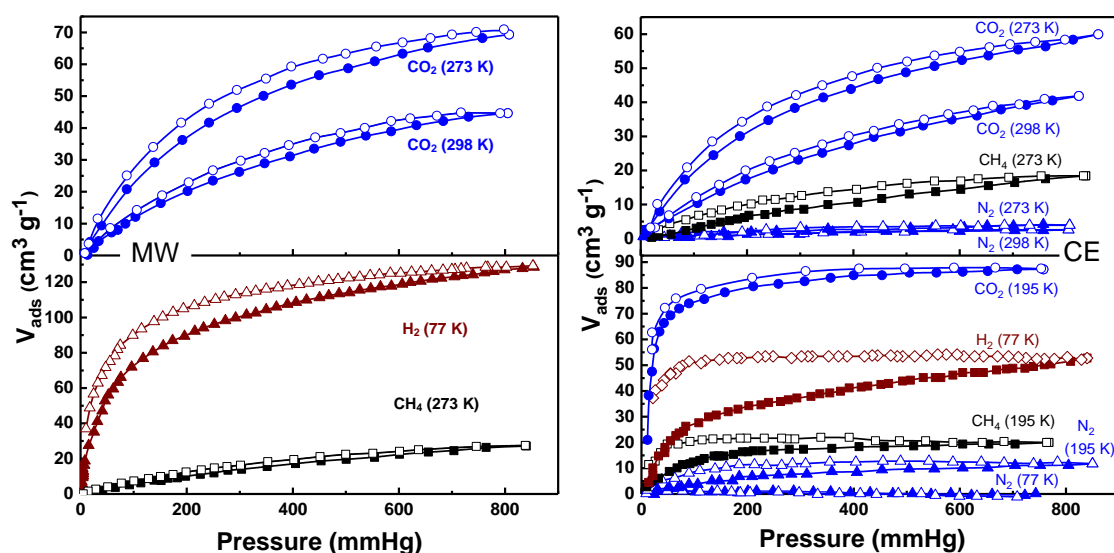
Figure 3.12: Gas sorption isotherms for activated IFP-7 of CO$_2$, N$_2$, H$_2$, and CH$_4$. Adsorption and desorption branches are indicated by closed and open symbols, respectively.

the broad hysteresis is not a question of the equilibration interval between measurements. Consequently, a comparison of the H$_2$ desorption behavior with that of IFP-1 (no hysteresis), which is isostructural to IFP-7 but with a methyl group instead of a methoxy group, is seen as further strong evidence of the flexibility of the methoxy group and its action in the gate opening behavior of IFP-7-CE (see supporting info. of [179]). Also, as stated in part 3.3.4.2, the adsorption enthalpy increases with the adsorbed amount of CO$_2$ which made the interpretation of the broad hysteresis hard.

Co-based IFP-8-MW exhibits a much higher CO$_2$ uptake than the CE material

with a disappearance of the hysteretic desorption (figure 3.13). A similar result was observed for CH_4 uptake (figure 3.13). Exceptionally, the H_2 uptake capacity (at 77 K) of IFP-8-MW (figure 3.13 and table 3.3) is 12 times higher (112.7 cm^3 g^{-1}) than IFP-8-CE (figure 3.12) with a very broad desorption hysteresis as noted and explained above for the IFP-7 materials (the slightly higher H_2 amount upon desorption is an artefact of a somewhat too low equilibration time of 20 seconds per data point). The adsorption at higher relative pressure is irre-
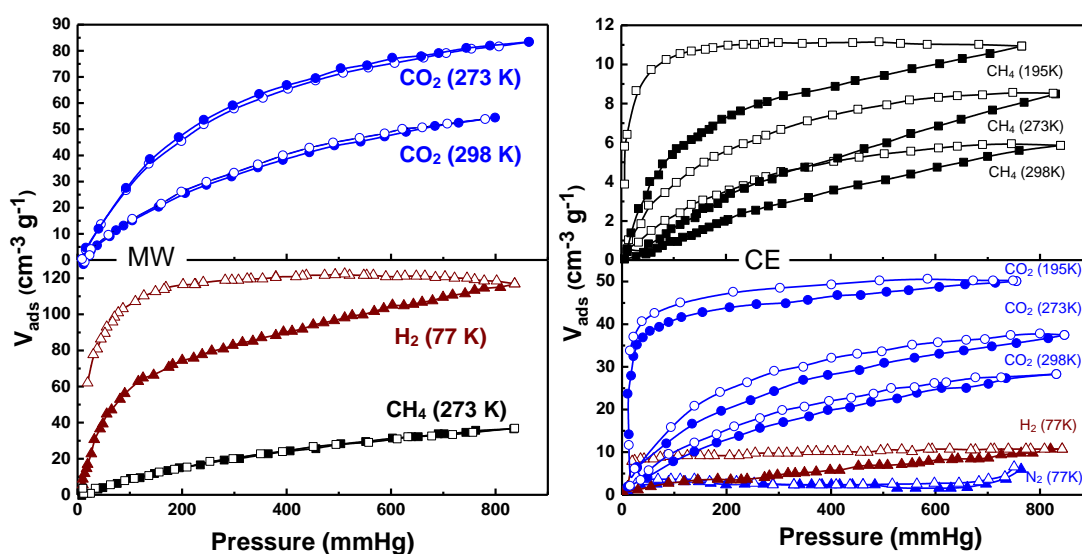
Figure 3.13: Adsorption-desorption curves for activated IFP-8 of CO_2, N_2, H_2, and CH_4. Adsorption and desorption branches are indicated by closed and open symbols, respectively.

versible due to small pore openings, which gives rise to an open loop hysteresis (figure 3.13). The smaller H_2 molecule can pass through the gates formed from the methoxy groups. The sorption isotherms can deviate from ideal equilibrium experiments as pronounced kinetic effects occur because of the small channel size and the gate effect. In figure 3.13, the H_2 sorption isotherm confirms that 98% of the adsorbed H_2 is trapped in the framework when the pressure is reduced from 1 bar to 0.15 bar.

IFP-10-MW also performed enhanced CO_2 and H_2 sorptions, with less pronounced CH_4 sorption than the CE-analog (figure 3.14). The hysteretic desorption behavior was observed for all gases (table 3.3).

3.5.2.3 PALS data

The goal here with using PALS is to confirm the results of gas sorption of materials synthesized via MW-assisted conditions and CE method under the same conditions. Such a study would yield a reasonable explanation of the high gas uptake of MW-assisted materials. For performing the porosimetry by PALS,
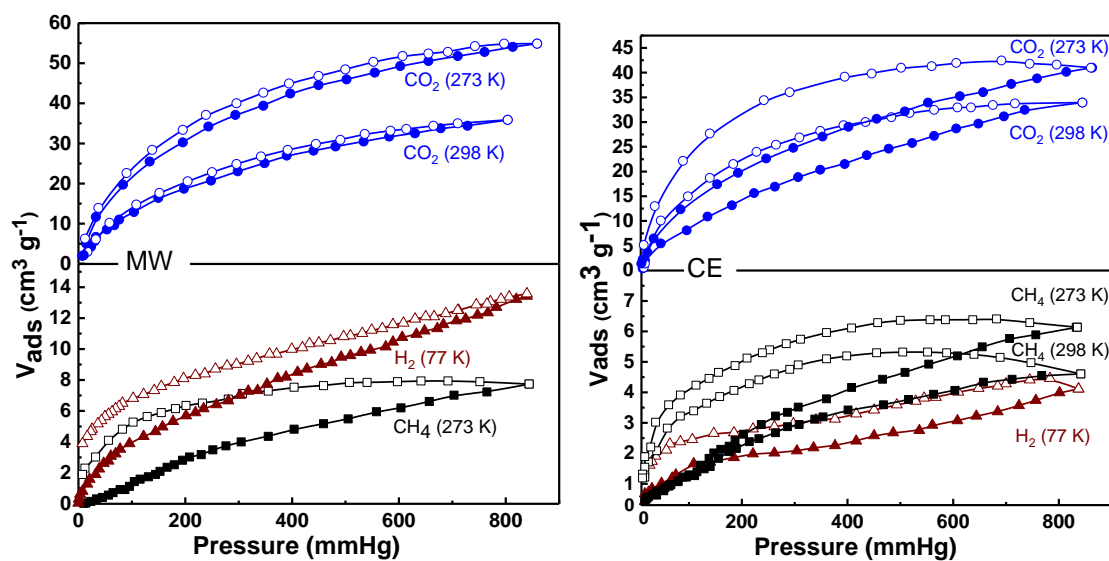
Figure 3.14: IFP-10-gas sorption isotherms of CO_2, H_2, and CH_4. Adsorption and desorption branches are indicated by closed and open symbols, respectively.

samples were activated at 473 K for 12 h to be comparable with other methods. PALS gave four positron lifetime components with the same physical meanings as in section 3.3.3 where τ_3 and τ_4 are the most important components as they reflect the o-Ps annihilation in micropores and mesopores(or defects due to de-formed linkers), respectively. PALS results reveal that micropores (determined from τ_3) of IFP-8 synthesized under CE conditions (figure 3.15.b, left) are larger than those of IFP-8 synthesized under MW-assisted conditions. IFP-8-CE micropore diameters are fluctuating around 0.6 nm during the activation periods and IFP-8-MW micropore diameters reduced from $\sim$ 0.5 nm in air at RT to $\sim$ 0.3 nm after activation at 473 K for 12 h. PALS method gave a pore diameter of 0.6 nm (with ΔR = 0.18 nm in the ETE model) for IFP-8-CE while the X-ray structure analysis gave two types of pore sizes (0.71 and 0.90 nm), considering the flexibility of the methoxy group. This conflict can be understood if the pro-cedure of pore size calculation by PALS is known. According to ETE model, o-Ps is confined in a potential well of height V and radius R (figure 2.12). In vacuum, o-Ps has its intrinsic lifetime (142 ns) but this lifetime will be reduced due to the interaction of the Ps with electrons in the wall of the potential well. When o-Ps touches the walls of the well, it will interact with a potential well of height ΔV and thickness ΔR. O-Ps annihilation occurs due to the overlap-ping between o-Ps and electron wave functions inside ΔR- thick layer. The value of ΔR is well known for porous silica (0.18–0.19 nm) [96, 153], 0.193 nm for controlled porous glass [65], and 0.166 nm for organic materials [129]. This means that ΔR is not an absolute value and it is a material-dependent fac-tor [184] which should be estimated for each material's class precisely. Since it
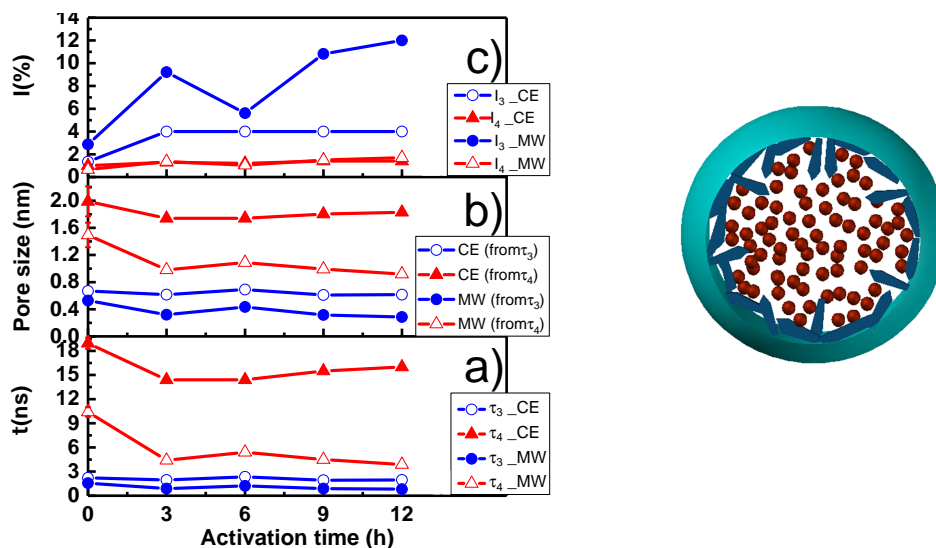
Figure 3.15: Left: effect of the activation time on a) o-Ps lifetimes, b) pore sizes, and c) o-Ps intensities of IFP-8-MW and -CE activated at 473 K for different times. The errors have the same size as the data points. Right: schematic illustrations of the existence of loosely coordinated linkers inside the pores results in an underestimation of the pore size. o-Ps between the linkers will annihilate faster than if they are not there. Red spheres are o-Ps, blue pentagonals are loosely coordinated linkers, and the open dark cyan sphere is the actual pore.

is a fitting free parameter, because it fits the electronic density in the pore wall, ΔR can be used as a surface sensitive parameter because for a certain class of materials it has a definite value. Such a value is different in the case of inner pore surface swelling with other materials having a different electronic structure from the pore wall. Shorter o-Ps lifetimes (and hence smaller pore sizes) than the expected indicate that the pore inner surface might have extra linker incorporation (figure 3.15, right) as a result of the activation which results in a faster o-Ps annihilation and an unreliable pore detection. In such a case, o-Ps will detect a narrower pore than the real one because of the presence of the extra linkers inside the pore. These extra linkers will add an extra layer to the original pore causing, on average, an irregular pore inner surface swelling. Additionally, these extra linkers would have a different (higher) electronic density than the main pore walls, resulting in an increase in the value of ΔR which could be another meaning of the shortening of the o-Ps lifetime. Such a swelling is larger in the case of IFP-8-MW than in IFP-8-CE. The confirmation of the presence of domains or regions in the inner pore wall with a different electronic structure requires a temperature dependent measurement. Unfortunately, this temperature dependent measurement needs a thermally stable material while the studied samples here are not stable with temperature. Similar findings were presented for porous polymer-silica composites [129]. As described in [179], TGA curves of IFP-8-MW showed a less weight loss (%) at 563 K compared with the ma-

terials synthesized under CE-conditions (IFP-8-CE and -8-MW: 18.6 and 13.8, respectively and IFP-7-CE and -7-MW, wt loss (%): 15.5 and 12.5 respectively; see figure B.4 in Appendix B.3.1). This result suggests that the pores were occupied with the weakly coordinated linkers which were hardly removed during a similar washing and the MW-based materials still have higher amounts of the linkers.

On the other hand, the calculated pore size from τ_4 is also larger for IFP-8-CE than IFP-8-MW and this large pore size could not be obtained from the structural model of IFP-8-CE that was constructed by single-crystal X-ray structure determination. This could probably be due to missing linker defects at a few regions of the crystal. It should be mentioned here that their intensity (which indicates their concentration) is very small ($\sim$1%, figure 3.15.c left).

After 3 h of annealing time, the small pore sizes of IFP-10- CE and IFP-10-MW are similar and negligibly reduced (figure 3.16.b). Such a nearly equal pore size of IFP-10-MW and -CE does not reflect the existence of deformed linkers inside the small pores explicitly while the higher intensity of micropores of IFP-10-MW relative to IFP-10-CE especially after 12 h of activation (4 % compared to $\sim$ 2.5 %, respectively) can explain the higher gas uptake of MW materials due to a higher micropore volume of IFP-10-MW. τ_4 of IFP-10-CE has shown always higher in size than its MW assisted material although the value is constantly reducing upon annealing time as similar with IFP-10-MW (figure 3.16.a, .b).

Micropores (from τ_3) of IFP-7-CE and -7-MW are similar after 6 h of activation, but the micropores of IFP-7-CE are still larger than those in IFP-7-MW (figure 3.17.b). On the other hand, the defect-related pores (from τ_4) are the same in both samples after 6 h of activation which are similar to the pre-activation value (figure 3.17.b). These average values of defect-related pores are scattered at 3 h of activation at larger values for IFP-7-MW and smaller values for IFP-7-CE. Surprisingly, PALS detected a fifth component after 3 h of activation for IFP-7-CE and after 6 h for IFP-7-MW as shown in figure 3.17.a. The correlated pore size of this fifth component of IFP-7-CE is increased from $\sim$ 2.7 nm after 3 h to $\sim$ 4.1 nm at 6 h then it is reduced to $\sim$ 3 nm at 9 h then it increased a little to $\sim$ 3.3 nm at 12 h. τ_5 is continuously reduced for IFP-7-MW since its first instance after 6 h from $\sim$ 3.9 to 3.3 nm after 12 h as it is clear in figure 3.17.b. Their related intensities showed a reverse behavior relative to lifetime components (figure 3.17.c). In the case of considering τ_4 as a detection of defects due to missing linkers, the presence of τ_5 in IFP-7-CE and IFP-7-MW samples would mean an agglomeration of these defects forming larger voids or mesopores. And since the formation of defects is temperature- dependent, the
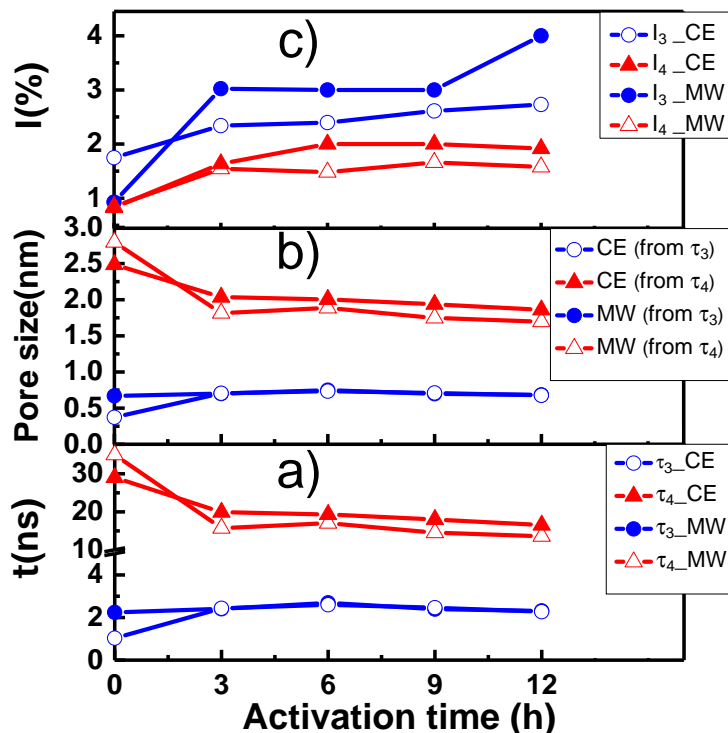
Figure 3.16: a) O-Ps lifetime, b) pore size, and c) o-Ps intensity of IFP-10-CE and -MW activated at 473 K as functions of activation time. The errors have the same size as the data points.

instability of the variation of τ_5 could be due to the irregular shape of the formed large void. Obviously, the intensities of these larger voids are not too high (I_5 in figure 3.17.c is $\sim$ 3 - 4 %). The appearance of such an agglomeration starts in sample IFP-7-CE earlier than IFP-7-MW which can be understood from the intensity of both samples (figure 3.17.c). After 3 h of IFP-7-CE activation, I_4 > I_3 which means that mesopores (defects) dominate over micropores. This suggests a higher probability of agglomeration (τ_5), while the appearance of τ_5 for IFP-7-MW is difficult to be explained in terms of intensity.

However, results revealed that there is no any indications of broadening of the reflexes in the PXRD patterns (compared to CE materials; figure 3.11) that may suggest smaller crystallites due to partly amorphous phase formation. Additionally, the characteristic type-I isotherm of the H4 type hysteresis for N_2 adsorption could prove the crystal defects due to the mesopore formation in the microporous materials. Such a defect production maybe result in the collapse of pore aperture which restricted the adsorption of N_2 at 1 bar and 77 K by the IFP materials because of activation at 473 K.
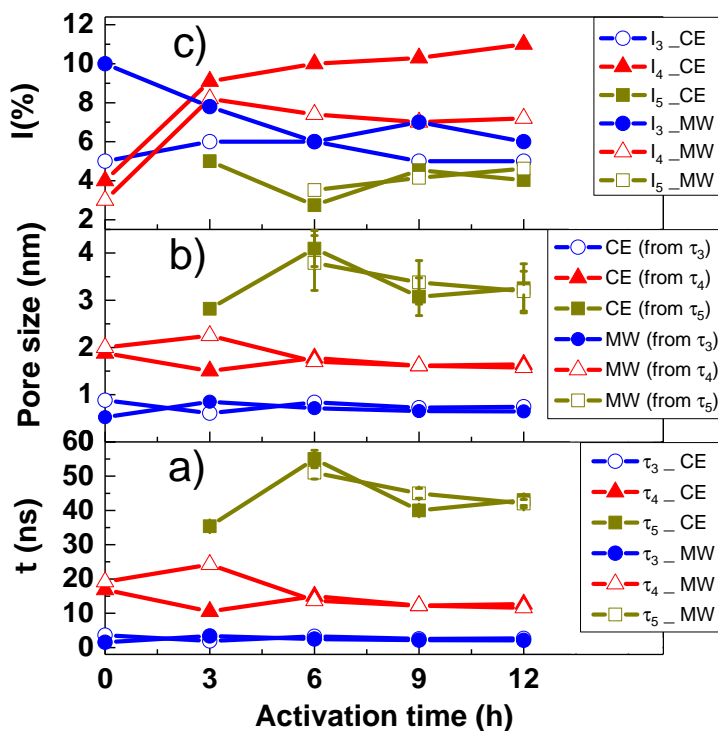
Figure 3.17: a) O-Ps lifetime, b) pore size, and c) o-Ps intensity of IFP-7-CE and -MW activated at 473 K as functions of activation time. Points without errors mean that the errors are in the same size as the points

3.5.3   Conclusions

In summary, the enhancement of gas uptake capacities of MW-assisted materials was observed, in comparison with the materials synthesized by the CE-method. Porosimetry by PALS indicated that the smaller pore sizes of MW-assisted materials than those obtained under CE-conditions could have an inherent ability to loosely coordinate hydrolysed linkers. Thus, the ultra-micropore volume (calculated by the CO_2-accessible micropore volume) for MW-assisted materials was increased. Small gas molecules could interact efficiently with the narrow sized pore walls of these ultra-micropores in MW-assisted materials, showing higher gas sorption than in CE-assisted materials.   eq25

Chapter 4

Pseudomorphic transformation of spelt husk ash, silica gel, and controlled porous glass into MCM-41

4.1   Introduction

Ordered mesoporous silica, like MCM-41, have attracted a great attention in the scientific community [185] since their synthesis for the first time in the 1990s [21]. They are suitable for several applications such as catalysis, sorption and separation technologies, chromatography [186], and in biomedical applications [187]. This versatility of applications relies on the unique features of ordered mesoporous silica as they are highly ordered with a high surface area and pore volume, their pore size is tunable (2-10 nm) [185] and can be functionalized, and they have a narrow pore size distribution which enables them to be used for large organic molecules separation [188].

Classically, mesoporous silicas are synthesized by using surfactants as templates [186] in a silica source such as silica gel [188]. Textural parameters like pore diameter, volume, and pore wall thickness depend on the used silica source, pH, temperature and duration of synthesis, and the silica-surfactant interaction [189]. Different surfactants have been used to synthesize different porous silicas with different morphologies. For example, rod-like micelle-templated silica (MTS) materials, e.g. MCM-41 and MCM-48, have been synthesized from water-alcohol systems [190] by controlled hydrolysis [191] or spray drying [192]. But with this method, a difficulty in controlling the particle morphology and size beside pore decoration was recognized [193]. Such a controlling is essential for applications like chromatography [188]. To this end, it was proposed in 2002 to transform the non-ordered porous system of silica gel having spherical particles into ordered mesoporous systems like MCM-41, -48, and -50 [188, 193]. Such a transformation allows independent optimiza-

tion of the particles and properties of MTS phase and hence, overcoming the aforementioned difficulty. This transformation process is known as *pseudomorphic* transformation and it means the maintenance of the original morphology (particle shape) of a mineral that undergoes different dissolution-precipitation reactions [194].

Pseudomorphic transformation of different silica sources like silica gels [195], controlled porous glass (CPG) [196], and biogenic silica [197] into MCM-41 has been conducted. All of these transformed systems were investigated by conventional tools of porosimetry like N_2 sorption, mercury intrusion (in case of large mesopores and macropores), and more recently by hyperpolarized ^{129}Xe NMR [194] but none of them was investigated by PALS. So, we report on the study of the pseudomorphic transformation of these systems by PALS for, to the best of our knowledge, the first time. In addition to being a powerful porosimetry technique of open pores and free volumes, PALS can detect closed porosity. It is sensitive to the electronic structure and chemical composition of inner pore surfaces, therefore, it is used here to get a deeper insight into the porous structures of the transformed samples.

This chapter is divided into two main sections; in the first section, the importance, porous structure, and transformation modes of Spelt Husk Ash (SHA) and silica gel will be addressed. The transformation of quite big pores (45 nm) of a CPG sample into MCM-41 is discussed in the second section.

4.2   From totally disordered porous silica-based materials to well ordered mesoporous silica

4.2.1   Biogenic silica

Production of MTS members requires a commercial silica source, to form the backbone of the mesoporous silicas, solvent, and a mineralized agent [198]. Fortunately, the cost of such a production can be lowered once a low-cost and abundant silica source like biomass is used. The raw material of the rice husk (RH) contains 12-18 wt% of silica [199]. It was found that the burning of pre-leached RH yields an amorphous silica-rich Rice Husk Ash (RHA) containing about 97.7 wt% silica [197]. So, silica extraction from RH is a good example of exploiting the natural resources and it adds economic and environmental values to RH as a cheap silica source.

The idea of pseudomorphic transformation of RHA into MCM-41 and MCM-48 (only from preformed MCM-41 not from RHA directly) was described for the first time in [197] where Egyptian RH was used. Type IV(a) (figure 1.8)

isotherm with a very broad pore size distribution of meso and macropores was obtained for the RHA starting material [199]. During pseudomorphic transformation, the slope of the sorption isotherm was increasing which indicates the formation of mesoporosity at the cost of the existent porosity in the starting material. The methodologies and outputs of this study [197] will be our guide for the transformation and interpretation of our sample which will be studied by PALS.

In this section, different biomasses are characterized by PALS and N_2 sorption to test the degree of their agreement of detecting the porous structure of these different biomasses after leaching and burning. Afterwards, only one system (G-SHA) is chosen for performing the pseudomorphic transformation process.

4.2.1.1 Experimental details

Materials: Four different plant biomasses from different origins were used in this study: horsetail ash (HTA), rice husk ash (RHA), spelt husk ash (SHA), and oat husk ash (OHA). Only the spelt husk sample was transformed into MCM-41 by pseudomorphic transformation process. The preparation of all samples and the transformation were done by the group of Prof. Enke, Leipzig University and the exact procedure is given in Appendix C.1.

N_2 **sorption**: Prior to nitrogen adsorption (ASAP 2000, Micromeritics, Norcross, GA, USA) measurements, the samples were degassed under vacuum at 523 K for 12 hours. The total pore volume was calculated at $p/p_0 = 0.995$ and the specific surface area was determined using the BET model in a pressure range of $p/p0 = 0.05$-0.30. The PSD was calculated by the non-local density functional theory in equilibrium (NLDFT) using the kernel of the software Quantachrome ASiQwin. The MCM-41 pore volume was determined using the t-plot method for statistical thicknesses t = 0.8-1.6 nm using the software Quantachrome ASiQwin. The approximated degree of transformation (DT) was calculated by dividing the MCM-41 pore volume by the initial pore volume.

PALS measurements: About 0.4 ml of powder samples surrounding a ^{22}Na source of ~ 3 μ Ci was put between two Hamamatsu PMTs, containing two 50 mm$\times$ 50 mm EJ232 plastic scintillators, connected to a digital PALS consists of an 8-bit digitizer (DC211) and custom-made dual high-voltage and coincidence units. The maximum time interval between signals from the detectors was set in the software to 1.1 μs (1 μs as a coincidence value and 0.1 μs as a delay due to cables and data transfer) with 100 ps channel width. With this setup, the obtained count rate was ~ 220 cps and the timing resolution was ~ 300 ps FWHM. Initially, all samples were measured as received in air, then they were annealed at 473K for 5h to remove water and moisture adsorbed on

the surface of the pores, and finally, they were measured at RT with 30 million counts statistics to minimize the statistical dispersion of MELT results, which is susceptible to it due to many freedom degrees in its calculations. Data resolving by MELT gave six and seven lifetime components with the following values and meanings; four short lifetimes of 0.12-0.2 ns, 0.4-0.5 ns, 1.2-2.2 ns, and 4-5 ns originate from the annihilation of p-Ps, free e^+, o-Ps in the matrix of the material, and o-Ps in small micropores (0.92 nm-1.02 nm in diameter), respectively. Additionally, German-SHA and Italy-RHA samples showed three long-lived o-Ps lifetime components while the other samples showed only two long-lived components due to o-Ps annihilation in different micro and mesopores. Only the o-Ps lifetime components will be considered in this discussions due to their link to pores and free volumes.

4.2.1.2   Results and discussions

Different biogenic silica sources

A-Gas sorption

Results of sample G-SHA is presented in the next section in the course of the pseudomorphic transformation process.

As discussed in [199], Nitrogen sorption isotherms of the different biogenic silica sources (figure 4.1.a) show type IV(a) isotherms indicating the presence of broad PSD of mesopores. The textural properties of the investigated samples are given in table 4.1. The PSD in figure 4.1.b shows that all samples have a broad PSD of mesopores which is centered at around 5 nm in all samples except for the G-HTA which has a peak at 6 nm and also it has the highest pore volume and BET surface area(table 4.1). No indication of the existence of micropores and the unsaturated isotherms would mean that the samples have also macropores but N_2 could not reflect theses pores.

Table 4.1: Textural properties of different biogenic silica samples given by N_2 sorption

Property	G-HTA	V-RHA	I-RHA	G-SHA	C-RHA	G-OHA
S_{BET} (m^{2}g^{-1})	392	313	272	150	251	210
V_P (cm^{3}g^{-1})	0.54	0.39	0.35	0.35	0.34	0.35
Average D (nm)	6.0	5.0	5.0	5.0	4.9	5.0

B-PALS results

In order to verify the findings of gas sorption measurements, it was important to get PSD from PALS to compare them. For doing so, the procedure was to use the MELT routine [91] which gives the lifetime distribution (distribution of an intensity over positron lifetime depending on the quantified maximum entropy of lifetime) without any pre-assumed number or shape of components (figure

Figure 4.1: a) Nitrogen sorption isotherm (solid symbols represent adsorption and open symbols represent desorption) and b) PSD of of different biogenic silica samples.

4.2.a). Then to correlate the obtained lifetimes to pore sizes using the ETE model [99] by EELViS code [153]. Finally, to correlate the intensity to the pore volume (V) per unit pore size (D) using the following expression [200]:

$$\frac{dV}{dlogD} \propto \frac{dI}{dD} = \frac{dI}{d\tau}\frac{d\tau}{dD} \tag{4.1}$$

where $\frac{dI}{d\tau}$ is the intensity distributed over lifetimes (obtained from MELT) and $\frac{d\tau}{dD}$ is the first derivative of the relation $\tau(D)$ given by the ETE model.

Converting the Ps lifetime distribution (figure 4.2.a) into PSD (figure 4.2.b) shows that all samples contain micropores with diameters of 1.4-1.9 nm in addition to smaller micropores in the range of 0.92-1.02 nm (correspond to 4-5 ns) which may be due to the annihilation in free volumes in the solid part of the materials. On the other hand, by comparing PALS and N_2 sorption results, it is clearly seen that PALS overestimates the size of the large pores (centered at 7-10 nm in comparison with 5-6 nm of N_2 sorption). Also for all samples, except for the G-SHA sample, the PSDs given by PALS are narrower than those obtained by N_2 sorption. This would mean that these large pores are interconnected together and once Ps enters these large pores it tends to stay and annihilate in the widest available part of the pores. Therefore, PALS has shifted the peak of the PSD to higher pore diameters. Also, the width of the PSD may reflect the degree of connectivity of these large pores because the poor connectivity will prevent Ps to travel over different pores which means in this case that PALS will exhibit the actual PSD. Thus, it is expected that the G-SHA sample has the worst connectivity between its large pores while the V-RHA has the best con-
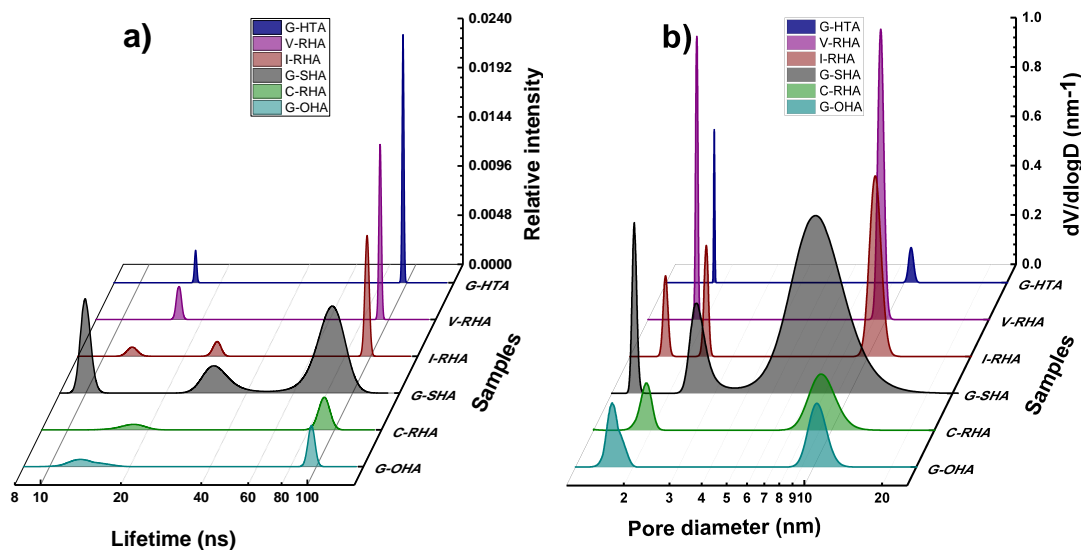
Figure 4.2: (colors on axes) Conversion of a) o-Ps lifetime distribution given by MELT into b) PSD (based on [200]) of different biogenic silica silica samples.

nectivity. It should be mentioned here that PALS did not show any signals of the annihilation in very large mesopores or even macropores because if there are large mesopores or macropores PALS would give its lifetime in vacuum (142 ns). Of course, PALS sensitivity will be not good but at least the detection of the 142 ns will reflect the presence of very large pores.

Despite the differences between PALS results and N_2 sorption ones, it can be seen that all samples have nearly the same accessible porous structures (in the valid range of both tools) although the samples are different.

German-spelt husk ash sample and its pseudomorphic transformation

A-Gas sorption

The nitrogen sorption isotherm of the starting material (G-SHA) and its transformed products is shown in figure 4.3.a. It is clear that the isotherm shape of G-SHA sample is type IV(a) isotherm indicating a complex porous structure with a very broad PSD covering a wide range of mesopores and reaching macropores (not shown). This complexity disappeared by transforming the starting material as the slope of isotherm was increased with transformation with a step appearance at 0.4 relative pressure which means the success in creating monomodal mesoporosity due to MCM-41 with a nearly complete disappearance of larger meso or macroporosity. Clearly, the isotherm shape of the 50% transformed sample (the blue starts is figure 4.3.a) differs from type IV and it shows type I(b). This anomalous trend (owing to the disappearance of Type IV isotherm) could be an indication of surfaces roughening. This roughening is caused by the high concentration of the added NaOH and it could be pore fragments were produced as a lot of SiO_2 was dissolved by NaOH but could not be ordered around

the micelles as there were too little surfactants present. In this case, only un-ordered pores are obtained resulting in a shrinking in the pore size. The textural properties of these samples are shown in table 4.2. PSD of all samples is shown in figure 4.3.b and it shows that G-SHA sample has mesopores with a broad distribution centered around 4.9 nm without any indication of microporosity. In the case of the 10 % transformed sample, this broad PSD was transformed

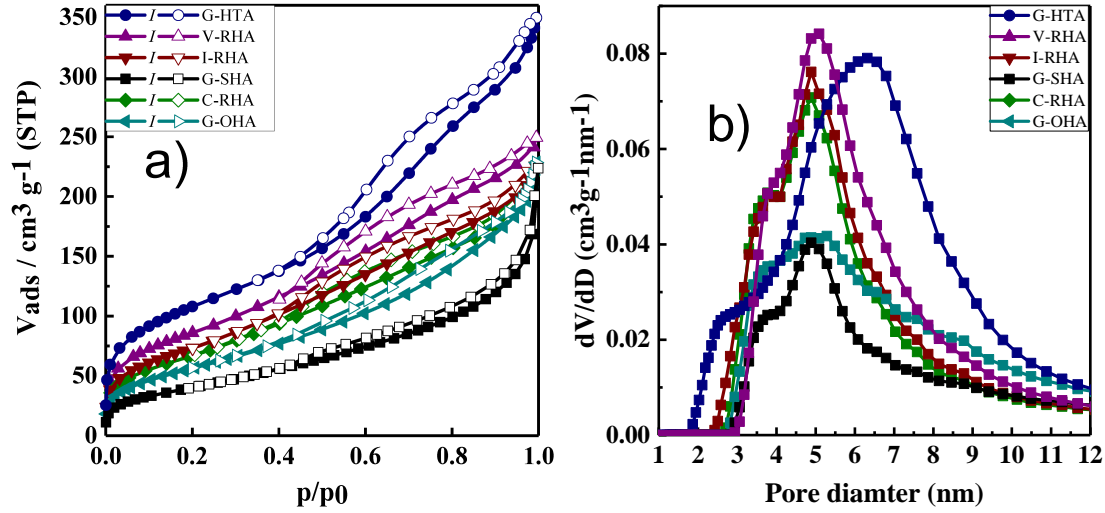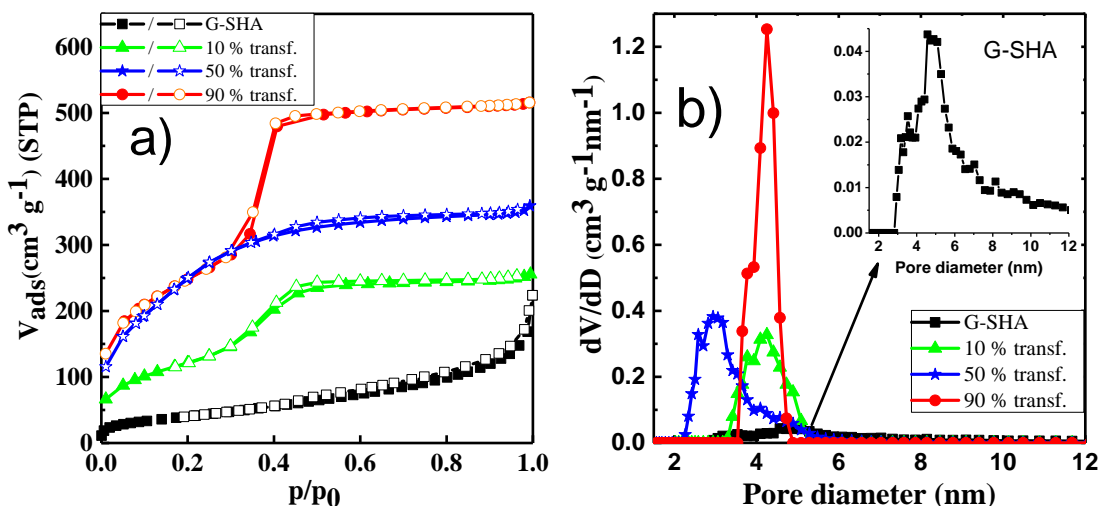

Figure 4.3: a) Nitrogen sorption isotherm (solid symbols represent adsorption and open symbols represent desorption) and b) PSD of G-SHA and its transformed products.

into that MCM-41 of $\sim$ 4.2 nm with $\sim$ 2.5 nm broadening. A shrinkage in the transformed pore has been observed for the 50 % transformed sample as it has a pore diameter of $\sim$ 2.9 nm. This reduction in the expected pore size ($\sim$ 4 nm) could be due to the formation of pore fragments as discussed for the isotherm. A

Table 4.2: Gas sorption data of G-SHA and transformed samples.

	Transformation degree (%)			
	0	10	50	90
S_{BET} (m^{2}g^{-1})	150	446	1001	896
V_P (cm^{3}g^{-1})	0.35	0.40	0.56	0.80
V_{MCM-41} (cm^{3}g^{-1})	0.00	0.36	0.51	0.77
D_{peak} (nm)	4.90	4.20	2.90	4.30

high-quality MCM-41 sample was formed with a narrow PSD and pore size of 4.3 nm was obtained for the 90% transformed sample which means a success of transforming a totally disordered porous silica into a well-ordered mesoporous silica.

B-PALS

PSD of the starting (reference) material and transformed ones given by PALS using MELT is depicted in figure 4.4.b. By looking at the PSD of G-SHA sam-
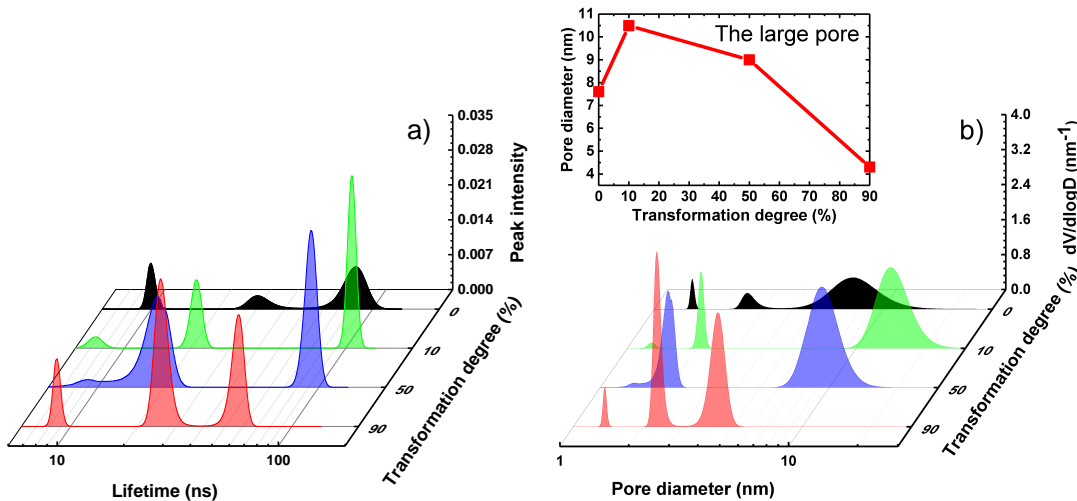
Figure 4.4: (colors on axes) a) o-Ps lifetime distribution given by MELT and b) PSD of G-SHA and transformed samples based on [200].

ple (the black area denoted by 0% transformation), it is obvious that this material contains complex micro and mesopore sizes of 1.4, 2.5, and 7.6 nm (in addition to ~ 0.92 nm small micropores, not shown) assuming spherical pore shape. This result brings two discrepancies between PALS and N_2 sorption; the first one is the disability of N_2 sorption to detect the 0.92, 1.4, 2.5 nm pores detected by PALS. Such a conflict would suggest that these pores are closed and they are not accessible by N_2 while Ps can penetrate to them hence, this is a good example validating an important feature of PALS which is *all free volumes and pores can be probed whatever their accessibility*. The second discrepancy is that the large mesopore detected by N_2 sorption is ~ 4.9 nm while PALS detected a PSD centered at ~ 7.6 nm in diameter while both methods showed a broad PSD of this pore starting from ~ 4 nm. The reason for such a mismatching is not clear but as PALS has realized closed porosity in this sample so, it could be that this sample contains some closed porosities with a mean pore diameter > 4.9 nm. These closed porosities could be there either due to; (a) formation of connected domains between the 4.9 nm pores (detected by N_2 sorption) and some small mesopores (2.5 nm) or (b) overlapping of some 4.9 nm pores together (figure 4.5). Both possibilities would shift the 4.9 nm towards bigger pore size. Even if one excludes the possibility of forming closed porosity as the leaching process should leave behind accessible pores (the large pores), this misfit could be discussed in a different way. Since N_2 sorption shows a broad PSD starting from 3 nm up till pores > 12 nm so, such a shift in the mean PSD, given by PALS, would mean simply that pores having sizes close to 7.6 nm dominate over the other pores in this distribution or pores in the range 4.9-7.6 nm are accessible together and o-Ps prefers to stay in the largest pores (7.6 nm). Another problem
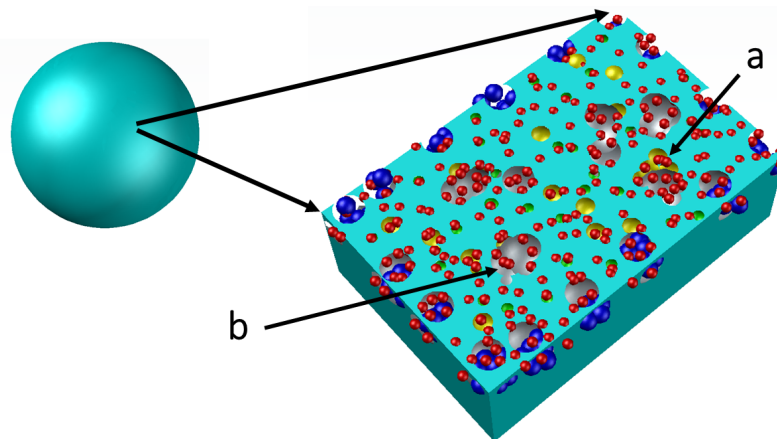
Figure 4.5: Possible explanation of the porous structure of G-SHA sample from PALS results. Big cyan sphere, the original particle; grey spheres, large mesopores; yellow spheres, small mesopores; green spheres, micropores; blue spheres, Nitrogen; red spheres, Ps.

appears in the 10 and 50 % transformed samples when comparing PSD given by PALS and N_2 sorption. N_2 sorption shows that the largest mesopore (4.9 nm) is not there anymore in these two samples and they have only pores with 4.2 and 2.9 nm in diameters, respectively. In contrast, PALS showed that the 7.6 nm and the 2.5 nm pores of the starting material were changed into 10.5 nm (figure 4.4.b, inset) and 2.1 nm, respectively, in the 10 % transformed sample. Similarly, the 9 nm (figure 4.4.b, inset) and the $\sim$ 2 nm pores were obtained for the 50 % sample. This disagreement between PALS and N_2 sorption can be explained as follows: starting from 10 % transformation degree, the MCM-41 phase is formed in the sample (shown in the sorption isotherm, figure 4.3.a) and this MCM-41 is accessible to a remaining porosity in the starting material (cannot be detected by N_2 sorption). This remaining porosity is caused by either free spaces between grains due to poor long-range order [188] or by an increase in the original pore size of the starting material due to the hydrothermal treatment of the starting material [133]. The existence of such large pores or free spaces accessible from the formed MCM-41 would result in an escape or migration of Ps from the MCM-41 into these larger volumes. Such an escape can be considered as an additional annihilation rate of Ps, $\lambda_{total} = \lambda_{MCM-41} + \lambda_{escape}$, ($\lambda$ is the annihilation rate) which means a decrease in the lifetime in MCM-41 pores, τ_{MCM-41}, (τ_{MCM-41} is the reciprocal of λ_{MCM-41}) and hence, an underestimation of their sizes (from 3.6 nm to 2.1 nm in the 10 % transformed sample and from 2.6 nm to 2 nm in the 50 % transformed sample). Again, the pore size reduction of the 50 % transformed sample might be due to the formation of pore fragments (as discussed in section 4.2.1.2). To verify the idea of Ps migration from MCM-41 pores, a comparison between PSD given by PALS and N_2

sorption of a high-quality and pure MCM-41 sample (synthesized at Hamburg University), with the same pore size as expected for the transformed samples, has been made. In figure 4.6, N_2 sorption shows that the sample has a narrow PSD centered around 4.3 nm while PALS shows two distributions centered around 2.1 nm and $\sim$ 11 nm. The 11 nm signal has no meaning as a pore from
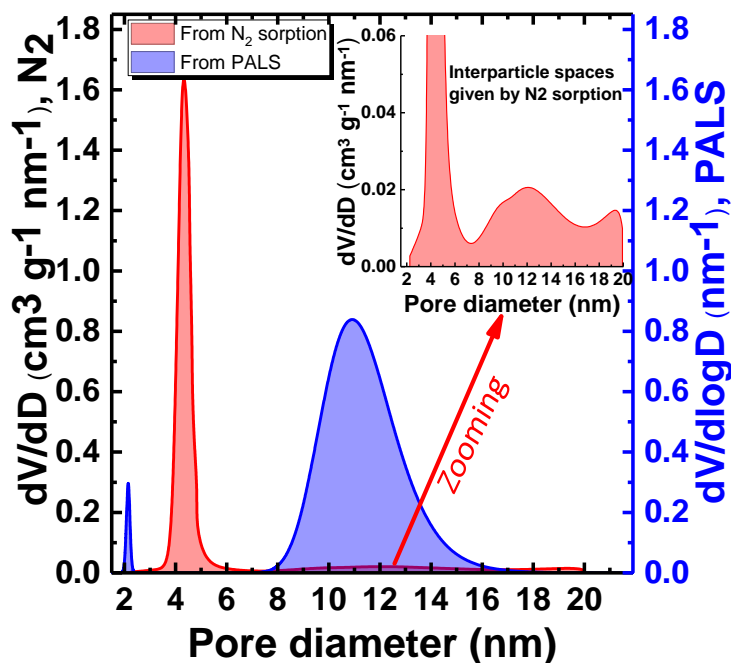
Figure 4.6: Comparison between PSD given by PALS (the light blue distributions) and N_2 sorption (the light red distribution) of a pure MCM-41 with small particle size

expectation's and N_2 sorption's point of view (or the pores of size greater than 8 nm would be in the great minority in PSD from LN2). The only explanation here is that this distribution corresponds to Ps migration from MCM-41 pores into interparticle spaces because of the small particle size ($\sim$ 0.2-0.3 μm) which is less than the 0.56 μm diffusion length of Ps in MCM-41 [201]. Such a migration has caused underestimation of MCM-41 pores from 4.3 nm to 2.1 nm. The accuracy of determining this interparticle spaces by N_2 sorption is very small due to their negligible pore volume (figure 4.6, inset). A similar discussion has been made by Zaleski et al. [202] for Ps migration from MCM-41 pores into larger spaces (interparticle spaces). These findings confirm the argumentation that the "apparent" pore shrinkage seen by PALS for the 10 % transformed sample (because the pore reduction in the 50 % would be due to the formation of pore fragments) is mainly due to o-Ps escape from MCM-41 into the remaining porosity of the original pore.

Surprisingly, sample transformed for 90 % exhibits a narrow pore with a mean

pore diameter of 4.3 nm which is the exact pore size detected by N_2 sorption experiment. This means that the remaining porosity seen in 10 % and 50 % transformed samples disappeared in the 90 % sample due to the production of a high-quality MCM-41 sample. Nevertheless, this sample still has the 0.92, 1.4, and 2.5 nm pores. The presence of these pores in all samples without any changes in their sizes (except a slight reduction in the 1.4 and 2.5 nm pores in the 10 % and 50 % samples due to overlapping with the MCM-41 affected pores) means that they are not affected by the transformation, only changes in their concentrations have been observed.

4.2.1.3 Conclusions

This study shows a successful way of getting porous silica from biomasses and the ability to transform the disordered porous structure of these biomasses (like spelt husk ash) into the well-ordered mesoporous structure of MCM-41 by employing pseudomorphic transformation. PALS has been conducted to study the pseudomorphic transformation of biomass samples due to its sensitivity to open and closed porosity. PALS revealed that the starting materials contain closed micro and mesoporosity and the presence of interconnected pore domains could be possible. Also, it showed that the closed porosity is not affected by the transformation with a change in their concentration. Finally, a perfect agreement was observed between PALS and N_2 for MCM-41 detection (90 % volumetric transformation) as both techniques showed a narrow PSD and 4.3 nm pore diameter. Thus, the usage of the discussed procedure of transforming a highly disordered husk ash into well-ordered MCM-41 is recommended.

4.2.2 Silica gel

4.2.2.1 Introduction

As discussed in section 4.1, the control of the particle shape and morphology of MTS is crucial in various applications. Such a control was accomplished by carrying out the pseudomorphic transformation introduced by Galarneau et al. using silica gel as starting materials [188]. This is because pseudomorphic transformation means transforming the pore walls of the starting material into a newly introduced porosity with preserving the original macroscopic particle shape. The mechanism of the pseudomorphic transformation is the locally restricted dissolution of the silica from the backbone of the starting materials (by the alkaline conditions) and its precipitation (self-assembly) around a surfactant to template MTS materials. With equal rates of dissolution and precipitation,

the initial morphology is maintained [203].

In the seminal paper of pseudomorphic transformation, silica gel (Lichrospher 100) was stirred in an alkaline solution with cetyltrimethylammonium bromide (CTAB) and NaOH having the following molar composition: 1 SiO_2 / 0.25 NaOH/0.1 CTAB/20 H_2O [188]. The presence of NaOH affects the surface charge of the silica particles and the produced MCM-41 will be more hydrothermally stable when there is no Na in its structure [196, 204]. Consequently, a modified approach was introduced by Enke et al. where the bromide anion of the CTAB surfactant was replaced with hydroxide anions forming cetyltrimethylammoniumhydroxide (CTAOH) [193, 196]. The formed CTAOH molecules are considered bi-functional templates as they can perform both the dissolution and templating processes.

A silica gel sample with 6 nm in diameter (Lichrospher 60) with spherical particle shape was studied in [193]. This study has revealed interesting findings due to the use of CTAOH where a narrower PSD with a slight enhancement of the pore volume was obtained as well as a complete transformation occurred only after one day in comparison with several days required with CTABr. These interesting results were obtained by characterizing the samples with low-temperature N_2 sorption and Pulsed-field gradient nuclear magnetic resonance (PFG-NMR) spectroscopy.

Other interesting findings regarding the porous structure during the evolution of pseudomorphic transformation would be obtained by undertaking PALS measurements. A comparison between the PSD of the parent and transformed samples derived from PALS and N_2 will help for the understanding of this system. Additionally, it can validate the ability of PALS to distinguish between pores in systems having pore diameters closed to each other.

4.2.2.2   Experimental details

The procedure of samples' preparation is described in Appendix C.2.
Nitrogen physisorption isotherms were measured with a Micromeritics®ASAP 2010 and Quantachrome® Autosorb iQ after sample pretreatment in vacuum for 10 h at 523 K. Specific surface areas were calculated using the B.E.T. method, the total pore volume was obtained at $p/p_0 \approx 0.99$. Pore size distribution curves were calculated from the adsorption branch of the isotherm on the basis of the NLDFT method. The mesopore volume of the MCM-41 phase was determined by the t-plot method in the range of 0.6–0.9 p/p_0.

The experimental details of PALS measurements are the same as described in section 4.2.1.1. The studying systems are a starting silica gel sample (0%) and four pseudomorphic transformed samples (25, 50, 75, 100 % transformation

degrees). The different degrees of transformation were obtained by using different amounts of CTAOH vary from 0-42 ml g^{-1} to control the pore volumes the MCM-41 pore in relation to the starting material pore volume.

4.2.2.3   Results and discussions

The N$_2$ sorption isotherms and textural properties of the parent silica gel sample and the products with different degrees of transformation are shown in figure 4.7 and table 4.3, respectively. The isotherm of the parent sample (0% transf.) exhibits a typical IV isotherm for mesopores having a broad PSD. In the region of relative pressure of about 0.37-0.4 in the sample with 25 % transformation, a fast increase in the isotherm is observed which means the formation of MCM-41 [188].   This MCM-41 formation caused a decrease in the pore volume of
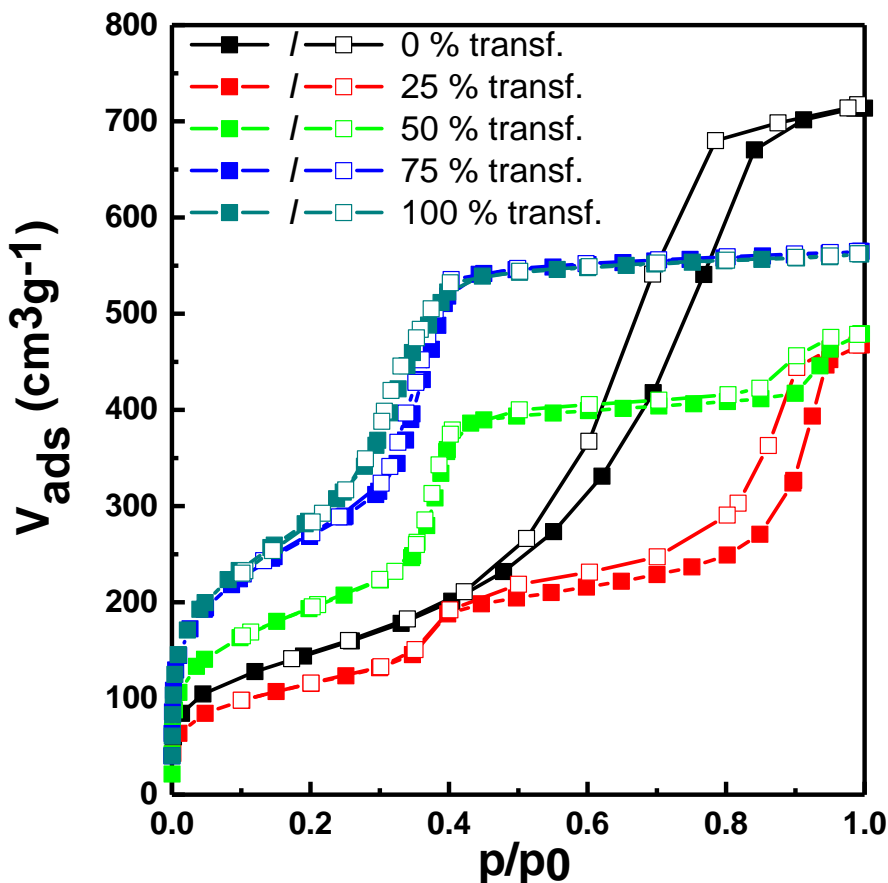
Figure 4.7: Nitrogen desorption isotherms at 77 K of 6 nm pores of a silica-gel and its pseudo-morphic transformed products.

the initial pores in the silica gel. The pore volume of the formed MCM-41 is further increased in the sample with 50 % transformation and the hysteresis of the parent sample delayed and appeared in the 0.8-0.9 relative pressure range. This hysteresis indicates a small pore volume of a remaining porosity of a small

Table 4.3: Textural properties of the silica gel sample and transformation products

Property	Transformation degree (%)				
	0	25	50	75	100
S_{BET} (m^2g^{-1})	533	411	695	981	1085
V_P (cm^3g^{-1})	1.18	0.51	0.15	0.05	0.05
V_{MCM-41} (cm^3g^{-1})	——	0.2	0.62	0.83	0.82
d_P (nm)	7	——	——	——	——
d_{MCM-41} (nm)	——	4.2	4.2	4.1	3.8

amount of the initial large mesopores. In the case of the samples with 75 % and 100 % transformation degree, the isotherms show that the initial mesopores have completely disappeared and pure MCM-41 pores have been formed. From the PSD given by N_2 and evaluated by the DFT method (figure 4.8, left) shows that the parent sample (denoted by 0 %) has a broad PSD solely with 7 nm in the peak. PSD of the sample with 25 % transformation shows that the mesopore of the parent sample has a very small pore volume due to the formation of the MCM-41 phase with a pore diameter (peak of the PSD) of 4.2 nm. In the case of the sample with 50 % transformation, the isotherm shows the formation of a larger amount of MCM-41 (high pore volume) and a small amount of the remaining pore system with a very broad distribution. So, the calculation of PSD (intensity) detects only the narrow size distribution in the MCM-41 phase and the broad distribution of the disordered mesopores is not seen (intensity in the graph is low). For the 75 % transformed sample, the PSD gave a 4.1 nm at the
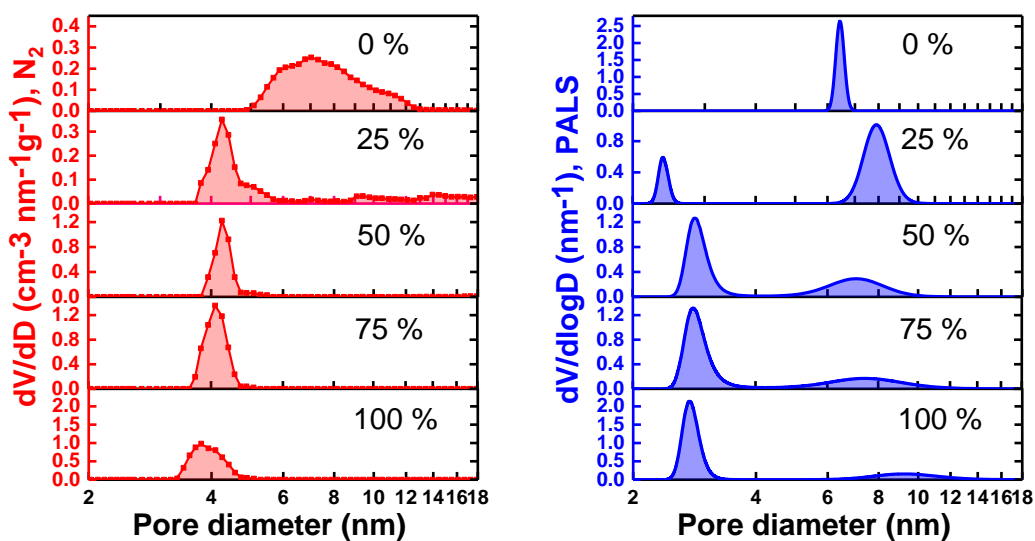
Figure 4.8: PSD of 6 nm pseudomorphic transformed pores of a silica-gel sample given by N_2 sorption using the DFT method (the light red distributions on the left) and by PALS using the method described in section 4.2.1.2 (the light blue distributions on the right)

maximum of the distribution and the pore volume is larger than the sample with 50 % transformation. This 75 % transformation degree can be considered as an initiation of the complete transformation of the silica gel into MCM-41 (from the specific surface area in table 4.3 and from the isotherm in figure 4.7). It should be mentioned here that the broadening of the MCM-41 phase would be due to the creation of MCM-41 domains in the silica gel particles with different ordering degree which means different pore sizes are included in the PSD. Interestingly, the sample with 100 % transformation showed a broad PSD with 3.8 nm pore diameter at the maximum of the PSD. The reduction of the mean pore size and the broadening of the PSD may be linked with the formation of an intermediate phase between MCM-41 and MCM-48 as MCM-48 has a smaller pore size and broader PSD because of the network feature of MCM-48.

PALS spectra were resolved by MELT program which gave six lifetime components for all samples where the three shortest-lived components represent the annihilation of p-Ps (τ_1 ~125-180 ps), the annihilation of free positron in the bulk and defects (τ_2 ~590-610 ps), and the annihilation of o-Ps in the material matrix (τ_3 ~1.7 ns (in the starting material)-2.2 ns (in the transformed products)) and the three longest-lived components represent the o-Ps annihilation in pores with different sizes (τ_{4-6} ~24-102 ns). PALS shows that the parent sample (denoted by 0 %) has a narrow PSD (by assuming cylindrical shapes of the pores) with a maximum at 6.3 nm (figure 4.8, right) in addition to micropores with 1.8 nm (not shown). This narrow PSD of the mesopores contradicts with the broad PSD given by N_2 sorption. O-Ps is predicted to diffuse through all available spaces in the sample and hence, detect the broad distribution of the mesopores of silica gel formed due to the spaces between its particles. So, such a narrow PSD would be obtained as a result of the milling of the sample to fit well in the sample holder. Unfortunately, the whole amount of the starting material was, later, consumed during the transformation and its re-measuring without the grinding is not possible. For this purpose, another silica gel (super gel) sample with nearly the same particle size ($\sim$ 200 μm) and pore size (6.4 nm) as the starting materials (in addition to 2.5 nm pores) was measured to check the effect of the grinding on the PSD by PALS. Figure 4.9 shows the PSD derived from PALS of the starting material (0 % transformation in figure 4.8, right) after grinding (figure 4.9.a) and of the super gel sample before and after grinding (figure 4.9.b). Obviously, the super gel sample before grinding has a broader PSD (the red distribution in figure 4.9.b) in comparison with the starting material while after grinding, the PSD is getting narrower (the green distribution in figure 4.9.b) with a shift in the pore size towards a lower value. This means that the grinding process might be the reason for the narrow PSD
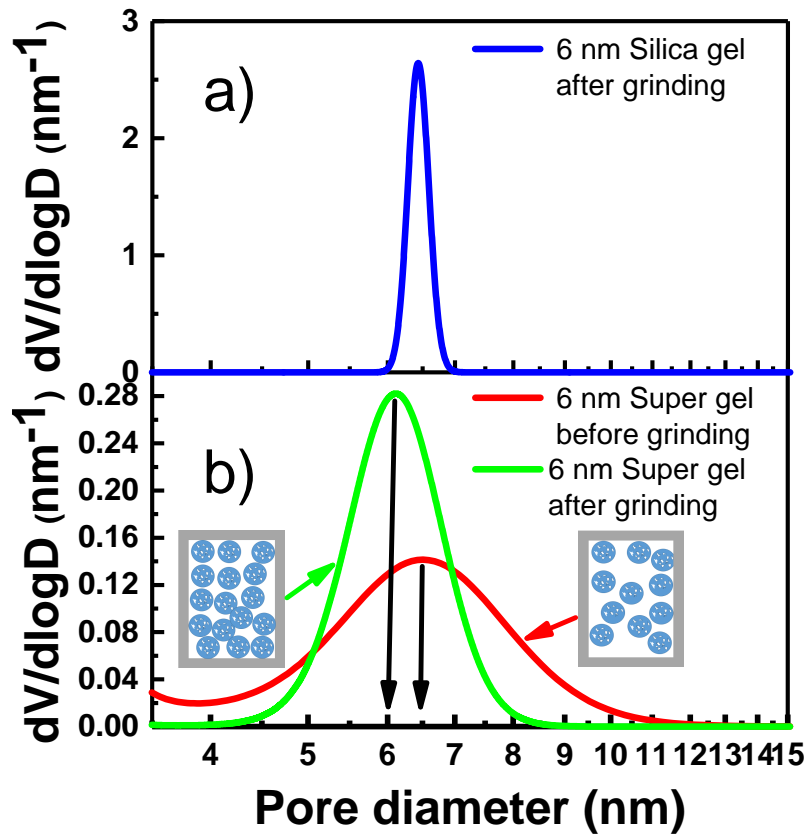
Figure 4.9: Comparison between PSD derived from PALS for a) the starting material after grinding and b) a super gel sample with and without grinding.

of the starting material and it causes a pore size reduction from 7 nm (given by N_2 sorption) to 6.3 nm. For this reason, all transformed samples were measured without grinding. Notably, the degree of PSD narrowing is larger in the starting material than in the super gel sample which could be attributed to the sample structure as the super gel sample has an additional pore meaning that the applied force during the grinding was shared between the bimodal pores.

For the sample with 25 % transformation, PALS detected bimodal pore distribution due to the formation of MCM-41 (shown in the N_2 isotherms) and a remaining porosity from the starting sample. Two differences are realized from the PSD given by PALS in comparison with that of the N_2 sorption method. Firstly, the pore size of MCM-41 is $\sim$ 2.35 nm (4.2 nm was given by N_2 sorption). Secondly, PALS showed that the pore size of the remaining porosity from the starting material has a bigger pore size than the parent sample and the pore volume of this remaining porosity is larger than the detected pore volume by N_2 sorption. The shift in the size of the remaining porosity would be caused by an overlapping of signals coming from o-Ps annihilation in the remaining porosity and from the intergranular spaces between MCM-41 fine grains or between the formed MCM-41 domains. Since the intergranular spaces are accessible from

the MCM-41, o-Ps would escape from MCM-41 into these spaces giving rise to their detected pore volume (due to the increasing in the intensity of o-Ps annihilating in these spaces) and reducing the detected pore size of the MCM-41 (due to the o-Ps migration as explained in section 4.2.1.2). With an increasing amount of CTAOH solution, i.e., with an increasing transformation degree in the range of 50-100 %, the pore size of the formed MCM-41 becomes nearly constant at 2.85 nm and its broadening is also constant (except for the sample with 100 % transformation which has a narrower PSD). On the other hand, the signal due to the o-Ps annihilation in the intergranular spaces is damped with increasing the transformation degree which means that the particles or the domains are getting closer to each other due to the increase of the amount of the CTAOH and, hence, increasing in the ratio of the formed MCM-41. An existence of regions inside the formed MCM-41 pores with irregular widths might be the reason for the tail of the distribution of the MCM-41 given from PALS which indicates an o-Ps annihilation from different spaces.

To test that there is an o-Ps escape form MCM-41 resulting in an underestimation of its detected pore size, the escape ratio (ER) was obtained. ER was calculated as the ratio between the peak area of the signals of o-Ps escape (intergranular spaces and/or any remaining porosity (if exists)) to the summation of the peak area of MCM-41 and the peak area of o-Ps escape. This ER correlates the ratio of the intensity of o-Ps escape to that in MCM-41 and intergranular spaces (taking into account that the 1.8 nm pores are closed and no o-Ps migration is possible). This assumption of calculating ER is valid because the Ps formation in interparticle spaces is negligible [205]. Figure 4.10 shows that the escape ratio is a reducing function with the transformation degree which might be due to the disappearance of the initial porosity (which contributes to the high ER for the sample with 25 % transformation) and the reduction in the concentration of the interparticle spaces of the finely formed MCM-41 particles. This reduction in ER does not continue to approach zero even for the sample with 100 % transformation which explains the reason for the disability of PALS to detect a comparable pore size of MCM-41 to that obtained by N_2 sorption. The reduction in the ER enhanced the o-Ps population in MCM-41 to some extent and hence, resulted in an increase in the peak area of MCM-41 (figure 4.10, the right axis). It is expected to detect nearly the exact pore size of MCM-41 by PALS as that obtained by N_2 sorption once the o-Ps escape (migration) stops. In case of there is no o-Ps escape from MCM-41 pores, the pore volume given by N_2 sorption can be used to calibrate the peak area of dV/dlogD of PALS results, as discussed in [134], which means a validation of PALS to measure the pore volume directly for MCM-41 (the calibration is material dependent).
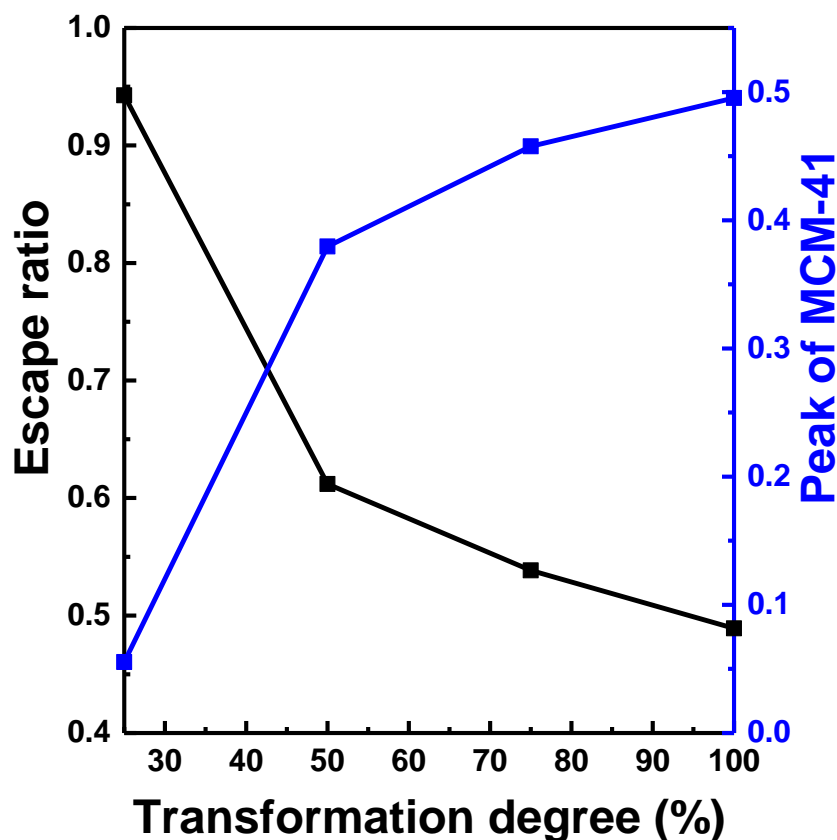
Figure 4.10: Escape ratio from MCM-41 and the integrated peak area of the MCM-41 pores.

4.2.2.4   Conclusions

The disordered porous structure of silica gel with 6 nm was changed into the ordered porous structure of the hexagonal MCM-41 by undertaking the pseudomorphic transformation approach. N_2 sorption method showed that the silica gel sample was completely transformed into MCM-41 after 75 % transformation degree. From the textural properties, it was found that the specific surface area is getting larger with the transformation, the pore volume of the starting material is reducing with the transformation, and the pore volume of the formed MCM-41 is increasing with the transformation. Additionally, N_2 sorption suggested that the 100 % transformed sample may have an intermediate phase of MCM-41 and MCM-48. PALS was used here as a complementary method and it showed very interesting results. It confirmed all the findings of the N_2 sorption such as increasing pore volume of the newly formed MCM-41 and the vanishing of the pore volume of the starting material as functions of the transformation degree. Interestingly, PALS has shown that the transformed samples have hidden large spaces between the particles or the domains of the formed MCM-41.

4.3 Pseudomorphic transformation of CPG studied by PALS

4.3.1 Introduction

Silica gel is widely available and its synthesis is well studied [196] however, its PSD is broad and preparation of macropores from silica gel is difficult even with using phase separated sol-gel monoliths (due to the shrinkage of the silica network during the drying) [196]. In contrast, CPGs can be prepared covering a wide pore size range from micropores to large macropores which allows CPGs to be a good choice as a starting material [196] of the pseudomorphic transformation. Additionally, CPG can be obtained in different geometries of a constant pore size but with different pore volumes and pore wall thicknesses (isoporous) [196]. Furthermore, CPGs have high mechanical, thermal, and chemical stability.

A comprehensive study has been made of the pseudomorphic transformation of CPG (beads and granules) having different pore sizes and pore volumes [196]. Also, the pseudomorphic transformation of CPG with a pore diameter of 53 nm was tested in [194]. Both studies have revealed very interesting findings regarding the mechanism of the transformation, the importance of the pore volume and size of the starting material, and the required concentration of the CTAOH solution used in the transformation to maintain bimodal pore sizes.

So far, the above studies have been performed using N_2 adsorption, Hg intrusion (in case of large mesopores and macropores), and hyperpolarized ^{129}Xe NMR. So in this part, PALS porosimetry is used which would be a complementary method confirming the findings of the used tools of porosimetry or it could give other interesting results due to PALS' uniqueness of probing the closed porosity and its sensitivity to the electronic structures.

Details of preparing the samples are given in Appendix C.3. The experimental details of N_2 sorption and PALS measurements are the same as described in section 4.2.1.1. For the quenching experiment by PALS, the sample was activated at 473 K for 5 h then annealed and measured at RT using Halle four-tube DPALS connected to a gas chamber. Four samples were synthesized by the pseudomorphic transformation (V-45-X, X = 25, 50, 75, 100 %, X is the transformation degree) by using different amounts of 0.08 M CTAOH vary from 0-42 ml g^{-1} to control the pore volumes of the starting material in relation to the MCM-41 pore volume.

4.3.2 Results and discussions

Nitrogen adsorption isotherms and PSD of the starting and transformed samples are shown in figure 4.11 and the textural properties are given in table 4.4. The
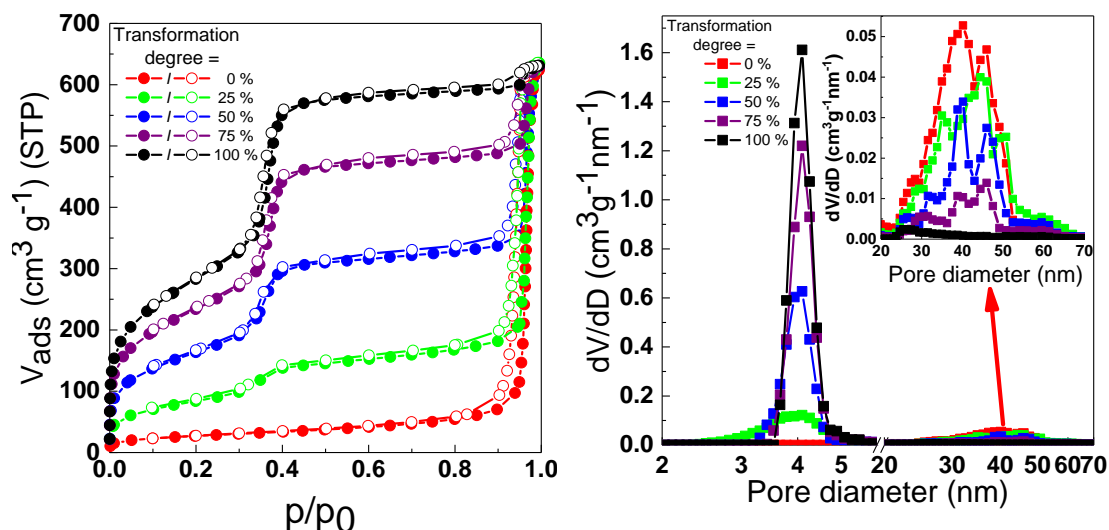
Figure 4.11: Nitrogen physisorption isotherm (left, closed symbols represent adsorption branch and open ones represent desorption branch) and the PSD (right) of the V-45 sample and its transformed products.

isotherm of the starting material (figure 4.11, left) exhibits type IV of isotherms reflecting the presence of big cylindrical mesopores with interconnectivity as a result of the leaching process. Evaluation of the PSD from the adsorption branch of the isotherm on the basis of DFT method, the part on the right of figure 4.11, shows that the starting material has a broad distribution (from ~25-~70 nm). The PSD reflects two overlapped peaks at ~40 nm and ~46 nm and their splitting is not clear so one may consider that this PSD reveals average pores having ~ 43 nm (table 4.4 and figure 4.11, right). After the transformation, the isotherm changes into type IV characterized by a steep increase at p/p_0 0.3-0.4, which is typical for MTS materials [196, 206] with a narrow pore size distribution at around 4 nm. Additionally, meso or macroporosity resulting from the remaining starting glass pores was obtained. The trend is with increasing the content of CTAOH solution, the remaining pore volume of the starting material is decreasing, the pore volume of the newly formed MCM-41 pores is increasing. Except for the 100 % transformed sample, the PSD of the other samples shows that there is no shift in the pore sizes but only a change in the volume due to the transformation was observed.

To examine these findings by another tool, PALS porosimetry is used to study the evolution of the pseudomorphic transformed CPG samples for the first time. PALS results obtained from MELT gave five (in the starting material) and six (in

Table 4.4: Textural properties of V-45 and transformation products

Property	Transformation degree (%)				
	0	25	50	75	100
^{a}S$_{BET}$ (m^{2}g^{-1})	95.00	308.00	596.00	847.00	1026.00
^{b}V$_P$ (cm^{3}g^{-1})	0.96	0.98	0.96	0.97	0.97
^{c}V$_{MCM-41}$ (cm^{3}g^{-1})	——	0.17	0.44	0.69	0.86
^{d} d$_P$ (nm)	43	43	43	43	26
^{d} d$_{MCM-41}$ (nm)	——	4.00	4.00	4.30	4.00

^{a}BET; ^{b}Desorption branch; ^{c}V-t method; ^{d}DFT.

the transformed samples) lifetime components. The three short lifetime component ($\tau_1 \rightarrow$ p-Ps annihilation, $\tau_2 \rightarrow$ free e$^+$ annihilation, and $\tau_3 \rightarrow$ o-Ps annihilation in the material's solid phase) are ignored from the discussion as they have no link to the porosity. The Ps lifetime distribution and its correlated PSD, using the method described in section 4.2.1.2, and based on the ETE model for cylindrical pores are depicted in figure 4.12.a, .b, respectively. PALS has revealed that the starting material (V-45) has one main big pores with 45 nm in diameter (figure 4.12.b) in addition to a negligible 1.68 nm micropores of $\sim$ 0.3 % intensity (not shown). Despite the not very high accuracy of PALS at pores as big as 45-50 nm, PALS shows a fairly good agreement with N$_2$ results for these pores. The very low-intensity of the 1.68 nm micropore would mean that the removal of the finely dispersed silica-gel using the NaOH solution has not been achieved successfully and some silica-gel having micropores are still in the sample. The low-intensity of these micropores means that their pore volume is very low and hence, a disability of N$_2$ adsorption to detect them. With
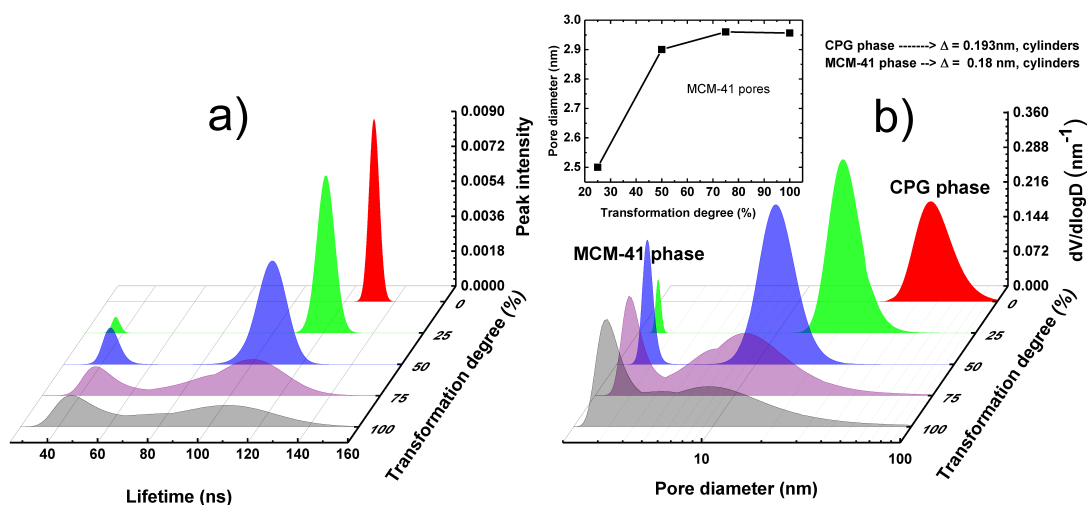
Figure 4.12: a) O-Ps lifetime distribution and b) PSD given by MELT of V-45 sample and its transformed products.

performing the transformation (from 25 - 100 %), some notes can be seen in figure 4.12.b:

- Starting from 25 % transformation, an additional component is obtained which reflects the formation of MCM-41 pores.

- The intensity of the MCM-41 pores increases monotonically, but the distribution increases with different rates.

- The original pore size (45 nm) and its peak intensity of the starting material are reducing with the transformation degree.

After the transformation, the pore size values of the MCM-41 pores (figure 4.12.b, inset) and of the original pore given by PALS are totally different from N_2 adsorption results (table 4.4 and figure 4.11, right). Firstly, the obtained pore size of MCM-41 by N_2 adsorption is $\sim$ 4 nm with only an increase in its pore volume due to transformation while PALS shows an underestimated pore size as it varies from 2.5 nm (25 %) to $\sim$ 2.95 nm (100 %). Such an underestimation of the MCM-41 can be explained as a result of o-Ps escape from the MCM-41 pores into the bigger pores of the parent material (same as in section 4.2.1.2). It was found in the literature that such an escape can be suppressed by quenching Ps in air [207]. It was explained that the oxygen in air will accommodate the bigger free spaces efficiently than the MCM-41 and hence any escaped o-Ps will annihilate in the oxygen which shortens its lifetime from > 100 ns (big pores or free spaces) to $\sim$ 0.5 ns (due to the quenching). The measurement in the air is doubtful as air contains moister and humidity which could be adsorbed during the measurement affecting the pore size. So, it was proposed to use oxygen with high purity (99.999 %) to do the quenching experiment. The quenching experiment has been carried out using a MCM-41 sample with a well-defined pore size of 4.3 nm (the same sample in figure 4.6) just to know the optimum pressure value able to suppress any o-Ps escape. Results of the quenching experiment given by LT9 are shown in figure 4.13. The results could not be explained either via the quenching model [208] nor via the assumptions in [207]. The quenching model, proposed by Zaleski [208] predicts a hyperbolic-like relation between the lifetimes and gas pressure and a smooth change in the intensity due o-Ps migration whereas the assumptions in [207] lead to see an increase of the o-Ps lifetime in the MCM-41 (due to the suppression of λ_{escape}). Such a disagreement could be there because the migration effects dominate in the sample and its contribution is much larger than oxygen quenching. It was suggested to increase the statistics from 4 million to 10 million or higher to get a better resolving of the lifetime components but no change has been observed with 10 million counts (at 800 mbar). Back to figure 4.12.b, the second contradiction
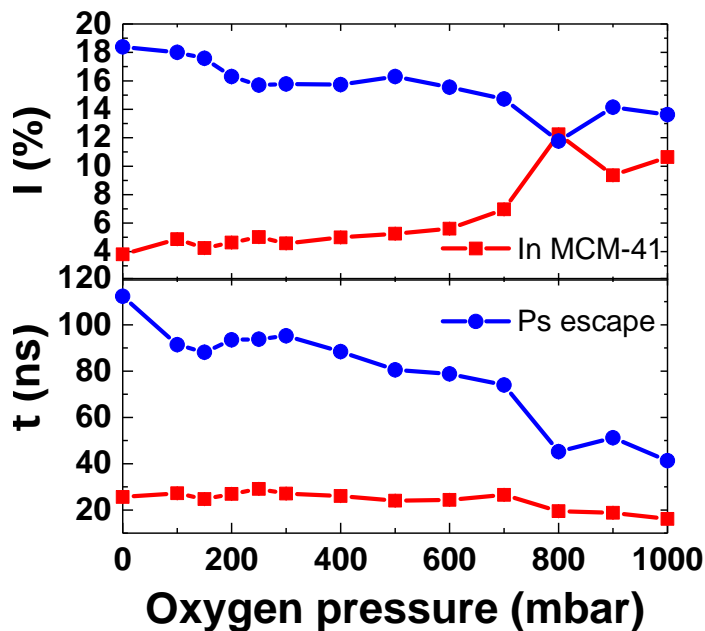
Figure 4.13: Change of o-Ps lifetimes and intensities due to quenching in high-purity oxygen adsorbed by a pure MCM-41 as a function of pressure

between PALS and N_2 sorption is the change of the size of the original pore with the transformation degree. PALS revealed that the size of the original pore is decreasing with the transformation degree while N_2 sorption showed only a decreasing in the pore volume. Such a misfit would clarify another feature of PALS which is "its sensitivity to the electronic structure of the inner pore walls". The "apparent" reduction in the size of the original pore would mean that the MCM-41 pores were formed inside the bigger pores (45 nm, from PALS). Since such a reduction of the original pore is not accompanied by any preserved original pores (of 45 nm), so it would suggest that the population of MCM-41 in all CPG pores is homogenous. This result would agree with the explanation given in [194] of a 53 nm CPG sample. It was concluded there that the evolution of the pseudomorphic transformation of CPG can result in a formation of domains of MCM-41 inside the particles as well as on their surfaces but with the maintenance of the original pores. This way, if MCM-41 is formed on surface to a certain depth and in domains, there would be part of CPG pores with smaller parts (near MCM-41) and with the original size. Most of Ps forms in MCM-41 because there is a larger probability of Ps formation in smaller pores. So it simply can not have time to diffuse to the part with larger pores while annihilating in the MCM-41 pores and the intermediated ones and this is represented only by the tail of very broad PSD. The argument of forming intermediated pores in

addition to the MCM-41 can be confirmed by SEM images of sample with 0, 50, and 75 % transformation (figure 4.14). With increasing the transformation
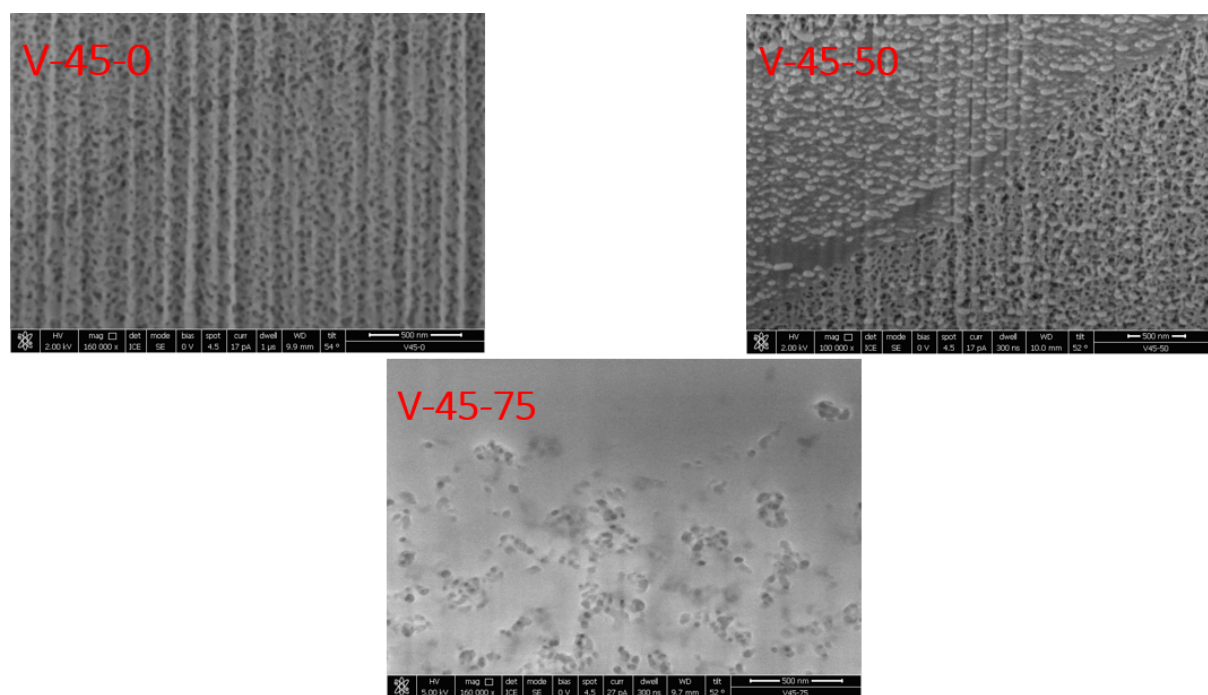
Figure 4.14: SEM images of sample with 0, 50, and 75 % transformation degrees.

degree, the formed MCM-41 pores populate the outer surface (the solid part in the images) of the particle (from accessible places by the CTAOH solution) and form domains inside the particle. The formed domains resulted in the shrinkage of some large pores and o-Ps is annihilating in the surface MCM-41 and in the reduced pores and has a negligible chance to reach any large pores. This idea is shown in figure 4.15.

To test this explanation, a temperature dependent measurement would be helpful. This is because if the pore is large enough, o-Ps can populate several energy levels [119] and with increasing the temperature its lifetime will decrease as it is averaged between different energy levels. And since the ETE model offers a relation between the pore size and the temperature using a fitting parameter, to fit the electronic density in the potential well (Δ), so, any experimental data of a known pore size can be fitted to the ETE model with varying the Δ value (as it is not a universal value and it is material dependent). This allows determination of the exact Δ value for a certain class of materials [119]. The same idea is used here using sample with 50 % transformation degree which means half of it is CPG and half of it is MCM-41. The ETE model predicted 0.18 nm as a value of Δ for several porous-silica based materials like MCM-41 [153] and 0.193 nm for CPG [65]. So, if there is no MCM-41 inside the CPG, the experimental data of the large pores (CPG) should fit well using $\Delta = 0.193$ nm. Figure 4.16 shows
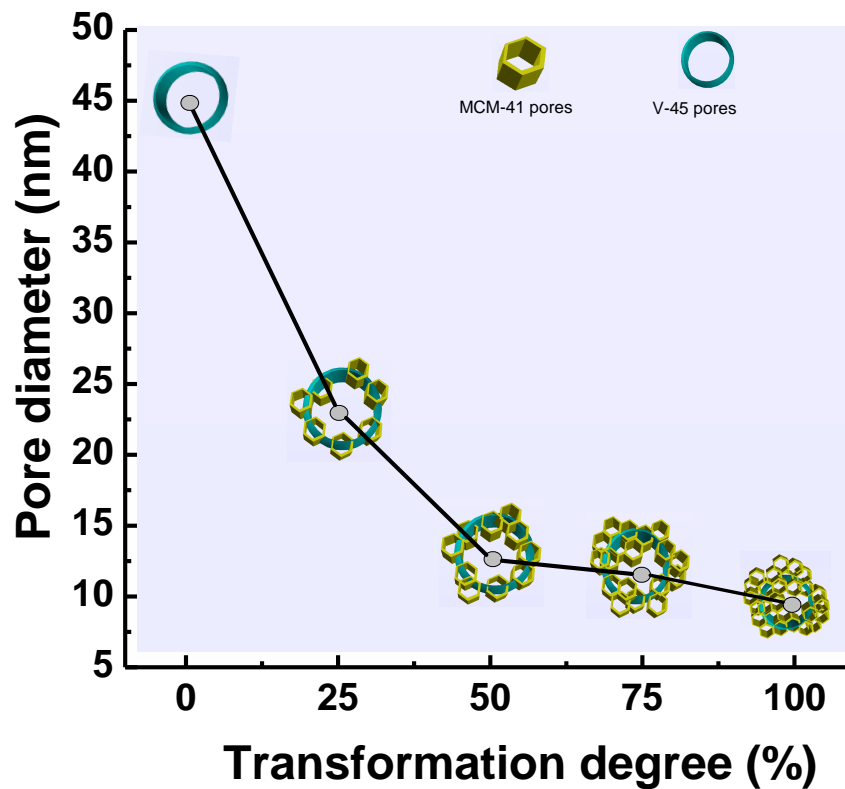
Figure 4.15: Schematic representation of the possibility of MCM-41 protrusion inside the V-45 pores.

the temperature variation of the o-Ps lifetime of sample V-45-50 (50 % transformation) and the predictions of the ETE model, considering cylindrical pore geometry for the interconnected CPG, using different Δ values. The analysis has been performed using LT9 program. Clearly, at temperatures < 200 K all experimental data underestimates the theoretical data with different Δ values. Similar underestimation was observed before [85, 103, 209]. It was discussed in [85] that such a shortening in the o-Ps lifetime is due to the enhanced annihilation probability of o-Ps with the electrons in the pore walls. At low T, o-Ps has low thermal energy and hence it can stick to the pore walls causing a shortening in the o-Ps lifetime. A good agreement is expected to be seen at temperatures above RT. On the other hand, the experimental data approach the 0.193 nm line in the 230-300 K range (with a very bad agreement at 250 K and 260 K and with a perfect agreement at 230 K, 240K, and 300 K). Starting from 320 K, the experiment data fits well (except for some scattering at some T, see figure 4.16) with the ETE model having Δ = 0.18 nm (as expected for MCM-41). In summary, this temperature dependent measurements have clearly demonstrated that the walls of the big pores would have the same electronic structure as MCM-41. These findings may confirm that during the progressive transformation of the
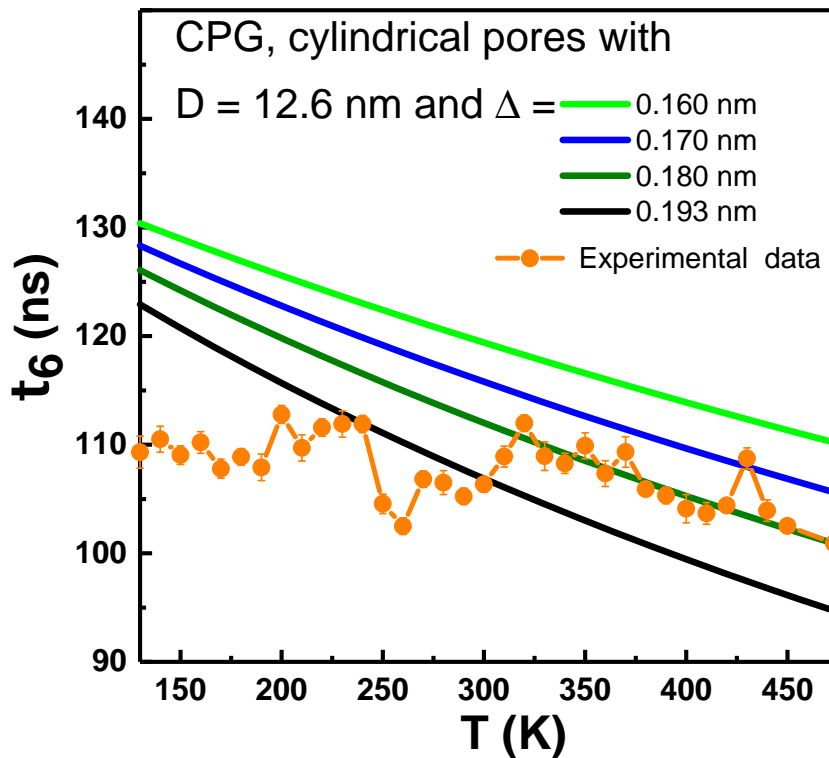
Figure 4.16: Temperature variation of experimental data and theoretical calculations with different thicknesses of the electronic layer of V-45-50.

pore wall, probably some of the newly formed MCM-41 are located inside the CPG pores causing a reduction in their size. The scattering in the data might be due to different arrangements of MCM-41. Sill, the undetectability of such a shrinkage by N_2 adsorption is questionable.

4.3.3   Conclusions

For the first time, PALS has been used to study the pseudomorphic transformation of CPG sample. N_2 sorption showed that a bimodal porous system with $\sim$ 43 (with a reduced pore volume) and 4 nm (with a growth in its pore volume) was formed during the transformation. PALS showed a decreasing in the pore size of the main pores and an underestimation of the newly formed MCM-41 pores. The underestimation of the MCM-41 pores has been attributed to o-Ps escape from the accessible MCM-41 pores into the larger pores exist in the starting material. The apparent reduction in the original pores might be due to the protrusion of the MCM-41 inside the big pores filling them to some extent. This MCM-41 protrusion was confirmed by SEM and a temperature dependent measurement by PALS which showed that some original pore sizes are get-

ting smaller due to the transformation and the pore walls of a similar electronic structure to MCM-41, respectively.

4.4 Direct evaluation of the pore volume from PA-LS results

From the study of the pseudomorphic transformation, it was shown that the calculated PSD from PALS data is a relation between the first derivative of the pore volume over the logarithmic pore diameter (dV/dlogD) and the pore diameter. This means that the integration of this distribution would give explicitly the pore volume but this is not the case because the obtained volume here is unitless. Another problem is the observed migration of o-Ps from the MCM-41 pores in all the measured systems. Such a migration means that some of the formed o-Ps in the MCM-41 are lost meaning a decrease in the o-Ps intensity (and hence the pore volume) in the MCM-41. Also, it will reflect a fancy increase in the large pores or free spaces to which the o-Ps was migrated. For these reasons, the direct calculation of the pore volume from PALS results requires a correction for the migration phenomena and for a physical unit.

Starting with the migration problem of the formed MCM-41 pores by pseudomorphic transformation of different systems, PALS detected one group of large pore in the starting materials and two groups of pores (due to the formation of MCM-41) in the transformed samples in addition to some closed porosities. By excluding the closed porosities, both PALS and N_2 sorption agreed together for detecting the accessible pores in the starting and transformed samples. So, it is quite reasonable to use the pore volume obtained using N_2 sorption for correcting the migrated o-Ps from MCM-41 pores. This correction can be made by calculating the ratio of the change in the pore volume between two consecutive transformation degrees and to use this ratio to correct for o-Ps migration from MCM-41 pores. For example, suppose that the pore volume given by N_2 sorption of a transformation degree is 0.2 cm^3g^{-1} and the pore volume of its sequential degree is 0.4 cm^3g^{-1}, this means that the pore volume of the first degree is half of that of the second degree. So if the integration of dV/dlogD of PALS data of the first degree gives, for example, 0.05 and that of the second degree gives 0.07, with correcting for the migration using the calculated ratio of the pore volume from N_2 sorption the integrated dV/dlogD of the second sample should give 0.1 not 0.07. By using this simple method, the corrected integration of dV/dlogD of the CPG, silica gel, and G-SHA systems in comparison with the obtained pore volume from N_2 sorption is shown in figure 4.17 (left).

Obviously, the corrected pore volumes from PALS data (unitless) still disagree
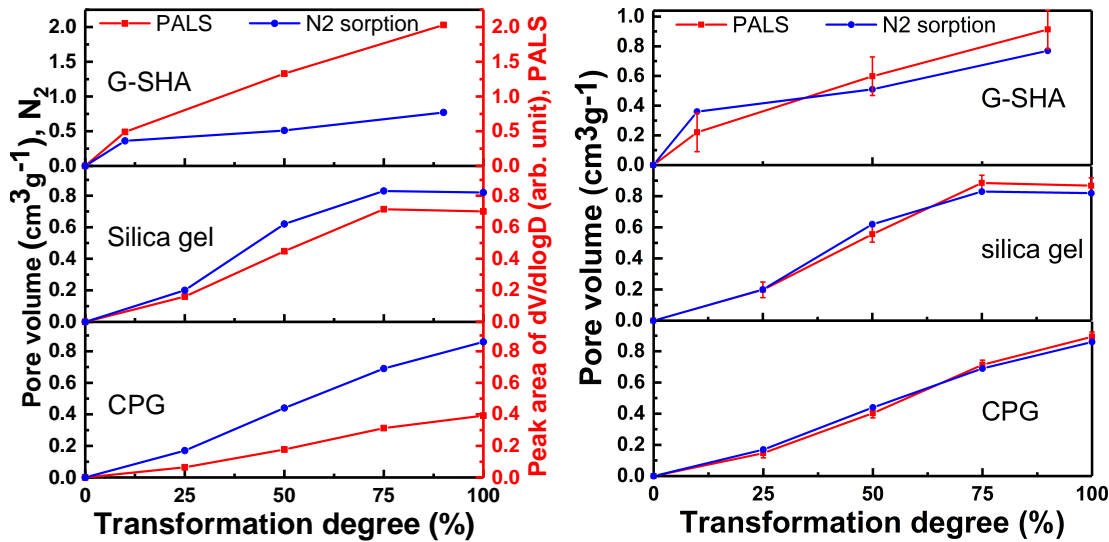
Figure 4.17: Correlation between the obtained pore volume from N_2 sorption and the pore volume from PALS data corrected for o-Ps migration without a unit (left) and with a unit (right) of the pseudomorphic transformed CPG, silica gel, and G-SHA samples at different degrees of transformation.

with the pore volume form N_2 sorption as PALS underestimates the pore volume for the CPG and silica gel samples and overestimates it for the G-SHA sample. This suggests that the correlation is material-dependent. This could be because the observed intensity of o-Ps in MCM-41 depends on how easily an o-Ps can migrate (all samples are measured at RT after annealing) i.e., maybe the migration ratio is not the same as the change in the pore volume given by N_2 sorption for all samples at all transformation degrees. Additionally, the disagreement between the corrected unitless pore volume given by PALS and the pore volume given by N_2 may suggest that the length of the formed MCM-41 pores is not the same in each system. This is because in the G-SHA sample, for example, the overestimation of the migration ratio indicates that the actual migration ratio is the smallest among other samples meaning that the length of MCM-41 is the longest. Similarly, the results suggest that the length of MCM-41 is the shortest in the case of CPG system. Here, we exclude that the Ps yield has an effect because the three measured samples are silica-based systems.

To get a good correlation between PALS and N_2 results, it seems that the corrected unitless pore volume given using PALS has to be multiplied by a correcting factor which has the unit of $cm^3 g^{-1}$ to quantify the integrated dV/dlogD values of PALS results. By doing so, a good agreement is obtained between PALS (by considering the data points and their uncertainties) and N_2 sorption results as shown in figure 4.17 (right). Clearly, the agreement is perfect in case of the CPG sample and it is modest for the silica gel sample while it has a relatively large error in the case of the G-SHA sample. This agreement was obtained

by correlating the pore volume of N_2 sorption with the corrected dV/dlogD of PALS by using the simple relation $V_{N_2} = a\ V_{PALS}$ where a is the correcting factor with cm^3g^{-1} unit. This equation is similar to the equation $V_{LN_2} = a\ V_{PALS} + b$ given by Zaleski et al. in [134] for mesoporous polymer-silica composites but here b is zero. The values of a are given in table 4.5 for the three measured systems.

Table 4.5: Correction factor of correlating PALS data and N_2 sorption pore volumes of the pseudomorphic transformed silica gel, G-SHA, and CPG samples

Sample	a (cm^3g^{-1})
G-SHA	0.45 ± 0.13
Silica gel	1.24 ± 0.05
CPG	2.28 ± 0.03

The obtained values for the factor a is valid for the studied complex (bimodal or multimodal pores) systems and their generalization for these three classes of materials is doubtful. This is because each sample has its own nature which controls the o-Ps migration. However, the described method here seems to be valid in case there is o-Ps migration (MCM-41 and small-particle porous systems). In the future, it is important to study these systems again with different lengths of the MCM-41 pores and similar porous systems (with multipores and containing o-Ps escape) to test the validity/meaningless of the obtained values here for the factor a to allow PALS to be a stand-alone tool of porosimetry for calculating the pore volume. It is expected that $a = 1\ cm^3g^{-1}$ in porous systems without any o-Ps migration or escape.

An attempt has been made to correlate the pore volume of the large pores (remaining porosity from the starting materials) by subtracting the ratio of the escaped o-Ps from the MCM-41 pores (given by the described method above) but the correlation failed. This is because o-Ps has escaped into intergranular spaces (in addition to remaining porosities from the starting systems) and the contribution of theses intergranular spaces is not the same for a given sample at all transformation degrees. Also, the volume of these intergranular spaces could not be observed by N_2 sorption meaning that PALS detected additional irregular free volumes and a very bad correlation was obtained.

4.4.1 Conclusions

By using the pore volume derived from N_2 sorption of the pseudomorphic transformed samples, it was possible to calculate the pore volume directly from PALS results with a good agreement with N_2 sorption. The generalization of the obtained correcting factor still requires other additional studies for simple

and complex porous systems but the described method works fine and can be used in the future for similar studies.

Chapter 5

Porosimetry of ultra-low-*k* materials by Mono-energetic Positron Source (MePS) at ELBE facility

5.1 Introduction

The production of porous low-*k* materials with lower relative dielectric constant (*k*<2) than that of SiO$_2$ (*k*=4), yielded a breakthrough in the microelectronics industry due to the significant decrease in the RC signal delay, signal cross-talking, power dissipation, and cost [210, 211].

The fabrication of porous dielectrics relies on the formation of a miscible and an interacting solution from a networking material and a thermal unstable "porogen". A thermal baking is required to remove the porogen from the deposited films to get emptied pores. Spin-on coating or plasma enhanced chemical vapor deposition (PECVD) methods are widely used to produce such porous low-*k* materials. Unfortunately, PECVD films have the drawback, that pore size and distribution is not controllable [212]. A novel spin-on-low-*k*$\sim$ 2 film based on template self-assembling approach [213] is used in this work.

The conventional techniques of porosimetry like gas adsorption and mercury intrusion are not reliable for characterizing $\sim$ 500 nm-thick films because they lose their sensitivity in films with less than 1μm-thick included on a sub-mm Si wafer [214]. Ellipsometric porosimetry (EP) and X-ray porosimetry (XRP) can be used for characterizing such thin films. Within EP method, the refraction index of the absorbent (toluene) is measured to get the pore size distribution [215] while XRP detects the density increase of the solvent. The applicability of EP and XRP requires pore accessibility and it is not possible to depth profiling the sample. While the tuneable energy of the slow positron beam is effectively able to control the depth of interest. By employing positron(ium) annihilation lifetime spectroscopy (PALS), it is possible to perform a depth profiling porosime-

try of open and closed pores of thin films [122]. Porosimetry by means of PALS was discussed in details in section 2.8 but it is worth to note here that in case of beam measurements of open or interconnected pores to the sample's surface, o-Ps can escape into vacuum giving the extreme o-Ps lifetime in the vacuum (142 ns) and an increase of the 3 γ / 2 γ ratio is anticipated.

In this chapter, the MePS system of ELBE facility at HZDR, Germany has been used to investigate the success of ultra-low-*k* (*ULK*) samples production via the template self-assembling method and to see the minimum curing time required to form the desired pore sizes.

5.2   Experimental details

Five samples with capping (WC) (capped with carbon layers of 20 nm thickness) and without capping (WO) cured at 723 K for 0, 05, 30, 60, and 90 minutes have been prepared according to [213]. The synthesis steps of the investigated samples are described in Appendix D.1.

MePS system is a user-dedicated system for thin films studies where the positron beam is created by bremsstrahlung process in a W converter due to the 35 MeV electron beam of the superconducting electron linear accelerator of ELBE facility [216]. The created e^+ in the W converter is being thermalized in a W moderator, biased by a +2 keV potential, and magnetically guided by an 8 mT longitudinal field [216] to the main cave. A beam-synchronized two-stage chopper of 5 ns FWHM is used to kick out any e^+ out-of-phase from the main e^+ beam to enhance the timing resolution. A 78 MHz double-slit buncher is used to align all e^+ in the beam to reach the sample surface at the same time. With such a combination of chopper/buncher, the average timing resolution is about 340 ps FWHM which is sufficient for porous materials investigations. For porous materials with long lifetimes, a 1.625 MHz repetition rate (corresponds to 615 ns) is used [216]. A single crystalline Y_2O_3-stabilized ZrO_2 (YSZ) with a well-known lifetime of $\sim$ 181 ps has been used as a reference sample to get precisely the FWHM values of MePS at different e^+ energies. The YSZ sample revealed another lifetime component with $\sim$ 800 ps / 5% which has an unknown origin and it is subtracted from the spectra during the analysis. Five million counts have been accumulated for each sample at positron energies of 2, 3, 4, 5, 6, 8, and 10 keV and analyzed by LT10 routine [152]. The mean implantation depth of positrons was calculated by using the Makhovian profile [72, 217]. The Makhovian profile was described in details in Appendix D.2 and it gives the distribution of thermalized positrons as a function of the depth and the implantation energy. The pore size was calculated by using Excited Energy Levels

and Various Shapes (EELViS) program [153]. The samples were measured under ultra-high vacuum ($\sim 5 \times 10^{-7}$ mbar) at RT without any prior heating.

5.3 Results and discussions

Firstly, the uncapped five samples were investigated in order to study the pore's structure and their connectivity and to determine the lowest curing time required for forming such pores. The uncured sample designated as WO-00 contains three lifetime components of 0.125 ns, 0.5 ns, ~ 3 ns due to p-Ps, free positron, and o-Ps annihilation, respectively. The longest component (τ_3) reflects o-Ps annihilation in the bulk-nonporous material (small free volumes of bonds). On the other hand, the cured samples have larger values for τ_3 relative to the uncured sample (5-12 ns) which might be due to small micropores formation in addition to the free volume. The change in τ_3 with the curing time (not shown) is not monotonic but it is constant for each sample between mean positron implantation depth $\sim$ 100-420 nm. Additional two long-lived components are observed in the cured samples. The variation of the longest two o-Ps lifetimes and their intensities of cured samples as functions of the positron implantation energy is depicted in figure 5.1. Just beneath the surface (2 keV), τ_4 has its highest value for WO-05 sample and it decreased with E up to 6 keV then it increased slightly and saturated at 8 keV (figure 5.1.a). Similarly, WO-30 and WO-60 samples showed high values of τ_4 at low E then they nearly have the same value and
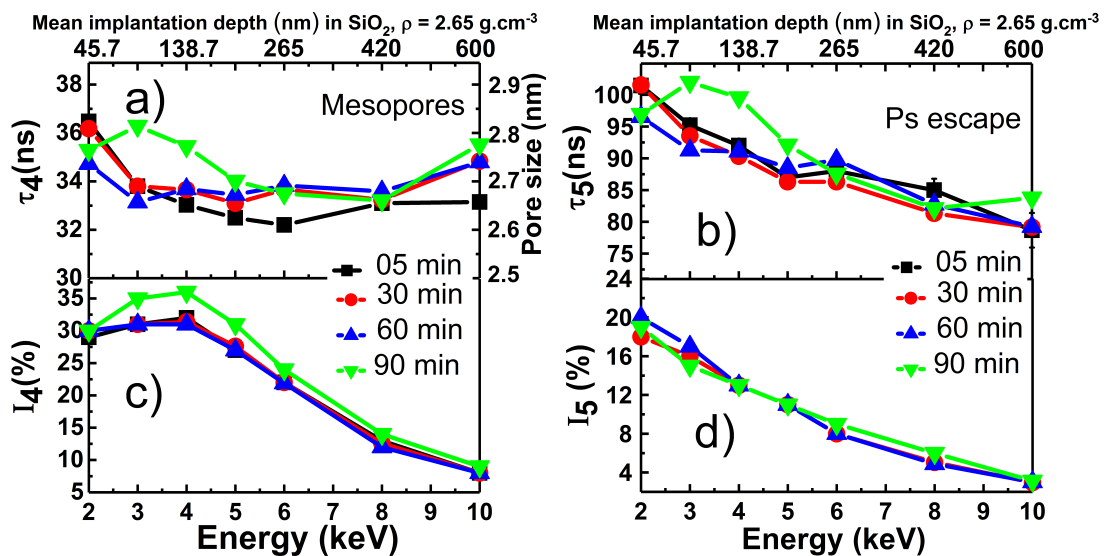

Figure 5.1: Dependence of lifetimes (and intensities) of o-Ps annihilating in mesopores and their correlated spherical pore sizes (the right axis of the graph of τ_4) (left) and lifetimes and intensities of o-Ps escape into vacuum (right) against positron implantation energy (E) of uncapped samples cured for different times. Errors in data are small to be seen.

trend in the 3-8 keV range but they increased at 10 keV. τ_4 of WO-90 sample has a maximum value at 3 keV then it decreased till 8 keV and it increased again at 10 keV. The above description of τ_4 reflects the variation of the size of the produced mesopores shown on the right axis of figure 5.1.a, which agrees quite well with the expected pore size (2-3 nm). The values of τ_5, which measure unexpected pore sizes, indicate the o-Ps escape due to open/interconnected pores (figure 5.1.b). In figure 5.1.c, it is clear that I_4 is independent of the curing time in the 05-30 min curing range and it is constant in the ULK film (45.7-138.7 nm) but it decreased smoothly at higher implantation depths. The variation of I_5 with E is depicted in figure 5.1.d where it reached $\sim$ 3 % at 10 keV while it is $\sim$ 20 % at 2 keV which could confirm the consideration of τ_5 as a measure of the escaped o-Ps lifetime. It is anticipated in open and/or interconnected porous structures that thermalized o-Ps can reach the sample surface during its diffusion and escape into vacuum. However, such an escape has a less probability at high E. This is due to the internal collisions with the pore walls and, in consequence, the increasing of the pick-off annihilation probability. The values of τ_5 are consistent with those obtained by the group of K. G. Lynn [218] and they differ from the 142 ns of o-Ps in vacuum due to the bad detection efficiency of the escaped o-Ps with MePS setup [219]. Therefore, it is clear now that the cured samples (even with 5 min) have open porous structure, which allows o-Ps escape (τ_5 and I_5). However, such an escape does not affect the measured pore sizes in the film strongly as expected (from τ_4 and I_4 ($\sim$ 30-35 %)) which could mean that in addition to the open/interconnected pores, there are some closed/isolated pores in the samples.

To get rid of the effect of the o-Ps escape on the measured o-Ps LTs, a 20 nm-thick carbon layer is used as a capping to confine o-Ps in the sample. The capped samples showed only four LT components which means that the capping works well and no Ps escapes. Surprisingly, near the surface (2-4 keV), I_3 (mirrors the concentration of the free spaces between bonds) is lower than those of the uncapped sample (not shown here). This could mean that carbon *diffuses* and fills some of the formed micropores during the capping process. On the other hand, τ_4 showed longer values comparing with the uncapped samples (due to o-Ps escape) as shown in figure 5.2, left. The measured pore sizes (figure 5.2, left) show that WC-05 has the smallest value (2.9 nm) at 2 keV and it is increasing till 5 keV (3.3 nm) then it is slightly decreased at higher E (3.29 nm at 10 keV). Also, the pore size of WC-30 started with small values ($\sim$ 3.05 nm) at 2 keV and it is shows an increasing function with E as it reached 3.34 nm at 10 keV. The pore size of WC-60 has slightly decreased from 3.4 nm at 2 keV to 3.35 nm at 10 keV. The pore size of WC-90 is increasing with E up to 5 keV

(3.4 nm) but for higher E it reduced slightly reaching 3.35 nm at 10 keV. The trend of the mesopore's intensity of the capped samples (figure 5.2, left)
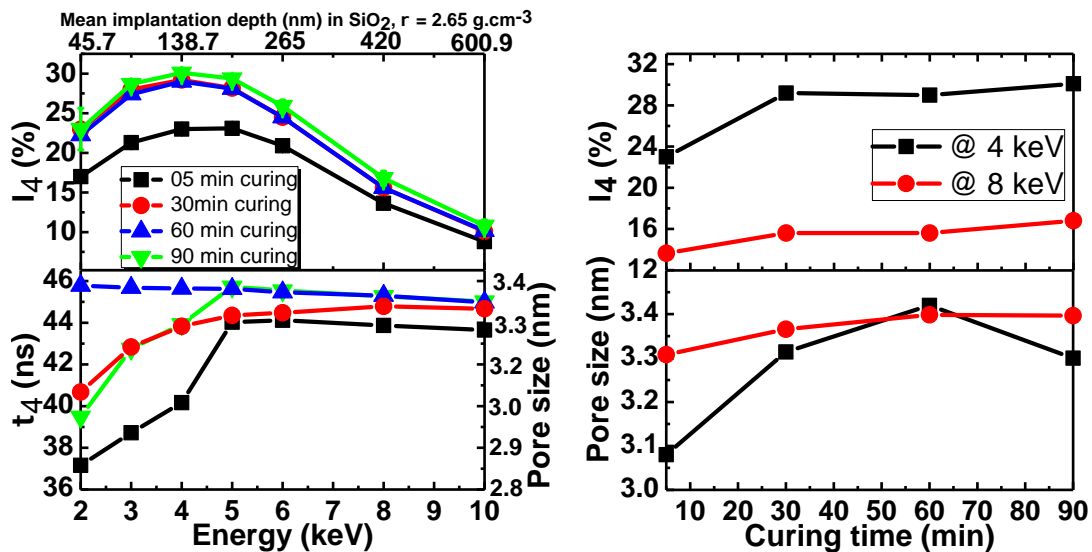
Figure 5.2: Dependence of o-Ps lifetime, intensity, and spherical pore sizes (left) on E of ULK capped with 20 nm C layer and dependence of the pore size and o-Ps intensities of capped samples at 4 keV and 8 keV on the curing time (right). Errors in data are small to be seen (except for I_4 at 2 keV for the 90 min cured sample).

is similar to that of the uncapped ones with two differences; firstly, the intensity of WC-05 is the smallest comparing with the other samples (which is quite plausible due to the short curing time); samples WC-30, WC-60, and WC-90 have nearly the same intensities with a small decrease in WC-60. To get a better evaluation of the dependence of the pore size and their concentration (Ps intensities), a comparison has been made at 4 keV (at the highest intensities) and at 8 keV (close to the end of the film). The right part of figure 5.2 shows that pore size at 4 keV increases with the curing time (except for 90 min of curing). Pore size at 8 keV is > at 4 keV (except for 60 min of curing). I_4 (pore concentration/volume) increases with the curing time (with a step in the 30-60 min range). I_4 at 4keV is > I_4 at 8 keV.

Worth mentioning, I_4 in the ULK films of all capped sample (figure 5.2, left) in the 2-4 keV range is smaller than this of the uncapped samples (figure 5.1.c). This can be understood by considering, again, the carbon diffusion to the micropores. In addition to the free positron annihilation in the cap layer and the substrate (the high intensities at 2 keV and 8-10 keV, respectively), another fraction of free positrons would annihilate with the diffused carbon atoms to the near-surface micropores. Such a diffusion caused the filling of some accessible micropores to the mesopores in the capped samples. Thus, the lower values of I_4 in the capped samples relative to the uncapped ones could mean that some

of these accessible micropores to the mesopores were filled by the diffused carbon, accordingly, a reduction of the additional source (due to migration from micropores) of I_4 in the capped samples. This expectation is confirmed experimentally in figure 5.3. Figure 5.3.a shows that the intensity of free positron annihilation (I_{e+}) in two capped and uncapped samples (as examples) cured for 5 and 90 min. Obviously, I_{e+} is higher in the case of capped samples (except for 3 keV) which could mean that some porous sections in the capped samples have been replaced by non-porous parts (diffused carbon here). Additionally, figure 5.3.b shows that I_3 is smaller in the case of capped samples indicating the partial filling of their micropores by carbon.
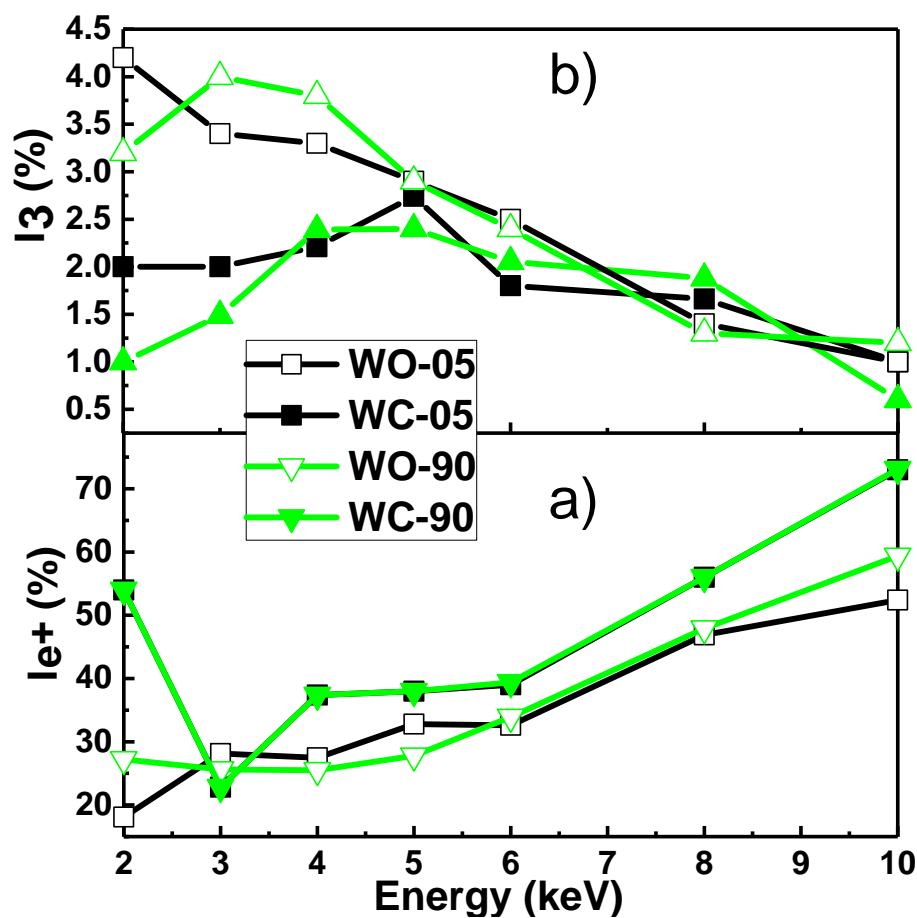
Figure 5.3: a) Change of the intensity of the free e^+ annihilating in the 5 min and 90 min capped and uncapped samples and b) total intensity of o-Ps of all capped and uncapped ULK samples with E.

5.4 Conclusions

PALS results showed that the synthesis of ULK materials via template self-assembling method (at Fraunhofer, ENAS and Chemnitz University) was suc-

cessfully performed with the expected properties. Thermal curing for 5 min is sufficiently enough for pore formation. In the case of uncapped samples, MePS showed a clear behavior of o-Ps escape, which mirrors accessible pores to the surface due to either open structure or interconnectivity. Capping the samples allowed o-Ps to detect $\sim$ 3.4 nm spherical pores in the film with an increase in their concentration with curing time and the highest concentration is included in the 0.1 -0.2 μm range (corresponding to the 3-5 keV energy range of implanted positrons). The comparison between capped and uncapped samples indicated a presence of an interconnected micropore-mesopore structure. The detected high o-Ps yield correlates the presence of high porosity in the samples.

Chapter 6

Summary

The goal of this thesis is to investigate materials having very interesting characteristics by PALS. These characteristics were gained due to the use of new and/or alternative routes in the synthesis processes. In this thesis, PALS has shown as a powerful technique for forming complementary visions of those obtained from gas sorption and x-ray. Also, PALS helped for explaining some findings which were hard to be explained by other tools of porosimetry.

Three main topics are discussed in the course of this thesis by using PALS as a main method of porosimetry; chapter 3 presents the porous structure of some MOFs after their evacuation; chapter 4 explains the evolution of pseudomorphic transformation process of silica-based materials into MCM-41; and in chapter 5, depth-profiling and investigation of ultra-low-k films cured for different times by mono-energetic positron source are given.

In **chapter 3**, the study can be subdivided into three parts;

In **part 1**, the goal is to reconcile the discrepancies between crystallographical and gas sorption porosity which exist in MOFs. IFP-6[1] was used as an example. Gas uptake by IFP-6 at various temperatures and 1 bar was negligible (in comparison with IFP-1 with smaller pore size and volume) though the kinetic diameter of the gases is smaller than the effective pore size. This underperformance of IFP-6 was expected to be due to pore collapse due to their activation. PALS was applied to explore, uniquely, the pore collapse assumption. PALS has found that some primary pores were deformed after heating the sample at 473 K and a new component of o-Ps reflecting larger pores (defects) appeared. The intensity of o-Ps in the large pores was decreasing with the activation time meaning pore filling or densification. The densification would result in the blocking of the small pores and hence, gases could not be adsorbed. Consistently with PALS results, crystallographical analyses showed that a rough surface can be formed after activation because IFP-6 have a flexible five-fold coordination after activation while it was six-fold before activation. Also, the assumption of

---

[1]Imidazolate Framework Potsdam-6, see section 3.2 for more details

pore blocking could be confirmed by considering the water instability in IFP-6 which attains a higher coordination number in polar water solvent so the solvent removal may facilitate instability at the Cd^{II} center. Hence, the amorphous material and rough surface can be generated by partial framework cleavage at the outer surface, which closes the pore window.

Part 2 is dedicated to exploring the structure of new HOF[2] samples because it was found that some HOFs have superior properties for the mixture gas separation. Two samples, HIF-3-CE[3] and HIF-3-MW[4], were investigated in this part. Unfortunately, both HIF-3-CE and -WM have shown that they encounter instability of their porosity. Similar to other reported H-bonded framework, this instability exists because the H-bonding networks are more fragile and they may collapse after solvent removal. Gas sorption of HIF-3 CE and -MW showed that these samples have comparable gas uptake of other H-bonded frameworks but they have a very wide desorption hysteresis suggesting a flexibility and irregularities of the structure. PALS was used to get a complete mapping of the samples' stability upon their evacuating at different temperatures for different times. Uniquely, PALS has shown that HIF-3-CE sample has activation-induced defects with $\sim$ 3.9 nm in diameter (by considering spherical shape) after evacuating the sample at 373 K for 12 h and 2.4 nm in HIF-3-MW sample. As a rough estimation and by considering the correlation between the concentration of defect with o-Ps intensity, it was found that $\sim$10 % of the micropores in HIF-3-CE were converted into mesopores (defects). This contribution was increased to $\sim$14 % in HIF-3-MW sample. The detection of these defects by PLAS suggests the missing of the building blocks at some places due to the week H-bonding. Despite the use of the MW-assisted conditions enables faster synthesis (1 h in comparison with 6 days in case of CE) and resulted in the production of HIF-3 solely but its structure is less stable in comparison with its CE counterpart (10 % defects contribution in CE sample while 14 % in the MW sample). This was explained as the fast crystal growth under MW conditions allowed not enough time for the building block to occupy the correct place. The existence of some deformed linkers inside the pores in case of the MW samples was confirmed from the pore sizes detected by PALS which have smaller values when compared with the CE samples.

Part 3 contains the results of new IFP members which showed several-fold enhancement of CO_2 and H_2 uptake capacities when synthesized under MW-assisted conditions compared to the analogous CE-heating method based materials. The aim of this part was to figure out the reason for such a high gas uptake of the MW based sample. Three CE based and three MW based ma-

---

[2]Hydrogen-bonded Organic Framework   [3]Conventional Electrical heating   [4]Microwave-assisted conditions

terials with different metallic elements and linkers, named IFP-7, -8, 10, were studied in this part. On one hand, in addition to the detection of micropores, PALS detected mesoporos in all samples synthesized by MW and CE methods. These mesopores were attributed to defect formation due to missing of linkers. On the other hand, the characteristic type-I isotherm of the H4 type hysteresis for H_2 adsorption could prove the crystal defects due to the mesopore formation in microporous materials. PXRD could not reflect any broadening in the reflexes suggesting smaller crystallites due to a partly amorphous phase formation. PALS has shown that both small and large (defect) pores in MW based samples are less than small and large pores in CE based samples. The smaller pore sizes in MW based samples was explained in terms of incorporation of extra linkers in pores. This incorporation would cause ultramicropore formation which is difficult to be seen by N_2. So, the CO_2-accessible micropore volume of MW-assisted materials has shown higher values than CE-assisted IFPs due to a larger number of ultramicropores in the MW-assisted materials. Small gas molecules may strongly interact with the narrow sized pore walls of these ultramicropores in MW-assisted materials, exhibiting enhanced gas sorption compared to that in CE-assisted materials.

Chapter 4 explains the pseudomorphic transformation process and presents the results of pseudomorphic transformation of three different systems of silica sources into MCM-41. The characterization in principle has been done by N_2 sorption and, for the first time, by PALS.

The first studying system is a biomass system in form of spelt husk ash. The extraction of silica from such a system (which can be considered as a waste) exemplifies the optimum exploitation of the agricultural resources and lowers the cost of MTS synthesis process. And to continue with cost lowering of MTS synthesis, a cheap surfactant has been used in this study and MW conditions which saved the synthesis time. PALS confirmed the N_2 sorption results concerning the formation of MCM-41 having an increasing pore volume with the transformation degree. Also, PALS detected closed pores in the starting material which were maintained after the transformation at all degrees. At transformation degrees < 90 %, PALS underestimated the MCM-41 pores due to the o-Ps escape into the remaining porosity of the starting material. At 90 % transformation degree, an excellent agreement between PALS and N_2 sorption results of detecting narrow 4.3 nm pores of MCM-41 was obtained because of the nearly complete transformation of spelt husk ash into MCM-41 and the absence of any remaining porosity of the starting material. Such an agreement suggests the use of the described procedure of transforming spelt husk ash into MCM-41 for any future studies and it sheds light on a bright future of biomasses in the synthesis

of mesoporous silica-based materials.

The second system of pseudomorphic transformation is the disordered silica gel with 6 nm pores which were transformed into 4.2 nm MCM-41 pores. According to N_2 sorption data, the success in transforming of silica gel into MCM-41 was shown in the isotherm shape and the increasing in the specific surface area and pore volume of MCM-41. Also, N_2 sorption isotherms showed that a complete transformation of silica gel occurred at 75 % transformation degree. PSD derived from N_2 sorption by DFT produced broad MCM-41 pores at 100 % transformation degree which may reflect an intermediate phase between MCM-41 and MCM-48. PALS results detected a transformation mode of silica gel to MCM-41 in addition to closed micropores in silica gel particles. Additionally, PALS underestimated MCM-41 pores due to o-Ps escape (even in case of no remaining porosity from the starting material) which suggests that the formed MCM-41 pores are contained in fine particles. PALS results also showed that the porous structure is sensitive to external forces (even by hand).

The third system is a CPG sample with 45 nm which was transformed into 4 nm MCM-41 pores. A similar study was performed before but without the use of PALS so, in the presented study here PALS was used to confirm the findings of N_2 sorption data for the first time. N_2 sorption showed that the specific surface area was getting larger with the transformation degree. The increase in the pore volume with the transformation of the newly formed MCM-41 pores and the attenuation of the pore volume of the starting material was confirmed by both methods. Additionally, PALS detected closed pores in the starting materials and it was preserved in all transformed samples. Again, the o-Ps lifetime in MCM-41 showed an escaping behavior into the larger pores of the starting material accordingly, it underestimated the MCM-41 pores. We tried to suppress the o-Ps escape from MCM-41 pores by oxygen quenching, but data analysis using the quenching model of Zaleski showed that the o-Ps migration (escape) dominates over the quenching thus, we failed to detect the expected pore size. Also, PALS results showed that the pore size of the starting material is decreasing with the transformation degree.This reduction of the original pores could not be detected by N_2 sorption. This reduction was explained as some of the original pores were partially transformed into MCM-41 which maintained in the original pores producing an apparent reduction in their sizes. The unaffected original pores (given by N_2 sorption) are expected to be deeply located inside the particles and o-Ps had no enough time to reach them before annihilation. Temperature-dependent measurement by PALS showed that the reduced pores have the electronic structure of MCM-41 which confirm the expectations. SEM images showed also that the transformed samples have reduced pores as well as

large pores (which were located in the core of the particle) and the surface has a layer of MCM-41 in addition to MCM-41 in domains.

By using the pore volume derived from N_2 sorption of the pseudomorphic transformed samples, it was possible to calculate the pore volume directly from PALS results with a good agreement with N_2 sorption. The generalization of the obtained correcting factor still requires other additional study for simple and complex porous systems but the described method works fine and can be used in the future for similar studies.

Chapter 5 describes the need for preparing low-k materials with $k > 2$ for better performance of microchips. In the microelectronics industry, it is recommended to integrate low-k films having monodispersed pore sizes and well-defined arrangement or ordered pores into microchips in new generations of smaller feature sizes. The self-assembly approach was found to produce ordered pores with definite sizes. Based on this, five samples were prepared by the self-assembly approach cured for different times. Films with ~ 500 nm thickness cannot be investigated by gas sorption or mercury intrusion which give unreliable results at this thickness. On the other hand, both ellipsometric porosimetry and x-ray porosimetry cannot give depth-profiling measurements, so the MePS system at ELBE facility was used in this study. Two sets of samples with and without 20 nm carbon cap layer were studied. In the uncapped samples, PALS showed that there was an o-Ps escape which reflected open pores to the surface. After capping the samples, the correlated pore size-o-Ps lifetime shows that the samples had 3.4 nm pores. PALS showed that 5 min of curing was enough to form these pores but they required longer curing times to remove the porogen from more pores. The concentration of the pores increased at each curing time with the depth till ~ 0.2 μm then it decreased with the highest concentration in the 0.1-0.2 μm range. At ~ 0.14 μm and ~ 0.4 μm, the pore sizes were increasing with the curing time except for 90 min at ~ 0.14 μm.

The evolution of the pores with the curing time is not fast as expected, so it is intended to prepare new sample cured at different temperatures. Also, the understanding of the pore evolution is important especially to know the moment and the temperature of forming interconnected (open) pores. For this reason, in-situ curing measurement is planned in the future using AIDA 2 system (under construction currently).

Appendices

Appendix A

Additional information about chapter 2

A.1 Stopping profile of positron in porous materials

Figure A.1 shows the stopping profile of positrons in porous materials having ρ = 1.0 g.cm^{-3}. This figure is drawn according to;

$$S_p = 1 - exp(-\alpha Z), \alpha(cm^{-1}) = \frac{17(cm^{-2}g^{-1}) \times \rho(g.cm^{-3})}{E_{max.}^{1.43}}.$$
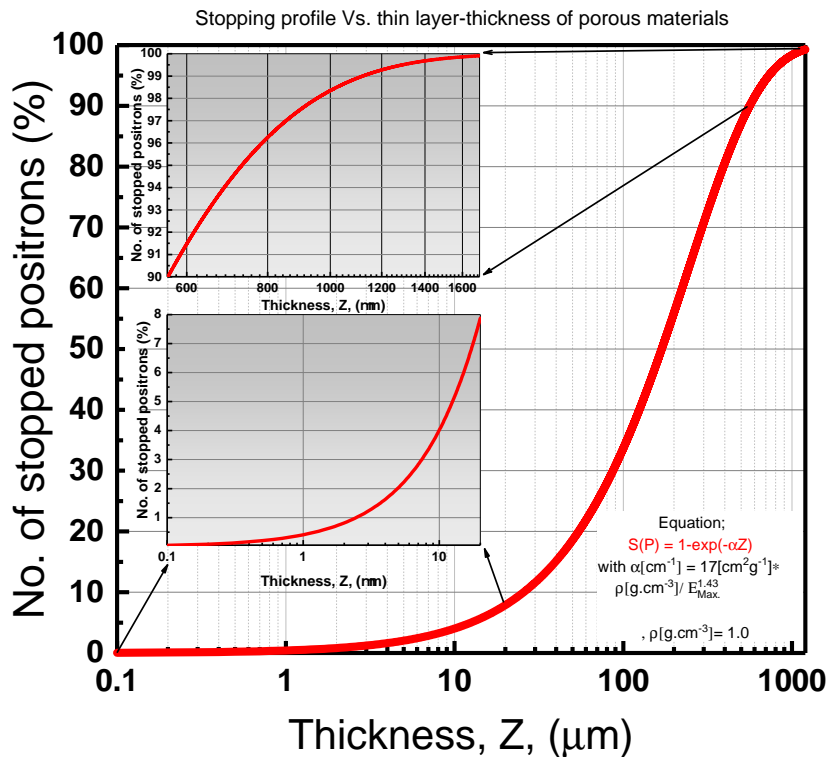

Figure A.1: Stopping profile of positrons in porous materials.

Appendix B

Supporting information of chapter 3

B.1   Supplementary information of IFP-6 and -1

Synthesis and gas sorption measurements and analyses of all samples of this chapter have been carried out by Dr. S. S. Mondal, the group of Prof. Holdt, Potsdam University

B.1.1   Synthesis

Crystalline IFP-6 ([Cd(L1)].0.5DMF.0.75H_2O) was formed in a mixture of ionic liquid (IL), 3-methyl-1-octylimidazolium 4,5- dicyano-2-methylim-idazolate (IL1), with Cd(OAc)$_2$.2H_2O in DMF under solvothermal conditions (figure 2.1). 4,5-Dicya no-2- methylimidazolate, the anionic part of IL1, acts as a source of the linker and transforms into the chelating imidazolate-4- amide-5-imidate linker (L1), which forms a neutral and highly crystalline framework. Zn-MOF (IFP-1) was synthesized from 4,5-dicyano-2-methylimidazole (1) as a linker precursor, under solvothermal conditions in DMF. To obtain a new Cd-based IFP from linker 1, several types of reactions with different Cd salts have been carried out, but none of the reactions yielded a framework that was isostructural to IFP-1. Hence, linker 1 was modified into an IL precursor(IL1; figure B.1) wherein the linker was preionized as the imidazolate anion, whereas the countercation, 3-methyl-1-octyl imidazolium, was not involved in coordination bonding. It is anticipated that the cation of IL1, which was large with a bulky alkyl chain, would enhance the hydrophobic character in solution, prevent favorable solvent–framework interaction, and therefore, lead to the formation of a 3D framework.
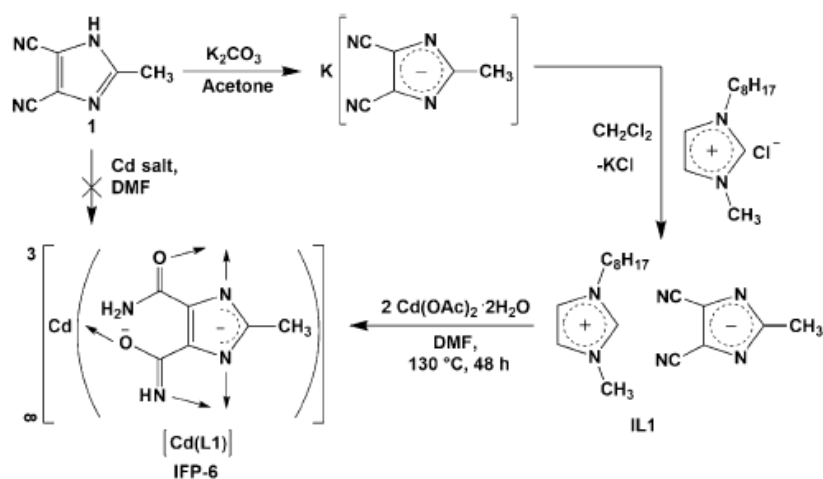
Figure B.1: Synthesis of IFP-6 from the IL precursor (IL1) [150].

B.2 Supplementary information of HIF-3

B.2.1 Synthesis

HIF-3-CE is formed by in situ hydrolysis of 4,5-dicyano-2- methoxyimidazole (L1) with an equimolar amount of Cd (ClO$_4$)2·6H$_2$O in N,N'-dimethylformamide (DMF) under solvothermal conditions by conventional electrical (CE) heating at 408 K with a reaction time of 6 days (Scheme B.2). Partial hydrolysis of the cyano groups of L1 to amide groups and of the methoxy to the hydroxy group followed by two-fold deprotonation generates the L2 linker. The linker L2 is only stable in the deprotonated and metal-coordinated state. Under these reaction conditions, in addition to HIF-3-CE, the in situ functionalized linker, 2-methoxy imidazolate 4-amide-5-imidate (L3) and its MOF IFP-14 (IFP=Imidazolate Framework Potsdam), is also formed as a minor by-product (Scheme B.2). IFP-14 was separated using the sieving technique. It was re-

Figure B.2: Generation of in situ imidazolate-4,5-diamide-2-olate (L2) and 2-methoxy imidazolate-4-amide-5-imidate (L3) linker under solvothermal conditions in DMF.

ported previously the synthesis of zinc or cobalt-L2 based H-bonded MBB networks respectively, as minor products from the same reaction conditions and along with this, the L3 linker based MOFs IFP-7 and -8, respectively, as a major product. It was reasoned that the CE-synthetic conditions c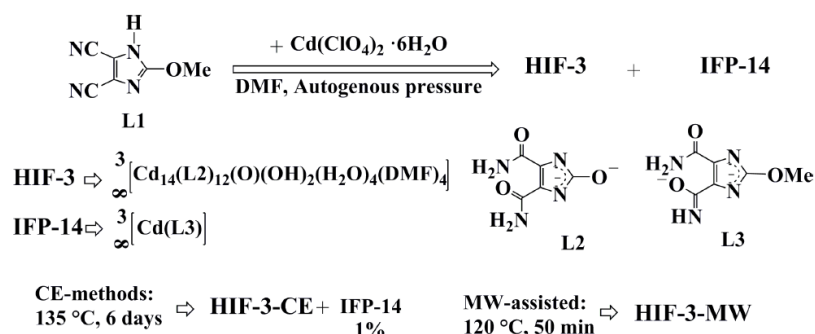ould be "thermodynamically" driven, allowing long time (6 days) for crystal growth in a reversible self-assembly synthesis process. Under this slow process, both the in situ L2 and L3 linkers were generated and, hence there should have been a competition for coordinating to the metal center, forming L2 linker based hydrogen-bonded MBB structures or L3 based MOFs. Noteworthy, in the hydrogen-bonded MBB structure, the metal centers, e. g., Zn and Co required higher coordination number of six or seven. In contrast, Zn and Co in the MOFs IFP-7 and -8, respectively were five-fold coordinated by the L3 linker. Due to the bigger size of Cd, the reaction preferably yields six-fold coordinated Cd center, forming the HIF-3-CE structure, as the major product.

Interestingly, when the reaction was done under microwave (MW)-assisted conditions (Scheme B.2), only phase pure, HIF-3-MW was formed and no by-product IFP-14 was detected. For the first time, in the MOFs areas, it has shown that MW-assisted condition has an advantage to the formation of a single product, where the conventional CE-heating methods gave a product mixture (Scheme B.2). Nevertheless, the MW-assisted condition has been shown to be particularly favorable to avoid uneven heating of the reaction chamber, resulting in the formation of only a high-temperature product, HIF-3-MW in having greatly reduced reaction times associated with rapid heating through the dipole effect rather than convection and conduction. The reason of forming only HIF-3-MW can be inferred that under a MW-assisted fast heating process the reaction rate of the double hydrolysis of L1 to L2 is enhanced (Scheme B.2), resulting only in the "kinetically controlled" single product of HIF-3-MW.
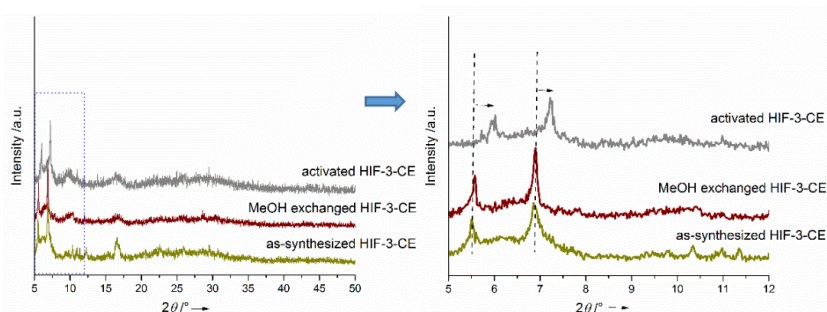
B.2.2 PXRD

Figure B.3: Comparison of the PXRD patterns of the HIF-3-CE. In the close up (right side) of the lower angle region from $2\theta = 5\text{-}12°$ the shifting reflections belonging to equivalent lattice planes are marked with a black arrow.

B.3 Supplementary information of IFP-7, -8, -10 -MW and -CE

B.3.1 Materials synthesis

The linker precursors 4,5-dicyano-2-methoxyimidazole (1a) and 4,5-dicyano-2-etho-xyimidazole (1b) were synthesized according to the published procedures [178,179]. All reagents and solvents were used without further purification. The MW-assisted synthesis was performed on the microwave system CEM Discover. For general synthesis, 50 mg of the linker precursor 1a/1b and an equimolar amount of metal salt hydrates were dissolved in 3.5 mL DMF and placed in a 10 mL glass vial with a magnetic stirrer. Under MW-assisted conditions at 393 K and 60 min reaction time, powdery materials were obtained. The material was filtered and washed with DMF (3 × 4 mL) and ethanol (3 × 3 mL). Samples IFP-7, -8 and -10 under MW-assisted conditions, named here IFP-7-MW, -8-MW and -10-MW, respectively, were synthesized in higher yields (77 to 84%) in a short reaction time of 1 h. IFP-7, -8 and -10 were also synthesized under CE-conditions (renamed here IFP-n-CE) with 52 to 67 % yield.

B.3.2 Elemental analysis

IFP-7-MW$\rightarrow$ Yield: 54 mg (81%) based on $Zn(NO_3)_2\cdot 4H_2O$; elemental analysis; Found, C 30.94; H 3.74; N 17.00; ATR-IR: 3320, 3103, 1658, 1543, 1442, 1263, 1225, 1111, 830, 741, 678 cm^{-1}.

IFP-8-MW→ Yield: 51 mg (77%) based on $Co(NO_3)_2 \cdot 6H_2O$; elemental analysis; Found, C 32.41; H 3.82; N 17.63; ATR-IR: 3345, 1655, 1558, 1467, 1403 1285, 1110, 810, 726, 687, 580 cm^{-1}.

IFP-10-MW→ Yield: 61 mg (84%) based on $_3)_2 \cdot 6H_2O$; elemental analysis; Found, C 33.84; H 4.10; N 17.51; ATR-IR: 3338, 1655, 1544, 1467, 1389, 1341, 1285, 1110, 1034, 817, 692, 523 cm^{-1}.
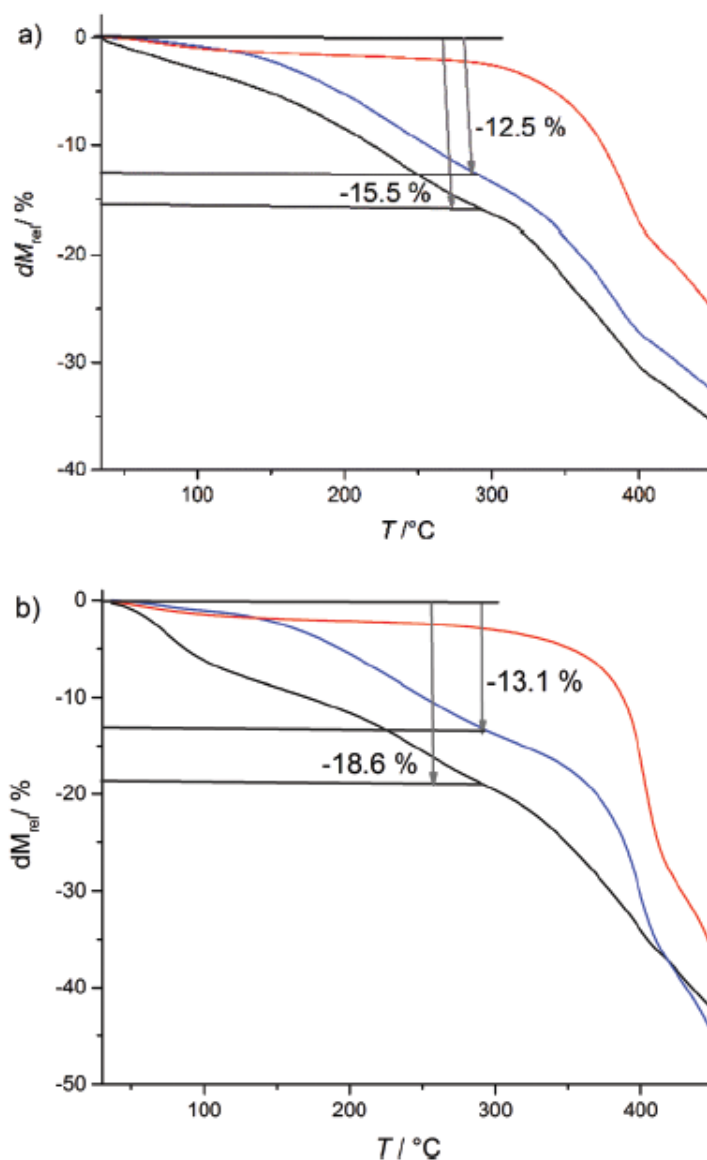
B.3.3 TGA analysis

Figure B.4: TGA curves for (a) IFP-7 and (b) IFP-8 (black: as-synthesized under CE-conditions; blue: as-synthesized under MW-conditions and red: activated under MW-conditions).

Appendix C

Supporting information of chapter 4

Sample preparation and gas sorption measurements and analyses of all samples of this chapter have been carried out by M. Sc. D. Schneider (biomass samples) and Dr. H. Uhlig (silica gel and CPG samples), the group of Prof. Enke, Leipzig University

C.1 Preparation of porous biomasses and transformation of German-Spelt Husk Ash (G-SHA)

Six biomasses (from different countries) were used in this study named, German-Horsetail (G-HT), Vietnam- rice husk (V-RH), Italy-rice husk (I-RH), German-spelt husk (G-SH), Cambodia-rice husk (C-RH), and German-oat husk (G-OH). C-RH and V-RH samples were provided by Deutsches Biomasseforschungszentrum Leipzig GmbH (DBFZ), Germany. I-RH sample was purchased at Agromil Cereali s.r.l., Italy. G-OH and G-SH samples were provided by Bayerischer Müllerbund e.V., Germany. G-HT sample was harvested near Leipzig, German. The used chemicals were citric acid (C6H8O7*H2O, technical grade, Citrique Belge, Tienen, Belgium) and sulfuric acid (H2SO4, 96%, reagent grade, Acros Organics, Germany) for leaching, NaOH (Merck KGaA, Darmstadt, Germany) and Cetyltrimethylammonium chloride (Arquad[®] 16 29, Akzo Nobel, Stenungsund, Sweden) for pseudomorphic transformation. In all cases, deionized water was used. A two-step procedure was used to prepare the biogenic samples; in the first route, 100 g of the biomasses (except for horsetail) were subjected to 1300 ml of a 0.35 M citric acid (solid-to-liquid ratio 1:13) and agitated in a four-necked round-bottom flask with 450 rpm (mechanical stirrer, Heidolph RZR 2021, Schwabach, Germany) at 353 K for 2 h. The horsetail was treated as following: stirring in with water for 2 hours at 353 K and afterwards with 1 M sulphuric acid for 2 hours at 353 K under the same conditions as the other biomasses. After filtration, specimens were washed with water and

dried overnight at 323 K in a drying oven (WTB Binder, Tuttlingen, Germany). Burning of the biomass samples to produce the ashes was the second route as the samples was burned in porcelain crucible consecutively in a muffle furnace (VEB Electro Bad Frankenhausen, Germany) using the following steps: 583 K for 30 min, 723 K for 60 min, 783 K for 210 min and 872 K for 30 min with a heating rate of 10 K min^{-1}.

By employing pseudomorphic transformation approach, G-SHA sample (powder) was transformed into MCM-41 (90 % transformation) in an oven using conventional heating for a mixture containing 21 ml of an aqueous solution of 0.18 M CTAOH and 1 g of G-SHA. This mixture was allowed to react at 393 K for 6 days. To get different degrees of transformation of the G-SHA sample, 1 g of G-SHA was added to an aqueous solution of 0.09 M CTACl (a cheap surfactant) and 0.13 M NaOH (10 % transformation) or 0.30 M NaOH (50 % transformation) in PTFE microwave (360 W) vessel for 10 min. The idea behind the microwave transformation was to shorten the time of transformation significantly. All transformed samples, after oven and microwave synthesis, were washed three times with 50 ml water and dried at 323 K for 24 h. Finally, they were calcined using the following parameters with a heating rate of 600 K min^{-1}: 473 K / 2 h, 573 K / 2 h, 673 K / 2 h, 813 K / 2 h and white powdery samples were obtained.

C.2   Synthesis and pseudomorphic transformation of silica gel samples

Pseudomorphic transformation of the silica gel sample with 6 nm in diameter and 100-200 μm particle size was carried out using an aqueous solution of CTAOH. This solution was prepared by ion exchange of cetyltrimethylammonium bromide (CTAB (Fluka, 96%)) using the anion exchanger Ambersep$^{\circledR}$ 900 (OH) (Alfa Aesar) for 24 h at room temperature. After ion exchange, the concentration of CTAOH was determined by titration. The reaction was performed in Teflon autoclave at 393 K for 72 hours. The final concentration of the resulting CTAOH solution was 0.08 mol/L. Four samples were synthesized by the pseudomorphic transformation (V-45-X, X = 25, 50, 75, 100 %) is the transformation degree) using different amounts of CTAOH vary from 0-42 ml g^{-1} to control the pore volumes of the starting material in relation to the MCM-41 pore volume. After the synthesis, the products were filtered, washed three times with distilled water and dried at 323 K for 24 h. After drying, the products were calcined in air using the following temperature program: heating rate 10 K min^{-1} to 823 K with isothermal steps at 423 K for 1 h, 673 K for 1 h, 823 K

for 4 h.

C.3   Preparation and transformation of CPG

A powder CPG sample in form of granular with $\sim$50 μm particle size with a pore size of 45 nm (denoted by V-45) and a specific pore volume of 0.96 cm^{-3} g^{-1} has been used as a starting material for the pseudomorphic transformation. The CPG sample was prepared using a sodium borosilicate glass comprises 70 wt % SiO_2, 23 wt % B_2O_3, and 23 wt % Na_2O. To get two overlapping phases of sodiumborate-rich phase and silicate-rich phase, the phase separation process has been conducted at 863 K for 24 h in a muffle furnace. The sodiumborate-rich phase was leached using an acid. The powder was stirred at 363 K for 18 h in a 3 N HCl solution to remove the soluble phase, washed to neutral and dried at 393 K. To clean the pore system, an alkaline treatment with 0.5 N NaOH solution at 303 K was conducted for 6 h. The pseudomorphic transformation and degree of transformation have been performed and calculated exactly as described in C.2.

Appendix D

Supporting information of chapter 5

Preparation of ULK films has been carried out by Dipl.-Ing. Nicole Köhler, *Chemnitz University*

D.1 Preparation of the ULK films

For preparing spin-on *ULK* material a solution from SBA Materials, Inc. was used. The *ULK* liquid precursor consists of an amphiphilic block copolymer with silicon alkoxide esters [213]. The final thickness is supposed to be 500 nm with an initial *k*-value of 2.2. The solution was spin-coated on 6-inch silicon wafers with 2000 rpm for 60 s. The spin-coated samples were soft baked for 120 s at 423 K. The curing procedure was performed with the quartz glass oven PEO 603 from ATV technologies for different curing times at 723 K under nitrogen atmosphere. The heating ramp of curing was chosen to be 7 K min^{-1}.

D.2 Makhovian profile

The implantation profile, P(Z, E), of a mono-energetic positron with energy E in sample with thickness Z and density ρ is given by;

$$P(Z, E) = \frac{mZ^{m-1}}{Z_0^m} exp \left[- \left(\frac{Z}{Z_0} \right) \right]^m with \qquad Z_0 = \frac{AE^r}{\rho \Gamma \left(1 + \frac{1}{m} \right)} \qquad \text{(D.1)}$$

where m=2, r=1.6, and A=4 μ g cm $^{-2}$ keV $^{-r}$ are empirical parameters and Γ is the gamma function. The mean implantation depth, $\overline{Z}$, is given by;

$$\overline{Z} = \frac{AE^r}{\rho} \qquad \text{(D.2)}$$

Graphically, the Makhovian profile of SiO$_2$ is shown in figure D.1.
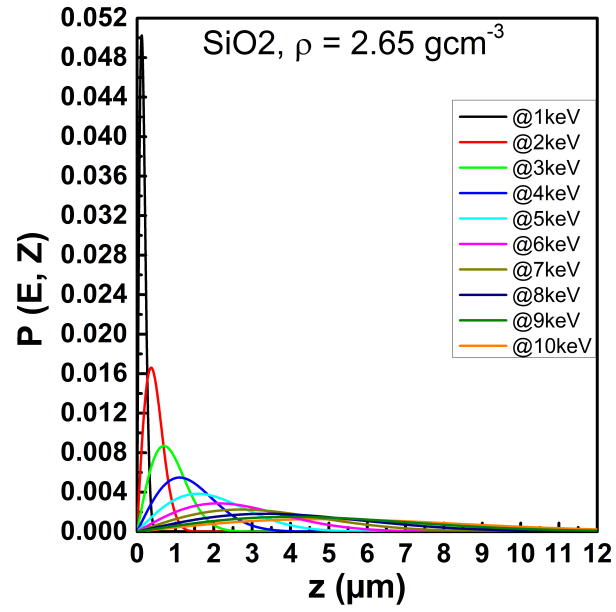
Figure D.1: Makhov profiles P(Z, E) in SiO_2 calculated for four incident positron energies according to equation D.1 and parameters described below it.

References

[1] www.esrl.noaa.gov/gmd/ccgg/trends/, Ed Dlugokencky and Pieter Tans, NOAA/ESRL.

[2] F. Fu and Qi Wang, Journal of Environmental Management, **92** (2011) 407.

[3] H. Jasuja et al. Chemical Engineering Science, **124** (2015) 118.

[4] Ioana Fechete and Jacques C. Vedrine, Molecules , **20** (2015) 5638.

[5] E. J. Creyghton and R.S. Downing, J. Mol. Catal. A. Chem., **134** (1998) 47.

[6] David J. Collins and Hong-Cai Zhou., Molecules, DOI: 10.1002/0470862 106.ia379.

[7] D. Shamiryan et al., Materialstoday, **7(1)** (2004) 34.

[8] R. J. Kuppler et al., Coordination Chemistry Reviews, **253** (2009) 3042.

[9] Jafar Alsayednoor., *Modelling and Characterisation of Porous Materials,* PhD thesis, University of Glasgow, (2013).

[10] K. S. W. Sing et al., Pure Appl. Chem , **57** (1985) 603.

[11] Mario Berett., *Nanostructured mesoporous materials obtained by template synthesis and controlled shape replica,* PhD thesis, University of Milano – Bicocca, (2009).

[12] B. Jha and D. N. Singh, Advanced Structured Materials, **78**, DOI 10.1007/978-981-10-1404-8_2.

[13] http://www.personal.utulsa.edu/ geoffrey-price/index.html, TU Chemical Engineering, zeolite page, by Professor Geoffrey L. Price.

[14] Sean M. Solberg., *Synthesis and characterization of new mesoporous materials and their application in catalysts and adsorption,* PhD thesis, University of Vermont, (2008).

[15] Sean E. Lehman and Sarah C. Larsen, Environ. Sci.: Nano, **1** (2014) 200.

[16] C. Dey et al., Acta Crystallographica Section B, **70** (2014)3.

[17] Owen J. Gledhill, *Tandem postsynthetic modification of the metal-organic framework DMOF-1-NH$_2$ using diketene and a range of metal containing reagents,* PhD thesis, University of Bath (2016).

[18] Yujia Sun and Hong-Cai Zhou, Sci. Technol. Adv. Mater., **16** (2015) 054202.

[19] V V Butova et al., Russ. Chem. Rev., **85(3)** (2016) 280.

[20] Y.-R. Lee et al., Korean J. Chem. Eng., **30(9)** (2013)1667.

[21] C. T. Kresge et al., Nature, **359** (1992) 710.

[22] Zeid A. ALOthman, Materials, **5** (2012) 2874.

[23] J. S. Beck et al, J. Am. Chem. Soc., **114** (1992) 10834.

[24] G. J. T. Tiddy, Phys. Rep., **57** (1980) 1.

[25] D. Zhao et al., Science, **279** (1998) 548.

[26] Jörg P. Thielemann et al., Beilstein J. Nanotechnol., **2** (2011) 110.

[27] K. Cassiers et al., Chem. Mater., **14** (2002) 2317.

[28] D. Zhao et al., J. Am. Chem. Soc., **120** (1998) 6024.

[29] A. S. Maria Chong and X. S. Zhao, J. Phys. Chem. B, **107(46)** (2003) 12650.

[30] D. Zhao et al., Adv. Mater, **10(16)** (1998) 1380.

[31] P. Van Der Voort et al., J. Phys. Chem. B, **106** (2002) 5873.

[32] D. J. Michalak et al., J. Mater. Res., **30(22)** (2015) 3363.

[33] A. Imhof and D. J. Pine., Nature, **389** (1997) 948.

[34] B. T. Holland et al., Science, **281** (1998) 538.

[35] A. Stein, Microporous Mesoporous Mater., **44-45** (2001) 227.

[36] Jayne Armstrong, *Gas Adsorption and Separation Properties of Porous Materials,* PhD thesis, New Castle University, (2013).

[37] Vera Bolis, *Fundamentals in Adsorption at the Solid-Gas Interface. Concepts and Thermodynamics In: Auroux A. (eds) Calorimetry and Thermal*

Methods in Catalysis, Springer Series in Materials Science, 154. Springer, Berlin, Heidelberg, **154** (2013).

[38] R. S. Mikhail et al., J. Colloid Interface Sci., **26(1)** (1968) 45.

[39] M. M. Dubinin, Proc. Acad. Sci USSR, **8** (1979) 1691.

[40] B. C. Lippens and J. H. de Boer, J. Catal., **4** (1965) 319.

[41] F. Rouquerol et al., J. Catal., *Adsorption by Powders and Porous Solids,*, Academic Press: London (1999).

[42] G. Horvath and K. Kawazoe, Journal of Chemical Engineering of Japan, **16** (1983) 470.

[43] E. P. Barrett et al., Journal of the Americal Chemical Society , **73** (1951) 373.

[44] S. Brunauer et al., J. Am. Chem. Soc., **60** (1938) 309.

[45] Robert Evans and P. Tarazona, Phys. Rev. Lett., **52** (1984) 557.

[46] Robert Evans et al., J. Chem. Soc., Faraday Trans. 2, **82** (1986) 1763.

[47] Robert Evans et al., J. Chem. Phys., **84** (1986) 2376.

[48] N. A. Seaton et al., Carbon, **27** (1989) 853.

[49] I. Langmuir, J. Am. Chem. Soc., **40** (1918) 1368.

[50] Irene Osagie Evbuomwan, *The Structural Characterisation of Porous Media for use as model Reservoir Rocks, Adsorbents and Catalysts,* PhD thesis, University of Bat, (2009).

[51] T. Takei et al., Colloid and Polymer Science, **275(12)** (1997) 1156.

[52] F. Rodriguez-Reinoso et al., *Characterization of Porous Solids II,* Elsevier Science Publishers B. V., **62** (1991).

[53] Lev D. Gelb and K. E. Gubbins, Langmuir, **15** (1999) 305.

[54] R. Sh. Mikhail et al., J. Colloid Interf. Sci., **26** (1968) 45.

[55] J. Landers et al., Colloids and Surfaces A: Physicochem. Eng. Aspects, **437** (2013) 3.

[56] C. Nguyen and D. D. Do, Langmuir, **15** (1999) 3608.

[57] S. Lowell et al., *Characterization of Porous Solids and Powders: Surface Area, Pore Size and Density,* Springer Netherlands, (2004) 116.

[58] Lawrence M. Anovitz and David R. Cole, Reviews in Mineralogy and Geochemistry, **80** (2015) 61.

[59] J. Kullmann et al., Eng. Aspects, **357** (2010) 17.

[60] B. Coasne et al., Langmuir, **22** (2006) 194.

[61] Kalliopi K. Aligizaki, *Pore Structure of Cement-Based Materials: Testing, Interpretation and Requirements,* CRC Press, (2005) 81.

[62] Hillar M. Rootare and Carl F. Prenzlow, J. Phys. Chem., **71** (1987) 2733.

[63] Simone Mascotto, *Synthesis of mesoporous metal oxides and their characterization combining small-angle scattering and gas physisorption methods,* PhD thesis, Justus-Liebig-Universität, (2009).

[64] K. Ito and Y. Kobayashi, Acta Physica Polonica A, **107(5)** (2005) 717.

[65] S. Thränert et al., Materials Science Forum, **607** (2009) 169.

[66] A. E. Ruark, Phys. Rev., **68** (1945) 278.

[67] R. E. Bell and R. L. Graham, Phys. Rev., **90** (1953) 644.

[68] A. T. G. Ferguson and G. M. Lewis, The London, Edinburgh, and Dublin Philosophical Magazine and Journal of Science , **44** (1953) 1339.

[69] Y. C. Jean et al., *Positron and positronium chemistry*, Amsterdam: Elsevier, (2003).

[70] Tomasz Goworek, J. Nucl. Radiochem. Sci., **1(1)** (2000) 11.

[71] M. Eldrup, J. Phys. IV France, **05** (1995) 93.

[72] Reinhard Krause-Rehberg and H.S. Leipner, *Positron Annihilation in Semi- conductors: Defect Studies*, Berlin:Springer-Verlag, (1999).

[73] P. A. M. Dirac, Proc. Roy. Soc.Lond, **A** (1930) 126.

[74] Carl D. Anderson , Science, New Series, **76(1967)** (1932) 238.

[75] Carl D. Anderson , Phy. Rev., **44** (1933) 406.

[76] T. C. Naginey et al., Phy. Rev. A, **89** (2014) 012708.

[77] S. V. Stepanov et al, Radiation Physics and Chemistry, **76** (2007) 90.

[78] Maik Butterling, *Application of High-Energy Photons for Positron Annihilation Spectroscopy and Positronium Chemistry,* PhD thesis, Martin Luther University Halle-Wittenberg, (2014).

[79] S. J. Tao, Appl. Phys., **10** (1976) 67.

[80] S.V. Stepanov and V.M. Byakov, *Physical and Radiation Chemistry of the Positron and Positronium,* In Y.C. Yean, P.E. Mallon, and D.M. Schrader, editors, Principles and Applications of Positron and Positronium Chemistry. World Scientific, (2003).

[81] P. G. Coleman, *Positron beams and their applications,* World Scientific (2000) 11.

[82] D. W. Gidley et al., Annu. Rev. Mater. Res., **36** (2006) 49.

[83] G. Dlubek et al., phys. stat. sol. (a), **174** (1999) 313.

[84] R. Lopez-Castanares et al., Bulg. J. Phys, **29** (2002) 155.

[85] Essmat Mahmoud Hassan, *Characterization of Control Mesoporous Glasses (CPGs) Using Positron Annihilation Lifetime Spectroscopy (PALS),* PhD thesis, Martin Luther University Halle-Wittenberg, (2007).

[86] J. Nissila et al., Nuclear Instruments and Methods in Physics Research A , **538** (2005) 778.

[87] James Patrick Ralston, *Design and Performance Analysis of an Ultra-Fast Digital Positron Annihilation Lifetime Spectrometer,* Master thesis, Ohio State University, (2013).

[88] K. Rytsölä et al., Applied Surface Science, **194** (2002) 260.

[89] J. Kansy, Nucl. Instrum. Meth. A , **374(2)** (1996) 235.

[90] J. V. Olsen et al., Phys. Status Solidi C, **4(10)** (2007) 4004.

[91] A. Shukla et al., Nucl. Instrum. Meth. A , **335(1-2)** (1993) 310.

[92] V. I. Grafutin and E. P. Prokop'ev, Physics - Uspekhi, **45(1)** (2002) 59.

[93] S. Mantl and W. Triftshäuser, Phys. Rev. B, **17** (1978) 1645.

[94] S. J. Tao, J. Chem. Phys., **56** (1972) 5499.

[95] M. Eldrup et al., Chem. Phys., **63** (1982) 51.

[96] Dull et al., J. Phys. Chem. B, **105(20)** (2001) 4657.

[97] K. L. Cheng et al., Critical Reviews in Analytical Chemistry, **21(3)** (1989) 209.

[98] Ito et al., J. Phys. Chem. B, **103(21)** (1999) 4555.

[99] T. Goworek et al., Chem. Phys. Lett., **272** (1997) 91.

[100] R. Zaleski et al., phys. stat. sol. (c), **4(10)** (2007) 3814.

[101] T. Goworek et al., Chem. Phys., **230** (1998) 305.

[102] M. Sniegocka et al., Acta Physica Polonica A, **107(5)** (2005) 868.

[103] Stefan Thränert, *Charakterisierung mikro- und mesoporöser Gläser mit Hilfe der ortho-Positronium Lebensdauer-Spektroskopie,* PhD thesis, Martin Luther University Halle-Wittenberg, (2008).

[104] R. Zaleski, Journal of Physics: Conference Series, **443** (2013) 012062.

[105] K. F. Canter et al., Physical Review Letters, **33** (1974) 7.

[106] A. Vehanen et al., Appl. Phys. A, **32** (1983) 163.

[107] J. M. Dale et al., Surf. Interface Anal., **2** (1980) 199.

[108] A. P. Mills and E. M. Gullikson, Appl. Phys. Lett., **49** (1986) 1121.

[109] G. Brauer et al., Appl. Surf. Sci., **116** (1997) 19.

[110] Chun Lei et al., Rev. Sci. lnstrum., **60(12)** (1989) 3656.

[111] Mohamed Elsayed, *The appearance of vacancies during Cu and Zn diffusion in III-V compound semiconductors,* PhD thesis, Martin Luther University Halle-Wittenberg, (2010).

[112] Marco John, *Untersuchung tiefenabhängiger Defektprofile mittels eines monoenergetischen Positronenstrahlsystems bei simultanem Ionenbeschuss,* PhD thesis, Martin Luther University Halle-Wittenberg, (2017).

[113] F. A. Selim et al., J. Appl. Phys., **97(11)** (2005) 113539.

[114] R. Krause-Rehberg et al., slopos,**12** (2010).

[115] F. Gabriel et al., Nucl. Instrum. Meth. B, **161-163** (2000) 1143.

[116] R. Krause-Rehberg, ELBE SAC-Meeting, (2016).

[117] M Jungmann et al., Journal of Physics: Conference Series,**443** (2013) 012088.

[118] Antti Laakso, *Construction of a pulsing system for low-energy positrons,* PhD thesis, Helsinki University of Technology, (2005).

[119] R. Zaleski, NUKLEONIKA, **60(4)** (2015) 795.

[120] R. Reisfeld et al., Optical Materials, **26** (2004) 181.

[121] C. L. Wang et al., J. Appl. Phys., **99** (2006) 113514.

[122] M. P. Petkov et al., Appl. Phys. Lett., **77** (2000) 2470.

[123] Asier Zubiaga et al., Appl. Phys. Lett., **18** (2016) 9211.

[124] O Šauša et al., Journal of Physics: Conference Series, **443** (2013) 012059.

[125] O Šauša et al., Journal of Physics: Conference Series, **618** (2015) 012041.

[126] R. Zaleski et al., Phys. Chem. Chem. Phys., **19** (2017) 10009.

[127] Marek Gorgol et al., NUKLEONIKA, **58(1)** (2013) 229.

[128] Chunqing He et al., Appl. Phys. Lett., **91** (2007) 024102.

[129] R. Zaleski et al., J. Colloid Interface Sci., **358** (2011) 268.

[130] Marek Gorgol et al., Microporous and Mesoporous Mater., **58(1)** (2013) 229.

[131] Ming Liu et al., Adv. Mater., **22** (2010) 1598.

[132] Agnieszka Kierys et al., J. Colloid Interface Sci., **349(1)** (2010) 361.

[133] H. Uhlig et al., J Porous Mater, **23(1)** (2016) 139.

[134] R. Zaleski et al., Adsorption, **22** (2016) 745.

[135] Priya Maheshwari et al., J. Phys. Chem. C, **121** (2017) 17251.

[136] J. Kullmann et al., Optica Applicata, **42(2)** (2012) 281.

[137] L. Liszkay et al., App. Phys. Lett., **95** (2009) 124103.

[138] J. A. Schwartz and C. Contescu (Eds.), *Surfaces of Nanoparticles and Porous Materials ,* (Surfactant Science), Marcel and Dekker, New York, (1999).

[139] J. Rouquerol et al., Pure Appl. Chem., **66** (1994) 1739.

[140] A. Figini-Albisetti et al., Appl. Surf. Sci. (2010), doi:10.1016/j.apsusc.2009.12.090.

[141] Seymour Lowell et al., *Characterization of Porous Solids and Powders: Surface Area, Pore Size and Density,* Springer Science and Business Media, 2006.

[142] Yoshitaka Inaki et al., Phys. Chem. Chem. Phys., **2** (2000) 5293.

[143] E. Jaramillo and M. Chandross, J. Phys. Chem. B, **108(52)** (2004) 2004.

[144] Jinhee Park et al., J. Am. Chem. Soc., **134** (2012) 20110.

[145] H.-C. Zhou and S. Kitagawa, Chem. Soc. Rev., **43** (2014) 5415.

[146] K. S. Walton and R. Q. Snurr, J. Am. Chem. Soc., **129** (2007) 8552.

[147] J. Hafizovic et al., J. Am. Chem. Soc., **129** (2007) 3612.

[148] K. Barthelet et al., Chem. Commun., (2004) 520.

[149] J. E. Mondloch et al., Chem. Commun., **50** (2014) 8944.

[150] Suvendu Sekhar Mondal et al., Chem. -A Eur. J., **22** (2016) 6905.

[151] J. I. Feldblyum et al., J. Am. Chem. Soc., **133** (2011) 18257.

[152] D. Giebel and J. Kansy, Physics Procedia, **35** (2012) 122.

[153] R. Zaleski et al., Radiat. Phys. Chem., **76** (2007) 243.

[154] R. E. Morris, Chem. Commun., (2009) 2990.

[155] F. Debatin et al., J. Mater. Chem., **22** (2012) 10221.

[156] Y. Zou et al., Chem. Commun., (2007) 5182, DOI: 10.1039/b712485f.

[157] Z. Fang et al., Angew. Chem. Int. Ed., **54** (2015) 7234.

[158] O. V. Gutov et al., Inorg. Chem., **54(17)** (2015) 8396.

[159] A. Bhunia et al., Chem. Commun., **52** (2016) 1401.

[160] J. Tian et al., CrystEngComm, **14** (2010) 1909.

[161] W. Xiao et al., J. Am. Chem. Soc., **136** (2014) 14200.

[162] V. Guillerm et al., Chem. Soc. Rev., **43** (2014) 6141.

[163] S. S. Mondal et al., ChemistrySelect, **1** (2016) 4320.

[164] R. S. Patil et al., Angew. Chem., **128** (2016) 4599.

[165] Z. Fang et al., Angew. Chem. Int. Ed., **54** (2015) 7234.

[166] A. W. Thornton et al., Dalton Trans., **45** (2016) 4352.

[167] I. Hisaki et al., Angew. Chem., **127** (2015) 3051.

[168] H. Wang et al., Chen, J. Am. Chem. Soc., **137** (2015) 9963.

[169] T. M. McDonald et al., Chem. Sci., **2** (2011) 2022.

[170] D. H. Hong and M. P. Suh, Chem. Commun., **48** (2012) 9168.

[171] S. Henke and R. A. Fischer, J. Am. Chem. Soc., **133** (2011) 2064.

[172] S. R. Caskey et al., J. Am. Chem. Soc., **130** (2008) 10870.

[173] Z. Fang et al., Angew. Chem.,Int. Ed., **54** (2015) 7234.

[174] K. Behrens et al., Inorg. Chem., **54** (2015) 10073.

[175] W. Xu et al., Microporous Mesoporous Mater., **180** (2013) 114.

[176] H. Wei et al., Chem. Commun., **51** (2015) 12178.

[177] S. S. Mondal et al., Chem. Commun., **49** (2013) 7599.

[178] D. M. Johnson and P. G. Rasmussen, Macromolecules, **33** (2000) 8597.

[179] S. S. Mondal et al., Dalton Trans., **46** (2017) 4824.

[180] S. Dey et al., J. Mater. Chem. A, **5** (2017) 3609.

[181] S. S. Mondal et al., Chem. Commun., **50** (2014) 5441.

[182] S. S. Mondal et al., CrystEngComm., **15** (2013) 9394.

[183] M. Thommes et al., Pure Appl. Chem., **87** (2015) 1051.

[184] S. V. Stepanov et al., Adv. Phys. Chem., DOI: 10.1155 (2012) 431962.

[185] A. Galarneau et al., Catalysis Today, **68** (2001) 191.

[186] L. F. Giraldo et al., Macromol. Symp. , **258** (2007) 129.

[187] Ying Wang et al., Nanomedicine: Nanotechnology, Biology, and Medicine, **11** (2015) 313.

[188] T. Martin et al., Angew. Chem. Int. Ed., **41(14)** (2002) 2590.

[189] Q. Cai et a et al., Chem. Mater., **13** (2001) 258.

[190] Q. Huo et al., Chem. Mater., **9** (1997) 14.

[191] H. Yang et al., J. Mater. Chem., **8** (1998) 743.

[192] P. J. Bruinsma et al., Chem. Mater., **9** (1997) 2507.

[193] W-D Einicke et al., Materials, **6** (2013) 3688.

[194] J. Hollenbach et al., J. Phys. Chem. C, **121** (2017) 15804.

[195] J. Babin et al., New J. Chem., **31** (2007) 1907.

[196] H. Uhlig et al., Microporous Mesoporous Mater., **182** (2013) 136.

[197] H. Alyosef et al., Chem. Eng. Trans., **37** (2014) 667.

[198] A. J. Schwanke et al., Cerâmica, **59** (2013) 181.

[199] H. Alyosef et al., Particulate Science and Technology: An International Journal, **31(5)** (2013) 524.

[200] R. Zaleski et al., Journal of Colloid and Interface Science, **343** (2010) 134.

[201] R. Ferragut et al., Journal of Physics: Conference Series, **262** (2011) 012020.

[202] R. Zaleski et al., NUKLEONIKA, **58(1)** (2013) 235.

[203] A. Galarneau et al., Adv. Funct. Mater., **16** (2006) 1657.

[204] Thomas R. Pauly et al., J. AM. CHEM. SOC., **124(1)** (2002) 97.

[205] M. Gorgol et al., ACTA PHYSICA POLONICA A, **132(5)** (2017) 1559.

[206] V. Meynen et al., Microporous and Mesoporous Mater., **125** (2009) 170.

[207] Y. J. He et al., J. Phys.: Condens. Matter, **13** (2001) 2467.

[208] R. Zaleski and M. Sokol, Materials Science Forum, **666** (2010) 123.

[209] M. Gorgol et al., Materials Science Forum, **733** (2013) 24.

[210] A. Grill et al., Appl. Phys. Rev., **1** (2014) 011306.

[211] A. Grill et al., ppl. Phys. Lett., **79(6)** (2001) 803.

[212] P. Marsik et al., Thin Solid Films, **518(15)** (2010) 4266.

[213] P. Garrou, Solid State Technology, **10** (2010).

[214] Hae-Jeong Lee et al., Journal of Polymer Science: Part B: Polymer Physics, **40** (2002) 2170.

[215] M. R. Baklanov et al., J. Vac. Sci. Technol. B, **18(3)** (2000) 1385.

[216] A. Wagner et al., IOP Conf. Series: Journal of Physics: Conf. Series, **791** (2017) 012004.

[217] A. F. Makhov, Sov. Phys. Sol. State, **2** (1961) 1934.

[218] C. L. Wang et al., Appl. Phys. Lett., **81(23)** (2002) 4413.

[219] P. Crivelli et al., Materials Science Forum., **607** (2008) 251.

Publications

1- *Positron annihilation lifetime spectroscopy at a superconducting electron accelerator*, A. Wagner, W. Anwand, **A. G. Attallah**, G. Dornberg, M. Elsayed, D. Enke, A. E. Hussein, R. Krause-Rehberg, M. O. Liedke, K. Potzger, and T. T. Trinh, IOP Conf. Series: Journal of Physics: Conf. Series, 79 (2017) 012004.

2- *Insights into the pores of the microwave-assisted metal imidazolate frameworks showing enhanced gas sorption*, Suvendu Sekhar Mondal, Subarna Dey, **Ahmed G. Attallah**, Reinhard Krause-Rehberg, Christoph Janiak, and Hans-Jürgen Holdt, Dalton Trans., 46 (2017) 4824.

3- *Missing Building Blocks Defects in a Porous Hydrogen-bonded Amide-Imidazolate Network Proven by Positron Annihilation Lifetime Spectroscopy*, Suvendu Sekhar Mondal, Subarna Dey, **Ahmed G. Attallah**, Asamanjoy Bhunia, Alexandra Kelling, Uwe Schilde, Reinhard Krause-Rehberg, Christoph Janiak, and Hans- Jürgen Holdt, ChemistrySelect, 1 (2016) 4320 .

4- *Study of the Discrepancies between Crystallographic Porosity and Guest Access into Cadmium–Imidazolate Frameworks and Tunable Luminescence Properties by Incorporation of Lanthanides*, Suvend Sekhar Mondal, Asamanjoy Bhunia, **Ahmed G. Attallah**, Philipp R. Matthes, Alexandra Kelling, Uwe Schilde, Klaus Mìller-Buschbaum, Reinhard Krause-Rehberg, Christoph Janiak, and Hans-Jìrgen Holdt, Chem. Eur. J., 22(2016) 6905.

Declaration

I hereby, declare that this thesis is an original report of my research, has been written by myself without any external help. The experimental work is almost entirely my own work; the collaborative contributions, such as sample preparation, have been indicated clearly and acknowledged. References have been provided correctly on all supporting literatures and resources.

I declare that this work has not been submitted for any other degree or professional qualification either in Martin-Luther-University, Halle-Wittenberg or in any other University.

_____   _____

Place and date   Elsherif, Ahmed Gamal Attallh Abdelmaksoud

Curriculum vitae

Family name: Elsherif

Given name: Ahmed Gamal Attallah Abdelmaksoud

Date of birth: 20.08.1986

Place of birth: Kalyobiya, Egypt

Marital status: Married

1992-1997: Primary school

1997-2001: Prep school

2001-2004: High school

2004-2008: Bachelor of Physics, Minia University, Egypt

2010-2013: Master in Physics, Minia University, Egypt

April 2015-Present: PhD student, Positron Annihilation Laboratory, Martin-Luther-University-Halle-Wittenberg

_____

Place and date

_____

Elsherif, Ahmed Gamal Attallh Abdelmaksoud

_____

This dissertation was typeset with LaTeX[1] by the author.

_____

[1] LaTeX is a document preparation system developed by Leslie Lamport as a special version of Donald Knuth's TEX Program.